

2017-01-01

Bimetallic Centers With Open Coordination Sites And Magnetic Nanocomposites For Water Remediation

Karen Ventura

University of Texas at El Paso, karen.ventura28@gmail.com

Follow this and additional works at: https://digitalcommons.utep.edu/open_etd



Part of the [Chemistry Commons](#)

Recommended Citation

Ventura, Karen, "Bimetallic Centers With Open Coordination Sites And Magnetic Nanocomposites For Water Remediation" (2017).
Open Access Theses & Dissertations. 575.
https://digitalcommons.utep.edu/open_etd/575

This is brought to you for free and open access by DigitalCommons@UTEP. It has been accepted for inclusion in Open Access Theses & Dissertations by an authorized administrator of DigitalCommons@UTEP. For more information, please contact lweber@utep.edu.

BIMETALLIC CENTERS WITH OPEN COORDINATION
SITES AND MAGNETIC NANOCOMPOSITES
FOR WATER REMEDIATION

KAREN VENTURA

Doctoral Program in Chemistry

APPROVED:

Dino Villagrán, Ph.D., Chair

Skye Fortier, Ph.D.

Shane Walker, Ph.D.

Keith Pannell, Ph.D

Charles Ambler, Ph.D.
Dean of the Graduate School

Copyright ©

by

Karen Ventura

2017

Dedication

To my grandma, because God sent me an angel.

BIMETALLIC CENTERS WITH OPEN COORDINATION
SITES AND MAGNETIC NANOCOMPOSITES
FOR WATER REMEDIATION

by

KAREN VENTURA, M.S.

DISSERTATION

Presented to the Faculty of the Graduate School of
The University of Texas at El Paso
in Partial Fulfillment
of the Requirements
for the Degree of

DOCTOR OF PHILOSOPHY

Department of Chemistry
THE UNIVERSITY OF TEXAS AT EL PASO
December 2017

Acknowledgements

First and foremost, I would like to thank my research advisor, Dr. Villagrán, for all of his support and guidance in my research and for his knowledge, enthusiasm, and immense patience.

In addition to my advisor, I would like to thank the members of my committee, Dr. Pannell, Dr. Fortier and Dr. Walker for their constructive commentary and their reliable advice. Additionally, I would like to thank Dr. Goos for his assistance in X-ray crystallography

I thank my fellow lab mates of the Villagrán lab, José, Yanyu, Nancy, and Yulu for all of the chemistry discussions, sleepless nights before deadlines, for the drama, and for all the fun that we had together throughout these four years. I would also like to show gratitude to my undergraduate assistants Roy, Edgar, and Jonathan for all of their hard work and for all the laughs we shared together, they made a lot of this research possible. Also to Jacob and Luis for their help even when they are miles away. Also, a special thanks to Andrew for every time I needed help in organic chemistry.

Special thanks to my parents and siblings for everything because everyone needs a team to rely on, to trust, and to open up to. To Jacobo for being my support in all of the good times and the not-so-good times, for his patience and for all the laugh we have shared.

Finally I would like to thank all the faculty and staff from the UTEP chemistry department, especially Dr. Narayan and Dr. Dirk for their valuable advice and support in my graduate studies.

Abstract

The development of effective, renewable and environmentally friendly energy sources is essential to supply the growing global energy demands. The use of fossil fuels to fulfill those energy demands have led to the increase of greenhouse gases and water contamination. The extraction of oil and gas requires a large amount of pressurized water, resulting in contaminated water as a byproduct. Meanwhile, ensuring access to clean water is one of the greatest global challenges of this century.

The following study is presented in three sections. In the first section, a bimetallic system with open coordination sites that can be used as a platform for the activation of small molecules has been synthesized. Small molecule activation is important to synthesize more energy dense compounds that can later serve as chemical fuels. A quadruply bonded complex $W_2(DippF)_2K_2$ with a $W_2(0)$ core was synthesized and structurally characterized. The observed W-W distance of 2.407(1) Å, which is longer than previously reported quadruply bonded complexes. DFT calculations were used to elucidate the electronic structure of the unprecedented complex having a D_{2h} symmetry, resulting in a molecular orbital configuration of $\sigma^2\pi^2\pi^2\delta^2\delta^{*2}$ where the HOMO is the δ^* .

To prepare future generations for the development of new energy sources, we have designed a four-hour physical chemistry laboratory to introduce upper division students to electrochemistry concepts, including mixed-valency and electron-transfer (ET), using cyclic and differential pulse voltammetries. In this laboratory practice, students use a ferrocene dimer consisting of two ferrocene centers covalently bonded through a dimethylethylene bridge as a platform for the measurement of inner-sphere ET. The degree of electronic communication between the ferrocene redox centers is measured by the magnitude of the equilibrium constant of the comproportionation reaction that yields the mixed valent ferrocene dimer. Students measure the difference in $E_{1/2}$ from the electrochemistry of the ferrocene dimers and categorize these ferrocene dimers according to the Robin-Day classification.

The use of fossil fuels have left a negative environmental impact in sources of fresh water. Water contamination is the result of the use of fracking techniques to extract oil and gas. In an attempt to approach this issue a series of highly efficient water contaminant adsorbents were developed using $\text{Ni}_3(\text{BTC})_2$ and $\text{Co}_3(\text{BTC})_2$ metal-organic frameworks (MOFs) and Fe_3O_4 magnetic nanoparticles (MNPs) to functionalize graphene oxide (GO). XRD results show high crystallinity of the prepared nanomaterials and the successful decoration of $\text{Ni}_3(\text{BTC})_2$ and $\text{Co}_3(\text{BTC})_2$ MOFs over the GO substrate (BTC = benzene-1,3,5-tricarboxylic acid). SEM and TEM imaging show the successful formation of nanoscale MOFs and Fe_3O_4 MNPs over GO. IR spectroscopy supports the characterization and successful preparation of the $\text{Fe}_3\text{O}_4/\text{MOF}@GO$ hybrid nanocomposites. The prepared adsorbents were used to sorb methylene blue (MB) as a model for common organic pollutants in water and common ions from a brackish water model (Na^+ , Ca^{2+} , Mg^{2+} , SO_4^{-2} , SiO_3^{-2}). The adsorption capacity for methylene blue of the prepared nanocomposites is improved by an average of 30.52 and 13.75 mg/g for the Co and Ni composite, respectively, when compared to the MOFs parent materials. The adsorption capacity for sulfates improves by 92.1 mg/g for the Co composite and 112.1 mg/g for the Ni composite, when compared to graphene oxide. This adsorption capacity enhancement is attributed to suppressed aggregation through increased dispersive forces in the MOFs due to the presence of GO, formation of nanoscale MOFs over the GO platform, and the hindering of stacking of the graphene layers by the MOFs. Leaching tests show that the release of Co and Ni ions to water is reduced from 105.2 and 220 ppm, respectively, in the parent MOF materials to 0.5 and 16.4 ppm, respectively, in the nanocomposites. These findings show that the newly developed adsorbents can sorb organic pollutants, and target sulfate and silicate anions, which makes them suitable candidates for water and wastewater treatments

Table of Contents

Acknowledgements	v
Abstract	vi
Chapter I: Introduction	1
Chapter II: Unprecedented $W_2(0)$ quadruply bonded complex supported by π -donor ligands	6
2.1. Introduction	6
2.2. Experimental	7
2.2.1. Materials and Methods	7
2.2.2. General Procedures	7
2.2.3. Physical Measurements	8
2.2.4. Preparation of $W_2(DippF)_2Cl_4$ (1)	9
2.2.5. Preparation of $W_2(DippF)_2Cl_4Li$ (2)	9
2.2.6. Preparation of $W_2(DippF)_2K_2$ (3)	9
2.3. Computational Details	10
2.4. Crystallography	12
2.4.1. X-ray Crystal Structure of 2, $W_2(DippF)_2Cl_4Li \cdot 4THF$	12
2.4.2. X-ray Crystal Structure of 3, $W_2(DippF)_2K_2$	15
2.5. Results and Discussion	18
2.6. Conclusion	22
Chapter III: Introducing students to inner sphere electron transfer concepts through electrochemistry studies in diferrocene mixed-valence systems	23
3.1. Introduction	23
3.2. Laboratory description	25
3.3. Materials and methods	29
3.3.1. General	29
3.3.2. Physical Measurements	29
3.3.3. Synthesis of E and Z-dimethylferrocene dimers	29
3.4. Hazards	30
3.5. Results and Discussion	31
3.5.1. Electrochemistry	31
3.6. Conclusion	31
Chapter IV: Superparamagnetic MOF@GO Ni and Co based hybrid nanocomposites as efficient water pollutant adsorbents	33
4.1. Introduction	33

4.2. Experimental	36
4.2.1. Materials and Methods	36
4.2.2. Physical Measurements	37
4.2.3. Synthesis of Graphene Oxide, 1	38
4.2.4. Synthesis of Fe ₃ O ₄ nanoparticles, 2	38
4.2.7. Synthesis of Co ₃ (BTC) ₂ • 12 H ₂ O MOF, 5	40
4.2.8. Synthesis of Ni ₃ (BTC) ₂ •12 H ₂ O MOF, 6.....	40
4.2.9. Synthesis of Composite Fe ₃ O ₄ /GO/Co ₃ (BTC) ₂ • 12 H ₂ O, 7	41
4.2.10. Synthesis of Composite Fe ₃ O ₄ /GO/Ni ₃ (BTC) ₂ • 12 H ₂ O, 8	41
4.3. Results and Discussions	42
4.3.1. Methylene Blue Adsorption	49
4.3.2. Brackish water treatment.....	54
4.4.Conclusions	57
Chapter V: Conclusion	58
References	61
Appendix	67
Student Handout.....	69
Vita.....	78

List of Figures

Figure 1. Consumption timeline for different types of energy resources.	1
Figure 2. Molecular orbital for a bimetallic complex with a D_{2h} symmetry.....	2
Figure 3. Three layered nano-engineered composite for water remediation.	4
Figure 4. ORTEP diagram of 3 plotted at the 50% probability value. W(1)-W(1) distance 2.407(1) Å, W1-N(1) distance 2.08(2) Å.....	6
Figure 5. Molecular orbital diagram plotted at the 0.04 isodensity value for a dianionic model of 3 . 10	
Figure 6. Select molecular orbital plots for orbitals showing strong π interactions.....	11
Figure 7. ORTEP diagram of 2 plotted at the 50% probability value. W(1)-W(1) distance 2.280(1) Å, W1-N(1) distance 2.130(1) Å.....	15
Figure 8. EPR spectrum of compound 2 showing an isotropic signal with a g value of 1.86.....	18
Figure 9. Raman spectra for 3 . The $\nu(W-W)$ can be observed at 299.4 cm^{-1} . Strong ligand vibrations were observed at 343.7 and 421.8 cm^{-1}	18
Figure 10. UV-vis spectrum of compound 3	20
Figure 11. Cyclic voltammogram of 1 depicting two reversible redox events and one non-reversible oxidation.....	20
Figure 12. Molecular orbital depicting ligand-metal interactions of compound 3	21
Figure 13. The famous Creutz-Taube ion studied as a platform for the study of inner-sphere electron transfer. Henry Taube was awarded the Nobel Prize in 1983.	24
Figure 14. Diferrocene complexes used in this laboratory practice.....	26
Figure 15. Experimental setup for the electrochemical measurements. The cap is designed to hold the working electrode (Green), the reference electrode (white), the counter electrode (red) and a purging needle	27
Figure 16. Cyclic voltammogram and differential pulse voltammogram of 2	28
Figure 17. Cyclic voltammogram and differential pulse voltammogram of 3	31
Figure 18. XRD spectrum of the Co nanocomposite, 7 (top) compared to the spectra of the parent materials ($\text{Fe}_3\text{O}_4@\text{GO}$, 4 ; $\text{Co}_3(\text{BTC})_2$, 5 ; GO , 1).	42
Figure 19. XRD spectrum of the Ni nanocomposite, 8 (top) compared to the spectra of the parent materials ($\text{Fe}_3\text{O}_4@\text{GO}$, 4 ; $\text{Ni}_3(\text{BTC})_2$, 6 ; GO , 1).	43
Figure 20. TEM images for GO-nanocomposites. (a) Go coated with Fe_3O_4 nanoparticles. (b) $\text{GO-Co}_3(\text{BTC})_2$ magnetic nanocomposite. (c) $\text{GO-Ni}_3(\text{BTC})_2$ magnetic nanocomposite.	43
Figure 21. SEM images for parent materials. (a) $\text{Ni}_3(\text{BTC})_2$. (b) $\text{Co}_3(\text{BTC})_2$. (c) Fe_3O_4 Nanoparticles. (d) Fe_3O_4 nanoparticles functionalized with APTES.....	44
Figure 22. XPS spectra for a) Co Composite $\text{Fe}2p_{3/2}$ with peaks at 711 and 725 eV. b) Co $2p_{3/2}$. c) Ni Composite $\text{Fe}2p_{3/2}$ with peaks at 711 and 725 eV and d) Ni $2p_{3/2}$ at 853, 861 and 873 eV.	45
Figure 23. XPS complete spectra as well as carbon and oxygen spectra of the prepared $\text{Fe}_3\text{O}_4/\text{GO}/\text{Ni}_3(\text{BTC})_2$	46
Figure 24. XPS complete spectra as well as carbon and oxygen spectra of the prepared $\text{Fe}_3\text{O}_4/\text{GO}/\text{Co}_3(\text{BTC})_2$	47
Figure 25. Infrared spectra comparison of parent materials and graphene oxide nanocomposites.....	48
Figure 26. M vs. H curves at 300 K for: Fe_3O_4 NPs 2 , Fe_3O_4 NPs coated w/ 3-aminopropyl triethoxysilane 3 , Fe_3O_4 NPs coated w/ 3-aminopropyl triethoxysilane on GO nanosheets 4 , Ni(II) MOFs and Fe_3O_4 NPs coated w/ 3-aminopropyl triethoxysilane on GO nanosheets, 8 ,	48
Figure 27. UV-Vis spectra of the adsorbed methylene blue dye at different concentrations using the parent materials	50

Figure 28. UV-Vis spectra of the adsorbed methylene blue dye at different concentrations using the prepared nanocomposites	51
Figure 29. Langmuir isotherms (Type II) of methylene blue onto Co and Ni magnetic nanocomposites	52
Figure 30. Langmuir isotherms (Type I) of methylene blue onto Co and Ni magnetic nanocomposites	52
Figure 31. Absorption capacity of parent materials and composites of methylene blue at 12.5, 25, 50 and 100 ppm.....	54
Figure 32. NMR spectrum of $W_2(DippF)_2Cl_4$ in d-THF.....	67
Figure 33. NMR spectrum of $W_2(DippF)_2K_2$	68
Figure 34. Hysteresis loop studies for a) Fe_3O_4 , b) $GO-Fe_3O_4$, c) Fe_3O_4 -APTES, d) Co composite, e) Ni composite	77

List of Tables

Table 1. Sample and crystal data for 2 , (W ₂ (DippF) ₂ Cl ₄ Li).	13
Table 2. Data collection and structure refinement for 2 , (W ₂ (DippF) ₂ Cl ₄ Li)	14
Table 3. Sample and crystal data for 3 , (W ₂ (DippF) ₂ K ₂).	16
Table 4. Data collection and structure refinement for 3 , (W ₂ (DippF) ₂ K ₂).	17
Table 5. Calculated and experimental data for compound 3	17
Table 6. Comparison of the Assessment Results for the Pre-lab Quiz and Lab Report.....	26
Table 7. Summary of magnetic studies for the Ni and Co composites	49
Table 8. Absorption capacity of parent materials and composites at different concentrations of methylene blue	50
Table 9. Langmuir maximum absorption capacities for the Co and Ni hybrid nanocomposites.	53
Table 10. Initial Concentration of Analytes in Test Water	55
Table 11. Adsorption capacity for tested nanomaterials and composites per analyte.	55
Table 12. Average ion concentration due to dissolution of nanomaterials in test solutions.	56
Table 13. Adsorption capacity and percent removal of ions for tested nanomaterials and composites per analyte.	56
Table 14. Adsorption capacity and percent removal of methylene blue for tested nanomaterials and composites per analyte	56

Chapter I: Introduction

The global energy demand is increasing daily due to rapid growth in population, urbanization, industrialization, among other reasons.¹ In 2012 the world energy consumption was of 160,000 TWh, which is the equivalent of having 25 billion horses constantly working for us.² Currently, fossil fuels provide 85% of our energy needs. The use of fossil fuels is accountable for the emission of greenhouse gases such as CO₂. Since the industrial revolution, the concentration

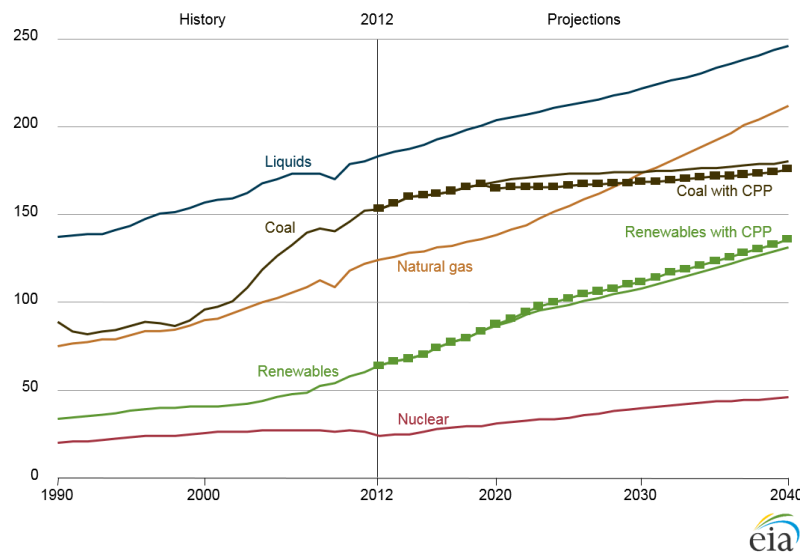


Figure 1. Consumption timeline for different types of energy resources.

of CO₂ in the atmosphere has risen from 278 ppm to more than 400 ppm today. Remarkably, 75% of this rise has been observed since the 1950s.^{1,2} In addition, the increasing demand of fossil fuels has led to the development of hydraulic (fracking) techniques. This process requires pressurized water and sand to be injected into wells to fracture shale rock and extract oil and gas. This process results in the contamination of large water bodies.³ In order to avoid the environmental impact that the use of fossil fuels entitle, it is necessary to move to cleaner sources of energy, such as solar energy. One of the biggest challenges solar power is facing these days is that once solar energy has been harvested it is difficult to store it.¹ Nature has been able to store solar energy for millennia, where plants use water, carbon dioxide and sunlight to

produce sugar where energy is stored in the form of chemical bonds.⁴ This process requires the transfer of multiple electrons. Therefore, the study of multi-electron redox chemistry is a promising pathway for making this and other processes (such as the production of ammonia and the generation of chlorine gas) more efficient. Important multi-electron redox reactions such as the Fischer-Tropsch process,⁵ the reduction of carbon dioxide,⁶ hydrogen generation,⁷ and hydrocarbon cracking,⁸ require a heterogeneous catalyst. Up to date, it is challenging to obtain mechanistic information of processes that require a heterogeneous catalyst, yet, the understanding of the fundamentals is central to the advancements of these processes. Hence, molecular systems that perform similar reactions can be used as platforms to understand the basic activation chemistry of small molecules with energy implications.

The role of the catalyst can be studied by moving the focus from the reactivity on the bulk materials to the molecular level. In order to this, on the first study of this dissertation we

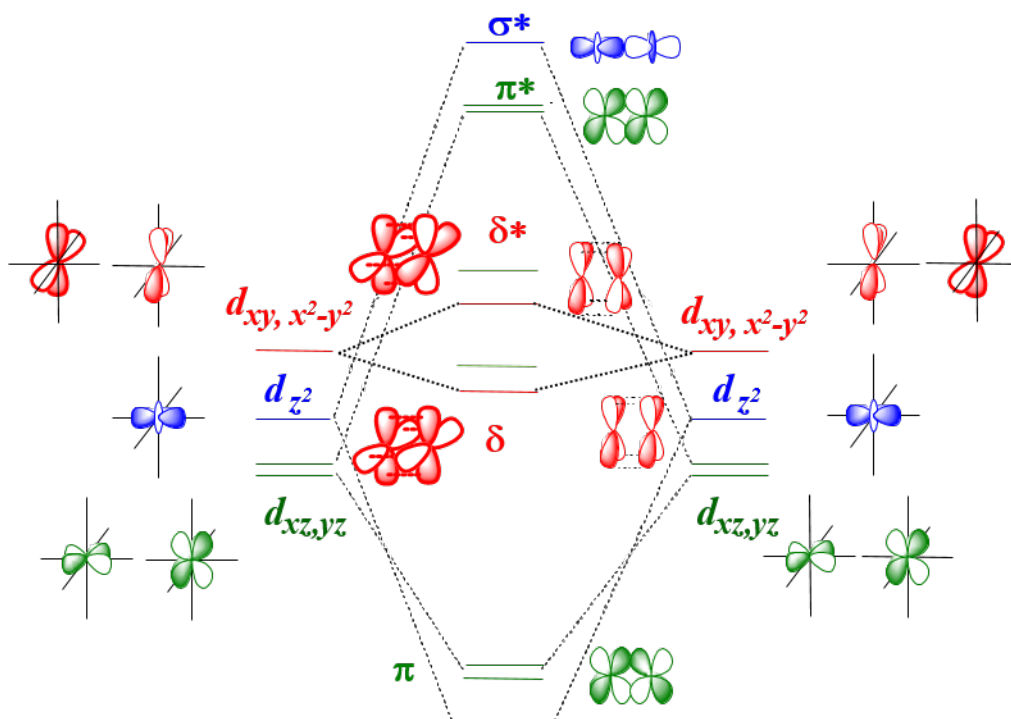


Figure 2. Molecular orbital for a bimetallic complex with a D_{2h} symmetry

have decided to use bimetallic centers with open coordination sites in the D_{2h} conformation. The molecular arrangement of bimetallics with D_{2h} symmetry is characterized by one σ orbital arising from the interaction of two d_z^2 orbitals, two π orbitals coming from the lateral interaction of two d_{xz} and two d_{yz} orbitals and two δ orbitals originating from the face to face interaction of a d_{xy} and $d_{x^2-y^2}$ orbitals with their corresponding antibonding orbitals.⁹ The electronic configuration of group six bimetallics is suitable for the formation of complexes with a D_{2h} conformation, thus the chemistry of dichromium and dimolybdenum complexes is very rich.^{10,11} On the other hand, the chemistry of ditungsten complexes is modest, in part, because of its more difficult synthetic pathways and increased reactivity. Formamidinates have been successful ligands used to synthesize bimetallic complexes.¹²⁻¹⁴ They have been the focus of interest due to their high basicity, which allows them to stabilize bimetallic units with high oxidation states.^{15,16} Herein, we present a quadruply bonded ditungsten $[W_2(0)]$ complex supported by two bis-diisopropylphenyl formamidinate bridging ligands.

In order to continue the exploration of new and clean sources of energy, it is important to teach future generations about multi-electron redox and other related energy production processes. The study of inner-sphere electronic communication is useful to understand how multi-electron redox process are carried out when two systems are covalently bonded to a linker. In these types of systems, the electron passes through a linker in order to be transferred from one metallic center to another. In some cases, the process has an intermediate species which consists of a mixed-valent complex, that is, two atoms of the same element coexist in different oxidation states.¹⁷ For this dissertation, we used a previously reported differrocene complex to illustrate the concept of inner-sphere electron transfer.¹⁸ This experiment is focused on students coursing junior year of college. This work was done when a deficit in educational literature addressing

this concept was observed. In order to fully explain the concept of inner-sphere electron transfer, a laboratory practice was developed for physical chemistry and inorganic chemistry courses. This laboratory practice was implemented in a physical chemistry course at The University of Texas at El Paso during the 2014-2015, 2015-2016, 2016-2017 and currently the 2017-2018 academic years.

Finally, water contamination resulting from oil and gas extracting processes is an important environmental and social issue. The worldwide problems connected with the lack of fresh water are vast. Today, 12 billion people lack access to safe drinking water, 2.6 billion people have little or no sanitation, meanwhile 3,900 children a day die from diseases transmitted through unsafe water.¹⁹⁻²¹ The removal of contaminants such as heavy metals and toxic organic chemicals from water sources is critical. A decade ago nanotechnology made a revolutionary change on traditional atomic chemistry. By thinking in a scale bigger than a molecule, interesting properties became a promising solution to various issues such as the energy crisis, cybersecurity, chemotherapy and environmental remediation.²² Properties such as increased surface area, selective absorptivity, catalytic activity, magnetism, among others have opened the window to a new interest in engineered nanomaterials with increased intricacy and functionality comparable (*or even better*) to those existing technologies currently being used. Nanotechnology is being currently studied as a medium for environmental remediation.²³ The exponential growth of the population, the fracking

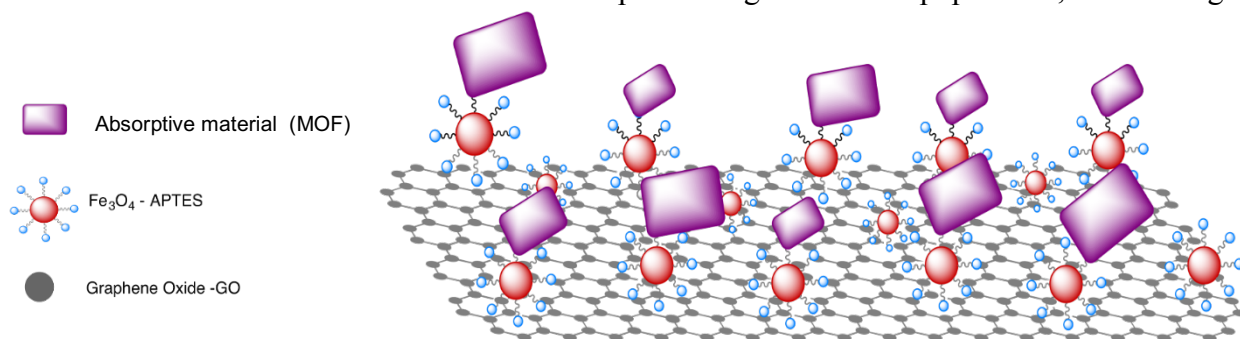


Figure 3. Three layered nano-engineered composite for water remediation.

industries, increased energy need, among other practices have increased the need for new, efficient and affordable technologies for water purification.

Our objective was to develop a nanoengineered material with the following properties: (1) high adsorptivity towards different types of water pollutants, (2) high stability towards different types of stresses conditions in the environment, and (3) intrinsic magnetic character for its easy removal from different kind of medium. In this dissertation, we present a novel three-layered nanocomposite consisting of graphene oxide acting as a supporting platform,²⁴ metal-organic frameworks as an adsorptive entity^{25,26} and finally iron oxide (magnetite) nanoparticles acting as the magnetic component.²⁷ We studied the synergistic effect of the afore mentioned components idealized in a novel nanocomposite, where graphene oxide is functionalized with $M_3(BTC)_2$ MOFs ($M = \text{Co}$ and Ni) and iron oxide nanoparticles (Fe_3O_4). The syntheses and characterization of these composites is shown as well as an analytical study of their efficiency in removing methylene blue, and their performance in targeting specific ions found in brackish water

Chapter II: Unprecedented $W_2(0)$ quadruply bonded complex supported by π -donor ligands*

2.1.Introduction

The chemistry of W_2 complexes has recently been the subject of renewed interest by many research groups due to its potential in small molecule activation reactions.^{28–34} However, in contrast to the rich chemistry of the other two group 6 bimetallics (Cr_2 and Mo_2), the chemistry of W_2 complexes has been characterized by their propensity to be easily oxidized. In fact, W_2 compounds are so easily oxidized that tetragonal compounds bridged by guanidinate ligands are the most easily ionizable complexes measured to date, and have potential uses as strong reductants.²⁸ Bimetallic complexes bridged by π -acceptor ligands such as CO allow the

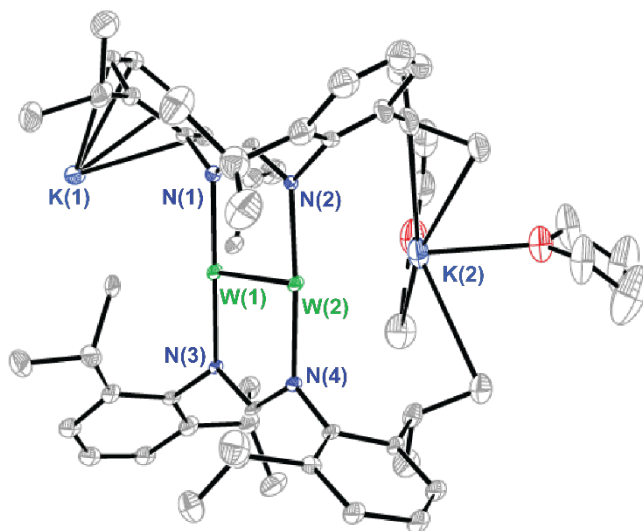


Figure 4. ORTEP diagram of **3** plotted at the 50% probability value. W(1)-W(1) distance 2.407(1) Å, W1-N(1) distance 2.08(2) Å.

** This chapter has previously appeared as an article in Chemical Communications. The original citation is as follows: K. Ventura, J. R. Prat, L. M. Aguirre Quintana, A. Goos and D. Villagrán; Unprecedented $W_2(0)$ quadruply bonded complex supported by π -donor ligands *ChemComm*, **2016**, 52, pp.3974-3976

formation of singly-bonded staggered complexes such as $\text{Mn}_2(\text{CO})_{10}$, $\text{Re}_2(\text{CO})_{10}$, $\text{MnRe}(\text{CO})_{10}$ and $\text{Co}_2(\text{CO})_8$,^{35–37 *}

whose chemistry has been well-studied. These bimetallic complexes supported by π -acceptor ligands can be considered as being formed by two $\text{M}(\text{CO})_5$ fragments that are isolobal with the methyl radical and behave accordingly,^{35–37} yet no W_2 complexes of this type are known to exist. While π -acceptor ligands can help stabilize electron rich metals thanks to back-bonding, ligands of increased basicity, such as π -donors, are needed to support bimetallic complexes with higher oxidation states. The most common ligands of this type are carboxylates, formamidinates, and guanidinates.^{32,38}

The lowest oxidation state of W–W bonded complexes when bridged by π -donor ligands is W(II)–W(II). In contrast, dichromium and dimolybdenum bimetallic systems have been isolated with oxidation states of Cr(I)–Cr(I) and Mo(I)–Mo(I). Currently, no ditungsten analogs are known, in part, due to the difficulty of their synthesis. While the W(I)–W(I) complex is still unreported (but still pursued by us and others), herein we report the synthesis and characterization of an even more highly reduced W(0)-W(0) bimetallic complex (Figure 4) supported by two DippF ligands (DippF = bis-diisopropylphenyl formamidinate) and its precursors.

2.2.Experimental

2.2.1. Materials and Methods

2.2.2. General Procedures

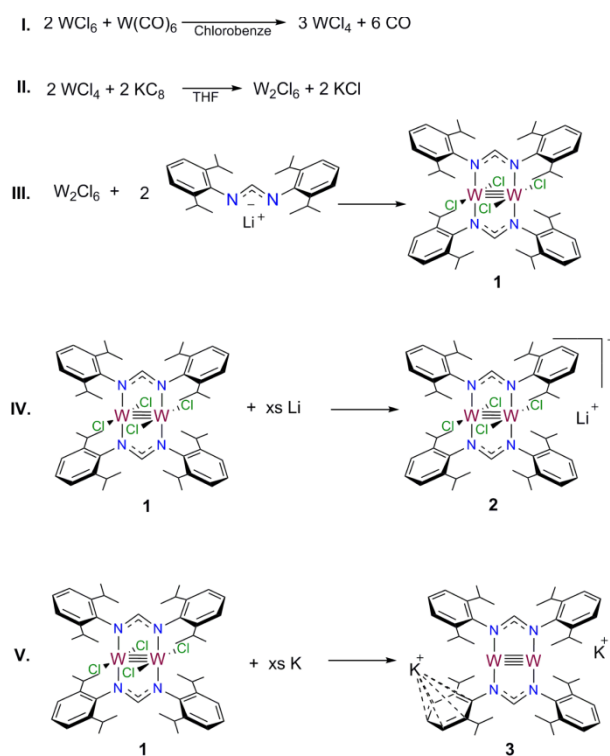
Standard vacuum line, dry-box, and Schlenk techniques under nitrogen atmosphere were used for the synthesis of all compounds. All solvents were dried and degassed using a Pure Process

Technology solvent purification system prior to use. Tungsten tetrachloride and HDippF were synthesized according to previously reported literature procedures.^{39,40}

2.2.3. Physical Measurements

¹H NMR spectrum was recorded in a J. Young NMR tube on a Bruker 400 MHz NMR spectrometer. The proton chemical shifts (δ) of **1** and **3** were referenced to the residual THF (δ = 1.72, 3.58) in d-THF solvent. Raman Spectrum was recorded on a Thermo ScientificTM DXR SmartRaman spectrometer using a 780 cm⁻¹ filter. Electrochemical analysis was performed in THF using a CHI760D potentiostat with a 2 mm diameter Pt working electrode, Pt mesh auxiliary electrodes and Ag/Ag⁺ (AgCl) reference electrode. All potentials were subsequently internally referenced to the ferrocene/ferrocenium couple by adding ferrocene to the sample at

Scheme 1. Synthetic pathway for W₂(DippF)₂K₂



the end of each run. The X-band (~ 9.5 GHz) EPR spectrum was obtained using a BrukerEMXplus spectrometer with an ER073 magnet at room temperature.

2.2.4. Preparation of $W_2(\text{DippF})_2\text{Cl}_4$ (1).

WCl_4 (0.500 g, 1.50 mmol) was reacted with KC_8 (0.417 g, 3.00 mmol) in 30 mL of THF at -94°C (liquid N_2 and acetone bath) under N_2 atmosphere until deep green coloration was observed. In a separate flask, $LiDippF$ was prepared by reacting $HDippF$ (0.557g, 1.50 mmol) and methyllithium (1.05mL, 1.68mmol) in 10 mL of THF at 0°C . The lithium formamidinate salt formed upon warming the solution to room temperature. It was then slowly added with a double tipped needle (cannula), for a period of 2 min, to the reduced ditungsten solution. The color turned dark blue after c.a. 1.5 h then the solution was filtered through a medium coarse filter packed with Celite®. The solvent was removed under reduced pressure, and the obtained red solid was washed thoroughly with diethyl ether and hexanes, and dried under vacuum. Isolated yield 0.830g, 25.85%. ^1H NMR spectroscopy (*d*-THF): δ 7.42 (s, 2H N-CH-N), 6.92-6.72 (m, 12H, *i*-Pr₂-C₆H₃), 3.62(septet, 8H, CHMe₂), 1.12 (d, 48H, (CH(CH₃)₂). CV (V vs. Fc/Fc⁺): E'_{ap} : -1.271, E'_{cp} : -1.287, $E'_{1/2}$: -1.279, E''_{cp} : -1.898, E''_{ap} : -2.206, E''_{cp} : -2.720, $E''_{1/2}$: -2.46.

2.2.5. Preparation of $W_2(\text{DippF})_2\text{Cl}_4\text{Li}$ (2).

0.475g of compound **1** was reacted with 0.475g of Li metal in a Schlenk flask in THF. The solution was heated to reflux and left to react for ~ 1 hr. and filtered with a medium coarse filter. The solvent was removed under reduced pressure and extracted with hexanes. Yellow crystals were grown from a concentrated solution of THF. Isolated yield 0.471 g, 98.6%. EPR: $g = 1.86$.

2.2.6. Preparation of $W_2(\text{DippF})_2K_2$ (3).

Compound **1** (0.200 g) was dissolved in 30 ml of THF. Potassium metal (1.00 g) was added to the resulting solution. The mixture was heated to reflux for two hours and then filtered through a medium coarse filter. The solvent was removed under reduced pressure and the product was

extracted with diethyl ether. Amber- red crystals were grown from a concentrated solution of diethyl ether at -10°C . Isolated yield 0.027g, 13.58%. ^1H NMR spectroscopy (*d*-THF): δ 7.48 (s, 2H N-CH-N), 6.87-6.61 (m, 12H, i-Pr₂-C₆H₃), 3.62(septet, 8H, CHMe₂), 1.10 (d, 48H, (CH(CH₃)₂)). ESI-MS $[\text{M}-\text{CH}_3]^+$: Calcd. 1157.4 found 1157.3 m/z.

2.3.Computational Details

Density Functional Theory (DFT)^{41,42} calculations were performed with the hybrid Becke-3 parameter exchange functional^{43,44} and the Lee-Yang-Parr nonlocal correlation functional⁴⁵ (B3LYP) implemented in the Gaussian 09⁴⁶ (Revision C.01) program suit. Double- ζ -quality basis sets (D95) were used on nonmetal atoms (carbon, nitrogen and hydrogen). An effective core potential (ECP) representing the 1s2s2p3s3p3d core was used for the tungsten atoms along

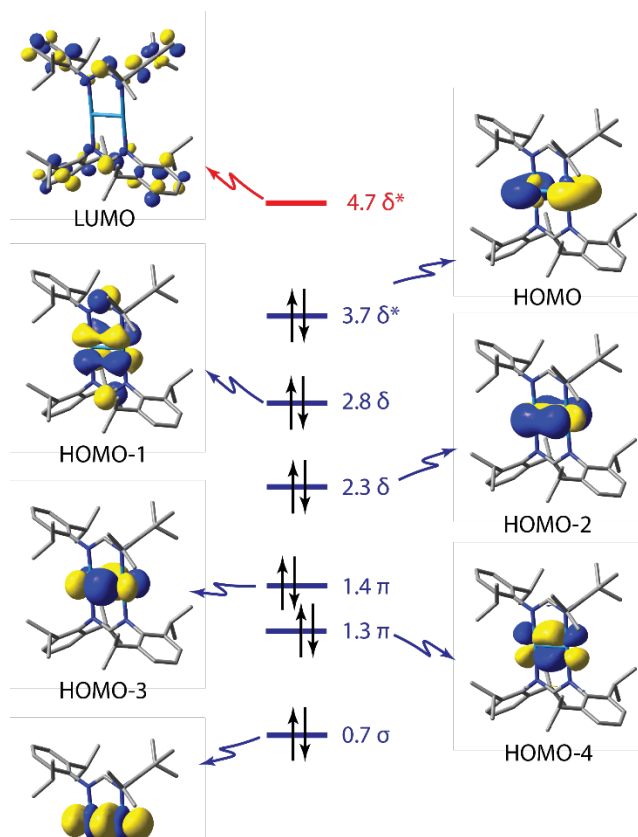


Figure 5. Molecular orbital diagram plotted at the 0.04 isodensity value for a dianionic model of **3**.

with the associated double- ζ basis set (LANL2DZ). The convergence criterion for the self-consistent field cycles on all calculations was increased from the default value to 10^{-8} . All the calculations were performed on a dianionic full-atom model of **3** with no simplifications. Geometry optimization calculations were found to be minima in the potential energy surface as

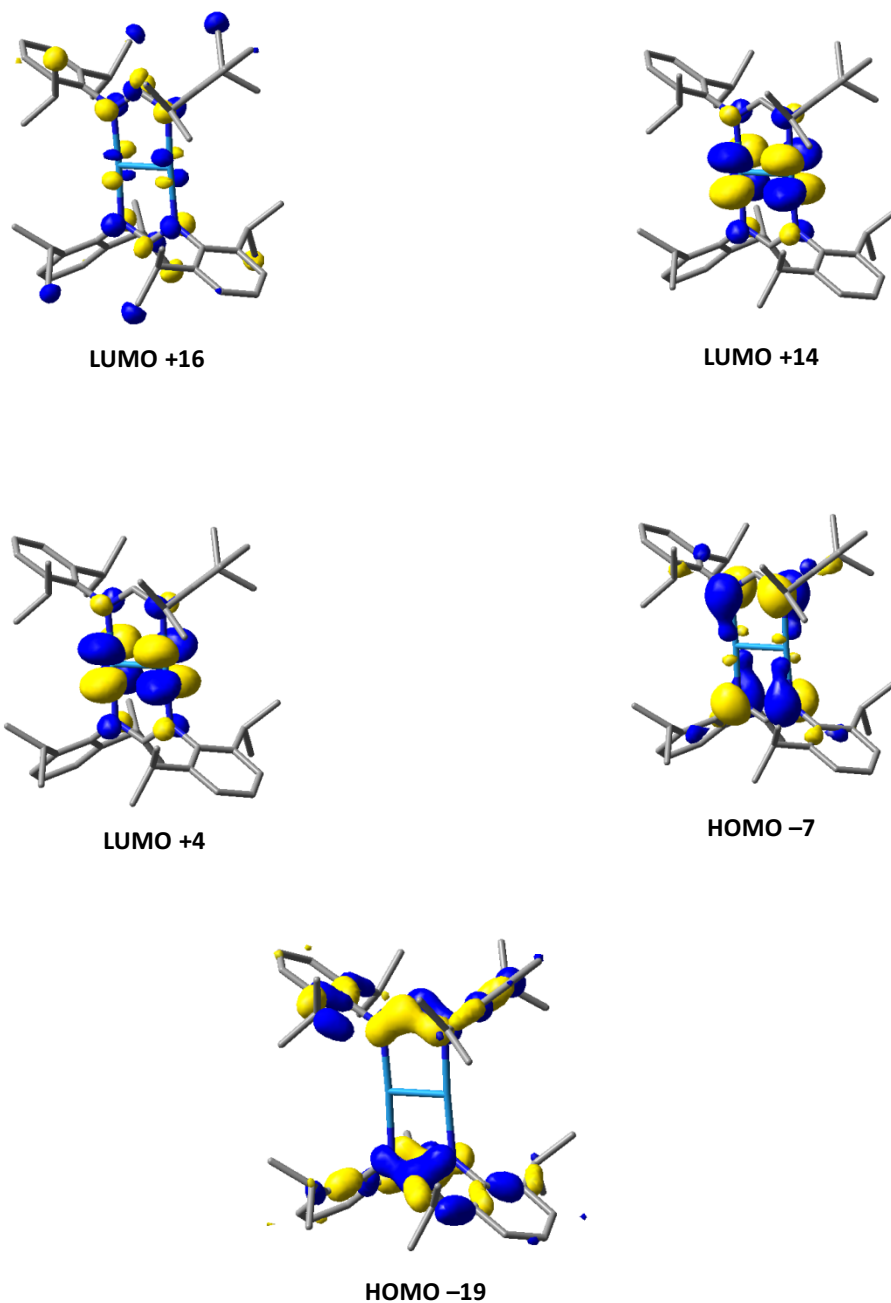


Figure 6. Select molecular orbital plots for orbitals showing strong π interactions

evidenced by the lack of imaginary vibrations in the frequency calculations. Raman calculations were performed by using the keyword freq=raman in Gaussian. All calculations were performed in a 44-processor PowerWolf PSSC supercomputer cluster running Linux Red Hat 4.1.2-54 located at the University of Texas at El Paso.

2.4. Crystallography

2.4.1. X-ray Crystal Structure of 2, W₂(DippF)₂Cl₄Li•4THF

A yellow block specimen of C₅₀H₇₀Cl₄N₄W₂•C₁₆H₃₂LiO₄, approximate dimensions 0.100 mm x 0.100 mm x 0.050 mm, was used for the x-ray crystallographic analysis. The x-ray intensity data were measured.

The frames were integrated with the Bruker SAINT software package using a narrow-frame algorithm. The integration of the data using a monoclinic unit cell yielded a total of 71366 reflections to a maximum θ angle of 24.18° (1.00 Å resolution), of which 5451 were independent (completeness = 99.4%, R_{int} = 11.40%, R_{sig} = 10.15%) and 4689 (86.02%) were greater than $2\sigma(F^2)$. The final cell constants of $a = 23.7527(9)$ Å, $b = 12.0648(5)$ Å, $c = 25.981(1)$ Å, $\beta = 113.065(1)^\circ$, volume = 6850.2(5) Å³, are based upon the refinement of the XYZ-centroids of 4689 reflections above $2\sigma(I)$ with $3.72^\circ < 2\theta < 48.36^\circ$. Data were corrected for absorption effects using the multi-scan method (SADABS). The ratio of minimum to maximum apparent transmission was 0.788. The calculated minimum and maximum transmission coefficients (based on crystal size) are 0.5875 and 0.7453.

The structure was solved and refined using the Bruker SHELXTL Software Package, using the space group C 2/c, with $Z = 4$ for the formula unit, C₅₀H₇₀Cl₄N₄W₂•C₁₆H₃₂LiO₄. The final anisotropic full-matrix least-squares refinement on F^2 with 354 variables converged at $R1 =$

10.15%, for the observed data and $wR2 = 21.53\%$ for all data. The goodness-of-fit was 1.226.

The largest peak in the final difference electron density synthesis was $7.456 \text{ e}^-/\text{\AA}^3$ and the largest hole was $-3.690 \text{ e}^-/\text{\AA}^3$ with an RMS deviation of $0.265 \text{ e}^-/\text{\AA}^3$. On the basis of the final model, the calculated density was 1.485 g/cm^3 and $F(000)$, 3108 e^- .

Table 1. Sample and crystal data for **2**, $(\text{W}_2(\text{DippF})_2\text{Cl}_4\text{Li})$.

Name	$\text{W}_2(\text{DippF})_2\text{Cl}_4\text{Li}$	
Chemical formula	$\text{C}_{50}\text{H}_{70}\text{Cl}_4\text{N}_4\text{W}_2\cdot\text{C}_{16}\text{H}_{32}\text{LiO}_4$	
Formula weight	1531.94 g/mol	
Temperature	100(2) K	
Wavelength	0.71073 \AA	
Crystal size	0.100 x 0.100 x 0.050 mm	
Crystal habit	clear yellow block	
Crystal system	monoclinic	
Space group	C 2/c	
Unit cell dimensions	$a = 23.7527(9) \text{ \AA}$	$\alpha = 90^\circ$
	$b = 12.0648(5) \text{ \AA}$	$\beta = 113.065(1)^\circ$
	$c = 25.981(1) \text{ \AA}$	$\gamma = 90^\circ$
Volume	$6850.2(5) \text{ \AA}^3$	
Z	4	
Density (calculated)	1.485 g/cm^3	
Absorption coefficient	3.559 mm^{-1}	
$F(000)$	3108	

Table 2.Data collection and structure refinement for **2**, (W₂(DippF)₂Cl₄Li)

Theta range for data collection	1.86 to 24.18°
Index ranges	-27<= <i>h</i> <=27, -13<= <i>k</i> <=13, -29<= <i>l</i> <=29
Reflections collected	71366
Independent reflections	5451 [R(int) = 0.1140]
Coverage of independent reflections	99.4%
Absorption correction	multi-scan
Max. and min. transmission	0.7453 and 0.5875
Structure solution technique	direct methods
Structure solution program	SHELXT-2014/7 (Sheldrick, 2014)
Refinement method	Full-matrix least-squares on F ²
Refinement program	SHELXL-2014/7 (Sheldrick, 2014)
Function minimized	$\sum w(F_o^2 - F_c^2)^2$
Data / restraints / parameters	5451 / 361 / 354
Goodness-of-fit on F²	1.226
Δ/σ_{\max}	0.002
Final R indices	4689 data; I>2σ(I) R1 = 0.1015, wR2 = 0.2071 all data R1 = 0.1170, wR2 = 0.2153
Weighting scheme	w=1/[σ ² (F _o ²)+(0.0410P) ² +632.5916P] where P=(F _o ² +2F _c ²)/3
Largest diff. peak and hole	7.456 and -3.690 eÅ ⁻³
R.M.S. deviation from mean	0.265 eÅ ⁻³

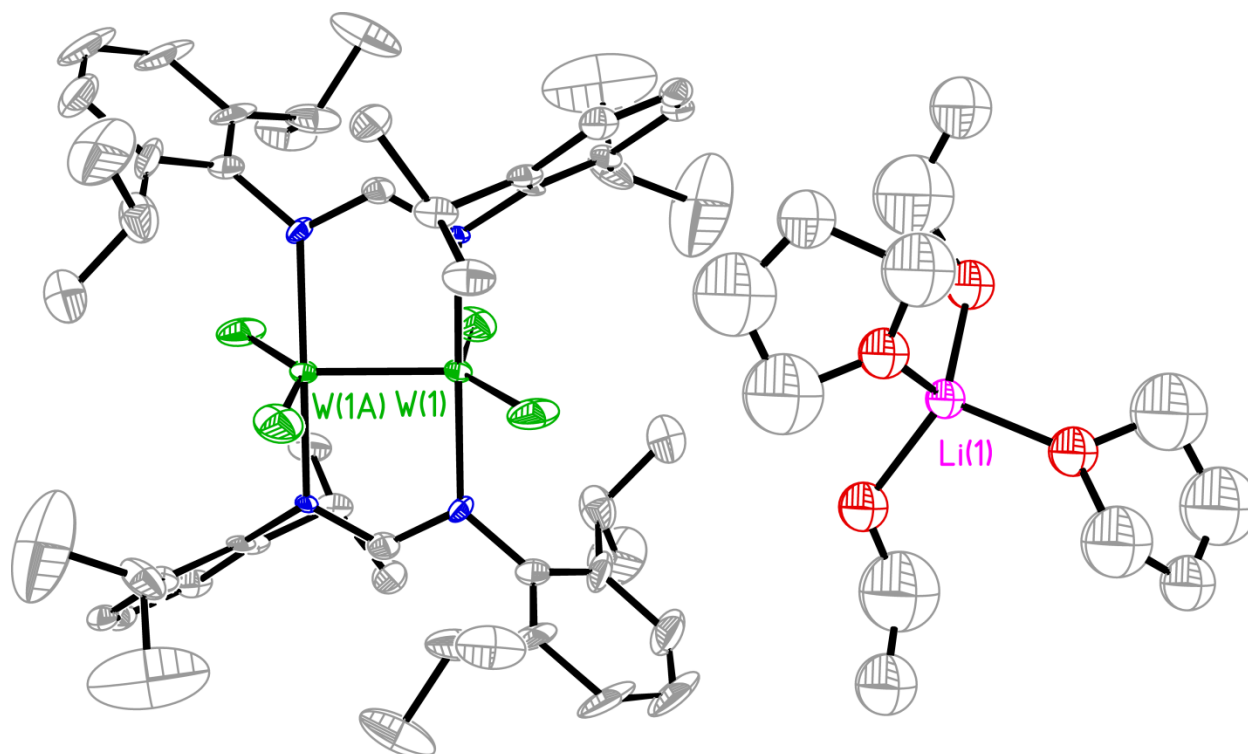


Figure 7. ORTEP diagram of **2** plotted at the 50% probability value. W(1)-W(1) distance 2.280(1) Å, W1-N(1) distance 2.130(1) Å.

2.4.2. X-ray Crystal Structure of **3**, $\text{W}_2(\text{DippF})_2\text{K}_2$

An amber- red plate-like specimen of $\text{C}_{116}\text{H}_{176}\text{K}_4\text{N}_8\text{O}_4\text{W}_4$, approximate dimensions 0.100 mm x 0.100 mm x 0.200 mm, was used for the X-ray crystallographic analysis. The X-ray intensity data were measured.

The total exposure time was 8.55 hours. The frames were integrated with the Bruker SAINT software package using a narrow-frame algorithm. The integration of the data using a triclinic unit cell yielded a total of 28893 reflections to a maximum θ angle of 20.84° (1.00 Å resolution), of which 6451 were independent (average redundancy 4.479, completeness = 96.6%, $R_{\text{int}} = 9.71\%$, $R_{\text{sig}} = 7.40\%$) and 4600 (71.31%) were greater than $2\sigma(F^2)$. The final cell constants of $a = 10.879(2)$ Å, $b = 13.364(3)$ Å, $c = 23.272(5)$ Å, $\alpha = 96.119(6)^\circ$, $\beta = 99.340(6)^\circ$, $\gamma = 105.700(6)^\circ$,

volume = 3173.4(11) Å³, are based upon the refinement of the XYZ-centroids of 7004 reflections above 2 σ(I) with 5.862° < 2θ < 41.61°. Data were corrected for absorption effects using the multi-scan method (SADABS). The ratio of minimum to maximum apparent transmission was 0.781. The calculated minimum and maximum transmission coefficients (based on crystal size) are 0.3140 and 0.5190.

The structure was solved and refined using the Bruker SHELXTL Software Package, using the space group P -1, with Z = 1 for the formula unit, C₁₁₆H₁₇₆K₄N₈O₄W₄. The final anisotropic full-matrix least-squares refinement on F² with 603 variables converged at R1 = 7.40%, for the observed data and wR2 = 24.46% for all data. The goodness-of-fit was 1.113. The largest peak in the final difference electron density synthesis was 2.715 e⁻/Å³ and the largest hole was -2.428 e⁻/Å³ with an RMS deviation of 0.282 e⁻/Å³. On the basis of the final model, the calculated density was 1.377 g/cm³ and F(000), 1326 e⁻.

Table 3. Sample and crystal data for **3**, (W₂(DippF)₂K₂).

Name	W ₂ (DippF) ₂ K ₂	
Chemical formula	C ₁₁₆ H ₁₇₆ K ₄ N ₈ O ₄ W ₄	
Formula weight	2638.44 g/mol	
Temperature	100(2) K	
Wavelength	0.71073 Å	
Crystal size	0.100 x 0.100 x 0.200 mm	
Crystal habit	Amber red plate	
Crystal system	triclinic	
Space group	P -1	
Unit cell dimensions	a = 10.879(2) Å	α = 96.119(6)°
	b = 13.364(3) Å	β = 99.340(6)°
	c = 23.272(5) Å	γ = 105.700(6)°
Volume	3173.4(11) Å ³	
Z	1	
Density (calculated)	1.377 g/cm ³	
Absorption coefficient	3.791 mm ⁻¹	
F(000)	1326	

Table 4. Data collection and structure refinement for **3**, (W₂(DippF)₂K₂).

Theta range for data collection	2.39 to 20.84°
Index ranges	-10<= <i>h</i> <=10, -13<= <i>k</i> <=13, -23<= <i>l</i> <=23
Reflections collected	28893
Independent reflections	6451 [R(int) = 0.0971]
Coverage of independent reflections	96.6%
Absorption correction	multi-scan
Max. and min. transmission	0.5190 and 0.3140
Structure solution technique	direct methods
Structure solution program	SHELXT-2014/7 (Sheldrick, 2014)
Refinement method	Full-matrix least-squares on F ²
Refinement program	SHELXL-2014/7 (Sheldrick, 2014)
Function minimized	$\Sigma w(F_o^2 - F_c^2)^2$
Data / restraints / parameters	6451 / 661 / 603
Goodness-of-fit on F²	1.113
Δ/σ_{\max}	0.004
Final R indices	4600 data; I>2σ(I) R1 = 0.0740, wR2 = 0.2002 all data R1 = 0.1165, wR2 = 0.2446
Weighting scheme	w=1/[σ ² (F _o ²)+(0.1196P) ² +135.4914P]
Largest diff. peak and hole	2.715 and -2.428 eÅ ⁻³
R.M.S. deviation from mean	0.282 eÅ ⁻³

Table 5. Calculated and experimental data for compound **3**

Model	Atoms	Calculated Distance (Å)	Experimental Distance (Å)	Total Energy (Hartrees)	Experimental Raman (cm-1)	Calculated Raman (cm- 1)
3	W(1)-W(1A)	2.21	2.407(1)	-2302.17584346	299.4	313 (W-W)
	W(1)-N(1)	2.13	2.120(1)			
	W(1)-N(2A)	2.13	2.110(1)			

2.5. Results and Discussion

The multi-step synthesis of the title compound starts with WCl_6 as a starting material, which is reacted with W(CO)_6 to form WCl_4 as depicted in Scheme 1. Reduction of WCl_4 with KC_8 in the presence of stoichiometric amounts of the lithium salt of DippF, yields the bimetallic precursor **1** (26% yield) which has a W_2^{6+} core. A cyclic voltammogram (CV) of **1**, Figure 11, shows a reversible reduction at -1.28 V (vs Fc/Fc^+) followed by an irreversible reduction at -1.89 V. A third reversible reduction event at -2.28 V is also observed.

Reduction of **1** with one equivalent of lithium metal in THF yields **2** in 99% yield. Compound **2** has been characterized by x-ray crystallography, and has a W-W bond distance of 2.280(1) Å.

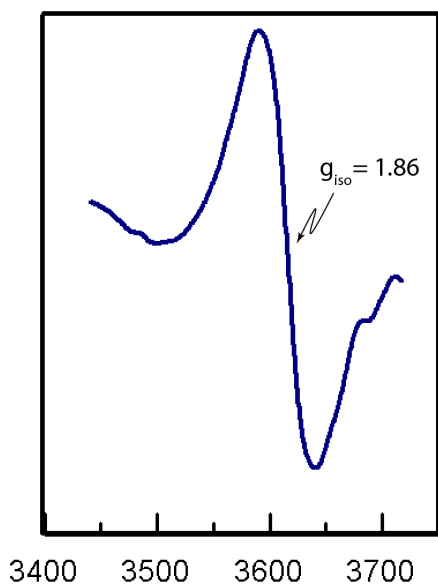


Figure 8. EPR spectrum of compound **2** showing an isotropic signal with a g value of 1.86

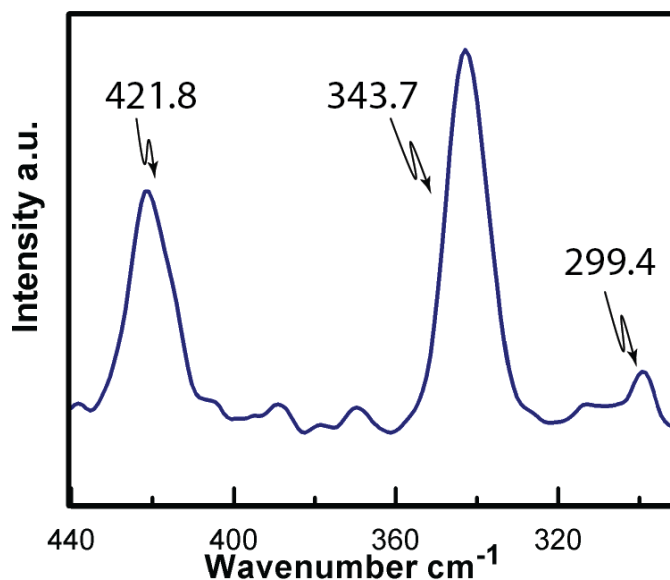


Figure 9. Raman spectra for **3**. The $\nu(\text{W-W})$ can be observed at 299.4 cm^{-1} . Strong ligand vibrations were observed at 343.7 and 421.8 cm^{-1}

This distance is consistent with a bond order of 3.5.⁴⁷ NMR spectroscopy shows broad signals consistent with having a paramagnetic sample. EPR spectroscopy shows an anisotropic signal with $g = 1.86$ (Figure 8) also in agreement with similar W-W complexes with bond order of 3.5.^{9,31,48}

Reduction of **1** in refluxing THF with excess potassium sand yields **3** in 14% yield (Scheme 1.V). Crystals grown at $-10\text{ }^{\circ}\text{C}$ from a concentrated solution of **3** in ether were analyzed under single-crystal x-ray diffraction. The structure of **3** is shown in Figure 4.

The W–W bond distance of $2.407(1)\text{ }\text{\AA}$ is longer than the range of classical $\sigma^2\pi^4\delta^2$ quadruply bonded complexes (spanning distances between $2.155(2)\text{ }\text{\AA}$ and $2.375(1)\text{ }\text{\AA}$).^{9,49} The bond distances between the metal center and the N atom in the ligand are between $2.081(2) - 2.121(2)\text{ }\text{\AA}$. The distances between the potassium cations and the isopropyl groups of the ligand fall in the range of $3.262(6) - 3.303(4)\text{ }\text{\AA}$. On the other hand the distances between the isopropyl groups and the W atoms are between $2.216(2) - 2.223(6)\text{ }\text{\AA}$.

DFT calculations were performed on a geometry optimized dianionic model of **3** to gain insight into its electronic structure. The top six highest occupied molecular orbitals of the model of **3** shows that they all are metal based (Figure 5). Starting from HOMO-5 and going up in energy until the HOMO, we see the molecular orbital manifold of bimetallic systems with D_{2h} symmetry,^{32,50–52} namely a σ -orbital (HOMO-5, 93% metal character), two π -orbitals close in energy (but not degenerate) (HOMO-4 and HOMO-3, 82 and 96% metal character, respectively), a distorted δ -orbital composed by two d_x^2 orbitals (HOMO-2, 87% metal), a second δ -orbital formed by two d_{xy} orbitals (51% metal), and finally a δ^* antibonding orbital as the HOMO (79% metal). The HOMO has a large s orbital contribution to the MO (22% s orbital character vs 20% d orbital character) also consistent with previous calculations on similar W_2 systems.⁵³ This molecular orbital manifold shows that the net bond order of this system is four and it is consistent with the experimentally observed long W–W distance. The electronic spectrum of **3** shows a broad signal from 600 to 350 nm (Figure 10) suggesting the availability of low-lying excited states.⁵⁴

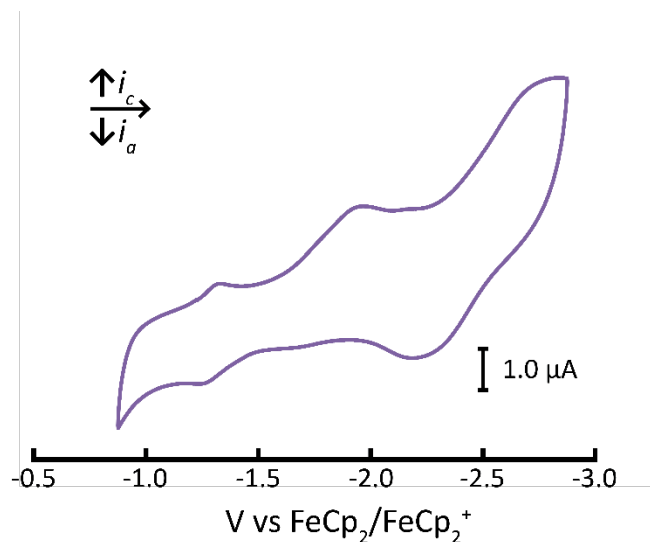


Figure 11. Cyclic voltammogram of **1** depicting two reversible redox events and one non-reversible oxidation

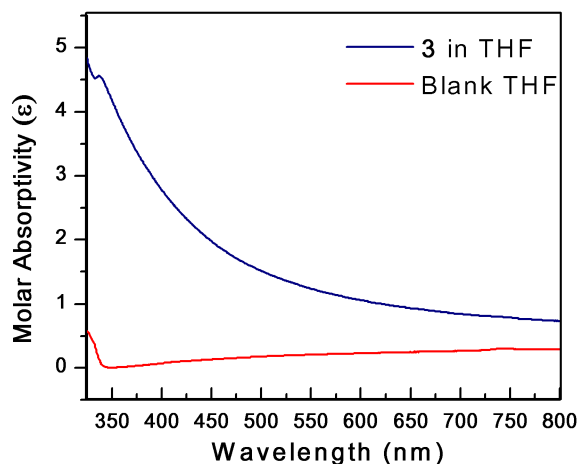


Figure 10. UV-vis spectrum of compound **3**.

The strong π interactions between the metal and the ligand are described pictorially in Figure 12. The π system of each DippF ligand yields three orbitals composed of different combinations of the NCN pz orbitals, namely a bonding combination (all pz orbitals in phase), a non-bonding (no pz character in the central C atom), and an antibonding orbital combination (left side of Figure 12, from bottom to top). Since there are two DippF ligands, the in-phase and out-of-phase interactions of each are expected. In an idealized D_{2h} symmetry each combination has the following Mulliken labels: b_{3g} , b_{1u} for bonding, a_u , b_{2g} for non-bonding and b_{3g} , b_{1u} for antibonding. The bonding and nonbonding orbitals are occupied, while the antibonding orbital is not.⁵⁵

The out-of-phase combinations of the bonding, non-bonding and antibonding (b_{3g} , a_u , and b_{3g} respectively) interact with one set of the δ and δ^* . The ligand based antibonding b_{3g} interacts with the b_{3g} δ orbital. The empty π^* b_{3g} stabilizes the delta b_{3g} in a back-bonding interaction. In the potassium salt of the deprotonated DippF ligand the carbon-nitrogen distances of the NCN π

system are 1.312(3) and 1.319(3) Å.⁵⁶ When DippF is associated to the ditungsten core, W₂, in **3** those distances increase to 1.37(3) and 1.36(3) Å, suggesting that the b_{3g} antibonding ligand orbital is occupied, and consistent with the depicted molecular orbital in Figure 12.⁵⁷

Three signals of different intensity were observed in the Raman spectrum of **3** (Figure 9). We assigned these vibrations with the aid of DFT calculations. Strong signals at 343.7 and 421.8 cm⁻¹ are attributed to ligands vibrations while a signal centered at 299.4 cm⁻¹ corresponds to the tungsten-tungsten vibration which is in the range of quadruply bonded systems.⁹

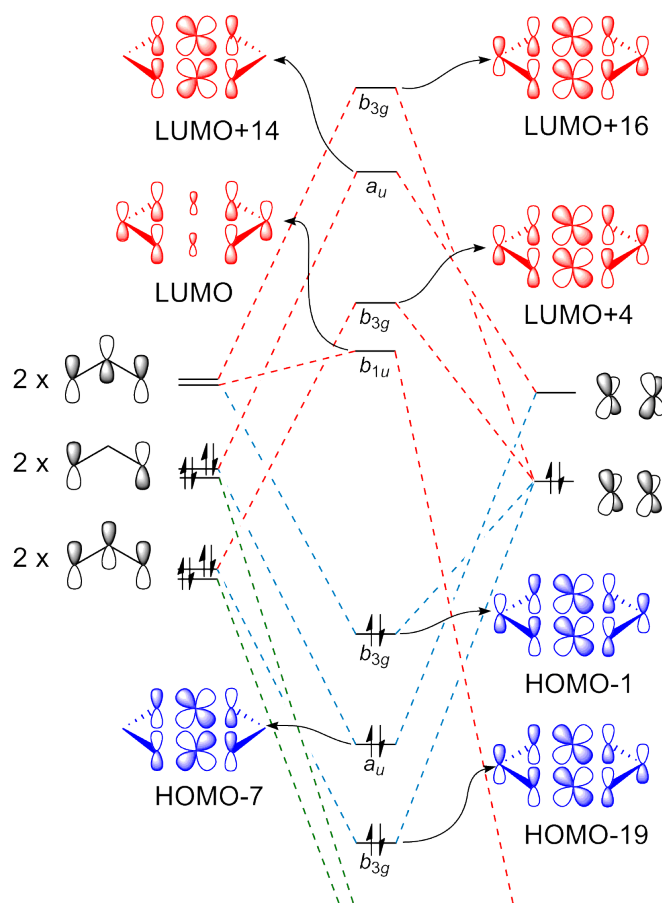


Figure 12. Molecular orbital depicting ligand-metal interactions of compound **3**

2.6. Conclusion

To the best of our knowledge, compound **3** is the first example of a M_2 core with a metal center in the zero oxidation state with π -donating ligands. Moreover, the low oxidation state of the metal centers makes this an unprecedented electron rich metal core. We are currently working on oxidizing **3** to yield the W(I)-W(I) analog to those of the Cr_2 and Mo_2 quintuply bonded complexes,^{32,50,52} as well as exploring its reactivity.

Chapter III: Introducing students to inner sphere electron transfer concepts through electrochemistry studies in diferrocene mixed-valence systems[†]

3.1. Introduction

Electrochemistry is an important topic in undergraduate chemistry, since it deals with the fundamental basis of all chemical reactions: the transfer of electrons across an interface.⁵⁸ However, to our knowledge, few laboratory practices for third year undergraduate students, deal with electrochemistry and the effects of inner-sphere (through bond) and/or outer sphere (through space) electron transfer.⁵⁹ Fundamental studies of electron transfer (ET) are critical for our understanding of the basic chemistry of energy conversion.⁶⁰ The electron transfer rate, a critical property in this context is simply defined as the rate at which an electron can move from one system (electron donor) to another (electron acceptor). This rate is explained in detail by the Marcus Theory.⁶¹

Ever since evidence of their existence was presented more than 40 years ago, the electronic structure of mixed-valence complexes has become one of the most studied fields in physical chemistry. In 1969, a historical report from Creutz and Taube described an inter-valence charge transfer band in a symmetrical mixed-valence system, in which the initial and final electronic states were degenerate.⁶² This system is known as the Creutz-Taube ion ($[(\text{NH}_3)_5\text{Ru}(\text{pyrazine})\text{Ru}(\text{NH}_3)_5]^{5+}$) where each Ru is considered to have an oxidation state of 2.5+ (Figure 13).⁶³

[†] This chapter has previously appeared as an article in the Journal of Chemical Education. The original citation is as follows: Karen Ventura, Mark B. Smith, Jacob R. Prat, Lourdes E. Echegoyen and Dino Villagrán; Introducing Students to Inner Sphere Electron Transfer Concepts through Electrochemistry Studies in Diferrocene Mixed-Valence systems. *J. Chem. Edu.*, **2017**, 94, pp.526-529

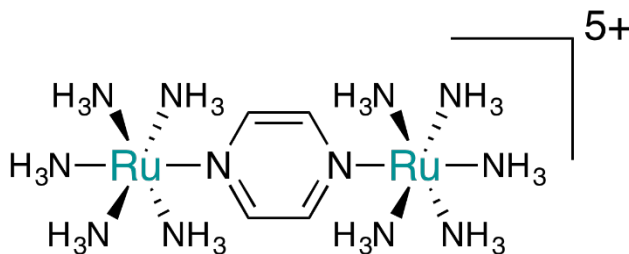
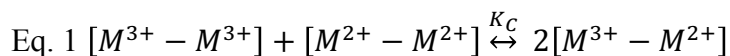


Figure 13. The famous Creutz-Taube ion studied as a platform for the study of inner-sphere electron transfer. Henry Taube was awarded the Nobel Prize in 1983.

The Creutz-Taube ion and its analogs provide an excellent platform for studying inner-sphere electron transfer mechanisms. Like the original, analogs of the Creutz-Taube ion are composed of two redox active centers bridged by an organic linker.^{64–71} Comparing electrochemical data corresponding to the redox events of the mixed valence system to that of the reactant neutral and doubly oxidized species, we can obtain equilibrium constants that relate the degree of electronic communication (electronic coupling) between the redox centers.¹⁷

The complexity of the chemical compounds needed and the lack of proper instrumentation may be reasons for the few available experiments in teaching laboratories that discuss ET. However, through cyclic (CV) or differential pulse voltammetries (DPV) we can obtain basic information about the degree of electronic communication between two redox centers, M^{2+} and M^{3+} , by determining the equilibrium constant of the comproportionation reaction shown in eq. 1.



We can use the Nernst equation to determine the equilibrium constant (K_c) of a system using equation 2.

$$\text{Eq. 2 } K_c = e^{\left(\frac{F\Delta E_{1/2}}{RT}\right)}$$

where F and R are the Faraday and gas constants, respectively, and T is temperature.

Once K_c is known, the Robin-Day classification can aid us in determining the degree of electronic communication between systems:

Class I $K_c < 10^2$

Class II $10^2 \leq K_c \leq 10^6$

Class III $K_c > 10^6$

We present here a simple experimental procedure to determine ET rates in mixed-valence compounds using two diferrocene platforms joined through a dimethyl alkene bridge. These experiments may be implemented in upper division physical chemistry and/or synthetic inorganic chemistry laboratories at the undergraduate level.

3.2.Laboratory description

The experiment described herein has been part of the first semester physical chemistry (junior level) laboratory at the University of Texas at El Paso since Spring 2014. The average class size is 15 students, divided in two sections of 7-8 students. The students were required to work in groups of two. A step-by-step procedure, laboratory report requirements, and a sample quiz can be found in the Supplementary Information. We prepare students for the lab experiment with an interactive presentation that provides background on ET, a fundamental explanation of the electrochemical methods to be used and a detailed explanation of the experimental procedure. A quiz prior to the start of the presentation incentivizes students to be prepared and to understand

the concepts to be studied before the laboratory practice. Assessment results of this laboratory practice are shown in table 1.

Table 6. Comparison of the Assessment Results for the Pre-lab Quiz and Lab Report

Evaluation Instrument	Score by Year %			
	2014, N = 20	2015, N = 13	2016, N = 13	Total, N = 46
Quiz	67.20	65.77	79.28	70.21
Lab Report	70.45	89.50	89.88	81.33

To study inner-sphere ET, we use two Creutz-Taube analogs, (E) and (Z)-dimethylferrocenylethylene, **2** and **3** respectively (Figure 14). Both compounds consist of two ferrocene molecules linked by a dimethylethylene linker. Each ferrocene center initially is

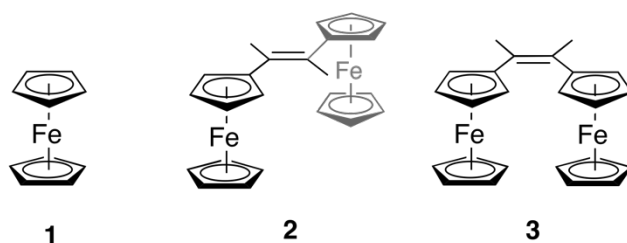
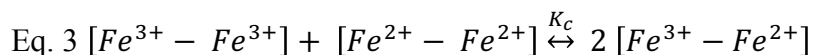


Figure 14. Diferrocene complexes used in this laboratory practice

divalent. Upon a one-electron oxidation, a mixed-valent complex is formed. Upon a second electron oxidation the comproportionation reaction shown in equation 3 below describes the equilibrium between the $\text{Fe}^{2+}\text{-Fe}^{2+}$ and the $\text{Fe}^{3+}\text{-Fe}^{3+}$ species that yields a mixed-valent complex. The extent of the electronic communication between the two ferrocene centers can be studied by measuring the equilibrium of the comproportionation reaction of **2** (or **3**).



The electronic communication between the redox centers was measured via cyclic (CV) and differential pulse voltammetry (DPV) methods using a 760 CH Instrument (CHI) potentiostat.

We used a standard 10 mL single-compartment electrochemical cell equipped with a stir bar whose cap is designed to prevent the electrodes from touching each other to avoid shorting the circuit (Figure 15). A standard three-electrode cell consisting of a freshly polished platinum working electrode (2 mm diameter), a platinum wire counter electrode and a Ag/AgCl reference electrode were used for all measurements. The cell was purged with a flow of nitrogen for 5 minutes before each initial run, and for about 30 seconds between each subsequent measurement. A scan rate of 100 mV per second was used.

The dimers were prepared by the instructor or teaching assistant prior to the laboratory practice (for details on the synthetic procedures refer to the Supplementary Information) and were given to the students in a capped vial. However, this laboratory can be coupled with an advanced inorganic or organometallic synthesis lab, where students synthesize, separate and characterize the dimers. The modified synthesis we report is simple and can be finished in two three-hour sections.¹⁸ We prepare these complexes through a McMurry coupling reaction

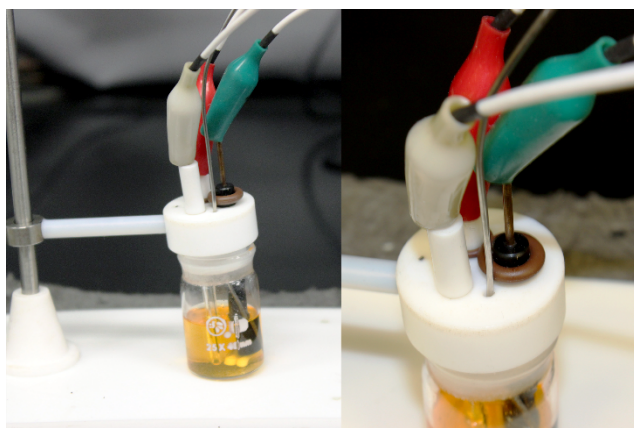


Figure 15. Experimental setup for the electrochemical measurements. The cap is designed to hold the working electrode (Green), the reference electrode (white), the counter electrode (red) and a purging needle

between two acetylferrocene molecules in the presence of zinc powder under a nitrogen atmosphere.⁷² Purification via column chromatography gives a mixture of both isomers, which

can be separated by taking advantage of the difference in their solubility in benzene. Compound **2** is much less soluble in benzene, making it easy to isolate in good yields (51%).

For the mixed-valency studies, students prepare a 10 mL dichloromethane solution of **2** (1.0 mM) and tetrabutylammonium hexafluorophosphate as the electrolyte (0.1 M). The solution is transferred to the electrochemical cell and nitrogen gas is bubbled for one minute to remove oxygen. Figure 15 shows the three-electrode set up used with each electrode connected to the potentiostat via alligator clips. Students repeat the same experimental set up with compound **3**, and finally, they do it again with ferrocene (**1**) as the reference experiment. If needed, this experiment may be further simplified by using only one of the two isomers since the electrochemical data of **2** and **3** are similar. Because **2** is easier to purify, it may be chosen over **3**.

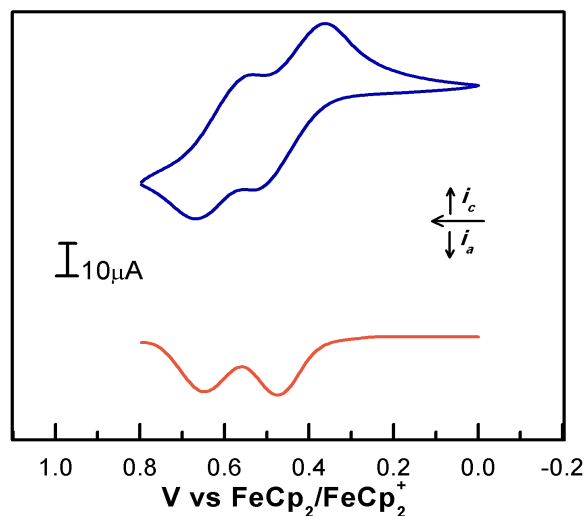


Figure 16. Cyclic voltammogram and differential pulse voltammogram of **2**

3.3. Materials and methods

3.3.1. General.

Standard vacuum line and Schlenk techniques under nitrogen atmosphere were used for the first part of the synthesis of **1** and **2**. Titanium (IV) chloride, ferrocene, and acetylferrocene were purchased from Aldrich and were used as is. Zinc powder purchased from STREM was activated with 1% aqueous HCl; washed with distilled water, ethanol, and ether; and dried in an oven (140°C) prior to use. THF was dried and degassed using a Pure Process Technology solvent purification system prior to use.

3.3.2. Physical Measurements.

A 760 CH Instruments (CHI) potentiostat with the capacity to perform CV and DPV was used. A 10 mL single-compartment electrochemical cell equipped with a stir bar was used for all measurements. The cap of the cell is designed to simplify the setup of the electrodes. It is important to ensure that the electrodes do not come into contact with each other or other metallic parts such as clamps. A freshly polished platinum working electrode (2 mm diameter), a platinum wire counter electrode and a Ag/AgCl reference electrode were used for all the measurements described. The cell was purged with a flow of nitrogen for 5 minutes before each run.

3.3.3. Synthesis of E and Z-dimethylferrocene dimers.

The E and Z-dimethylferrocene dimers were synthesized prior to the scheduled laboratory practice using a modified version of a previously published procedure.¹⁸ In a Schlenk flask a mixture of zinc powder (1.6 g, 24 mmol, CAS: 7440-66-6) and 40 mL of THF were cooled down to -94°C (acetone and liquid N₂ bath). Once cooled, TiCl₄ (1.3 mL, 12 mmol, CAS: 7550-45-0)

was slowly added with a syringe. The suspending mixture was warmed to room temperature and stirred for 0.5 h, then heated to reflux for 2.5 h. The resulting mixture was again cooled down to 0°C (ice bath) and a solution of acetylferrocene (0.96 g, 4.2 mmol CAS: 1271-55-2) in 15 mL of THF was slowly added. The reaction was heated to reflux once more until the carbonyl compounds were consumed. The reaction was then quenched with a 10% K₂CO₃ (CAS: 6381-79-9) aqueous solution and the dimers extracted with CH₂Cl₂. The crude was subject to chromatographic separation on a neutral alumina column. Elution with a mixture of hexane:dichloromethane (10:1 v/v) afforded a light orange band for **1** and **2**. The separation of the dimers was possible due to the fact that the E isomer is much more soluble in benzene. ¹H NMR spectroscopy for **1** (signals for **2** are shown in parenthesis) (CDCl₃): δ 4.32 (4.32) (t, 2H, *m*-Cp), 4.23 (4.23) (t, 2H, *o*-Cp), 4.17 (4.07) (s, 5H, Cp), 2.16 (2.12) (s, 3H, CH₃). ESI-MS [M+H]⁺: Calcd. 424.16, found 425.30 m/z.

3.4.Hazards

MSDS data indicates that (1) acetyl ferrocene may cause eye and skin irritation, and it is poisonous if swallowed; (2) dichloromethane causes skin, eye and respiratory tract irritation, may cause central nervous system effect, and possible cancer after chronic exposure; (3) ferrocene is hazardous when ingested. Therefore, the use of goggles, gloves and lab coat is advised. If students perform the synthesis of **2** and **3**, extreme caution must be exercised when refluxing the mixture due to elevated temperatures and pressures. Hoses connected to the condenser must be properly secured in order to avoid any potential accidents.

3.5. Results and Discussion

3.5.1. Electrochemistry

The cyclic voltammogram of **2** and **3** reveal that each compound has two reversible redox events as shown in Figures 16 and 17. For **2**, the $E_{1/2}$ for the first event is found at 0.451 V and the second at 0.609 V. The differential pulse voltammogram (DPV) for compound **2** shows two oxidation events, E_a , at 0.472 and 0.656 V (Figure 16). For **3**, the first redox event has an $E_{1/2}$ of

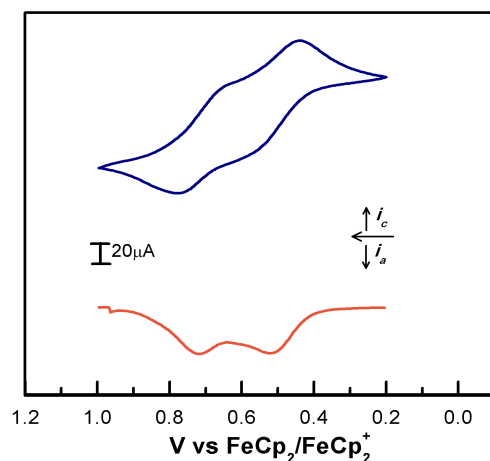


Figure 17. Cyclic voltammogram and differential pulse voltammogram of **3**.

0.537 V while the second redox event has an $E_{1/2}$ of 0.717 V. Two oxidations are observed in the DPV of compound **3** at 0.512 and 0.724 V (Figure 17). We can measure the equilibrium constant of the reaction of both compounds by using equation 2. This results in $K_c = 4.7 \times 10^2$ for compound **2** and $K_c = 1.1 \times 10^3$ for compound **3**, in agreement with literature values. Both compounds fall under Class II for the Robin-Day classification system.^{73–76}

3.6. Conclusion

We present here the use of two diferrocene dimer isomers as platforms for the study of ET in mixed valence systems. By determining the equilibrium constant of the comproportionation

reaction that yields the mixed-valence complex we can measure the electronic communication between the ferrocene centers and catalogue these complexes according to the Robin Day classification. We can compare and contrast the electronic communication with respect to simple ferrocene. Comproportionation constants, K_c , of 4.7×10^2 and 1.1×10^3 were obtained for dimers (E) and (Z) (**1** and **2** respectively), which correspond to Class II in the Robin-Day classification. These complexes are stable in air, making their handling appropriate for upper division teaching laboratories

Chapter IV: Superparamagnetic MOF@GO Ni and Co based hybrid nanocomposites as efficient water pollutant adsorbents[‡]

4.1. Introduction

Mesoporous materials and metal-organic frameworks (MOFs) are used in various fields such as gas storage, gas separation and purification, electrode materials, drug delivery, polymerization, catalysis, carriers for nanomaterials, luminescence, magnetism, membranes, imaging and water remediation.^{77–85} In the past decade, there has been increased interest in the use of MOFs as adsorbents in the removal of hazardous and toxic pollutants due to their high specific surface area, numerous pore openings, as well as functional groups, which are useful for selective adsorption.^{86–89} MOFs are high surface area materials made of metal ions or metal clusters coordinated to organic ligands (linkers). The specific interest in MOF materials arises from their shape and pore size distribution tunability from the microporous to the mesoporous scale. These factors depend on the connectivity of the central metal and ligands as well as in the nature of the linkers used.^{79–81} The properties of MOFs can be further enhanced by grafting active groups,⁹⁰ changing organic ligands,⁹¹ and making composites of MOFs with appropriate materials; as such, MOF research is expanding towards improving their absorption properties through synergistic effects.^{92–98} However, the compositing of MOFs with appropriate materials requires further understanding of the synthetic methods,⁹⁹ corresponding reaction kinetics, as well as resulting morphology¹⁰⁰ and physicochemical properties.^{83,97,101–103} Among the most

[‡] This chapter has been submitted as an article in ACS Omega. The original submission is as follows: Karen Ventura, Vahid Jabbari, Roy A. Arrieta, Camilah D. Powell, Reagan Turley, Amanda W. Lounsbury, Jonathan G. Gracida, Jerrin S. Philip, Julie B. Zimmerman, Jorge Gardea-Torresdey, Michael S. Wong, Dino Villagrán.; Superparamagnetic MOF@go Ni and Co bades hybrid nanocomposites as efficient water pollutant adsorbents. *ACS Omega*, **Submitted**.

suitable materials on which to assemble MOF-based composites is graphene oxide (GO), where GO nanolayers are introduced as a support for MOFs synthesis.^{93,104–108}

The advantages of using a GO substrate in MOF formation include the increase of dispersive forces within MOFs and the directed structural growth of MOFs.^{101,102} Pure MOF structures are full of void and free spaces in between the nanocrystals due to weak dispersive forces, which has an adverse effect on the retention of small molecules. In contrast, GO has a nonporous structure with arrays of layers. Thus, by combining the synergistic features of these materials, hybrid nanocomposites with less inter-MOFs void space are produced.^{107,109} It is also hypothesized, though not yet shown, that graphene layers within GO can direct the structural growth of MOFs during synthesis, by controlling the morphology and size of MOFs during their formation.^{93,107,108} Recently, the synthesis of MOF-5 decorated GO (MOF-5@GO) resulted in retention of the porosity of MOF-5 with added flexibility and a well-developed functionality.⁹⁴ These enhancements were associated with the presence of GO during the formation of the MOF and the possible alternation of the GO sheets embedded with the MOF. A recent report of a Cu-BTC@GO nanocomposite shows that the nanocomposite has similar porosity in comparison to the individual MOF.⁹⁷ In gas adsorption studies, it was observed that adsorption of NH₃ and H₂S improved by 10% and 30%, respectively, for Cu₃(BTC)₂@GO compared to that of the parent MOF.^{97,106} Composites of GO with Zn-containing MOF, reported by Huang et al.,¹⁰⁷ demonstrated enhanced gas adsorption after GO was functionalized with MOFs. MOF-4 and Cu-BTC MOFs composites were reported with greater gas CO₂/CH₄ selectivity and H₂ uptake compared to the MOFs alone.^{93,108} In addition, superparamagnetic iron (III) oxide nanoparticles (Fe₃O₄ MNPs) are helpful in magnetic recovery and separation of adsorbent materials used in water and wastewater treatments.^{109,110} Due to the strong magnetic nature of Fe₃O₄ MNPs, its

loading over MOF@GO can further improve these adsorbents by making them magnetic. In addition, several studies have proven that Fe_3O_4 nanoparticles are a natural adsorbent and are helpful in the removal of arsenic, fluoride among other heavy metals, which may add additional adsorptive properties.^{111,112} Further, we have recently reported the use of $\text{Cu}_3(\text{BTC})_2$ based magnetic nanocomposite for the removal of methylene blue (MB).¹¹³ Therefore, the present work expands the scope of these original adsorbent materials to include improved synthetic methodologies based on Co and Ni MOFs and in the study of their adsorption properties of dyes and common ions. In addition, we are interested in exploring whether the synthetic manipulation of these composite materials affect the superparamagnetic properties of the Fe_3O_4 nanoparticles. This work describes the syntheses of novel adsorbents based on magnetic $\text{Ni}_3(\text{BTC})_2$ @GO and $\text{Co}_3(\text{BTC})_2$ @GO hybrid nanocomposites.

Several important factors were considered for this study: (1) the synthesis of nanocomposites based on MOF and GO is a growing area of research for the development of new nanoengineered materials with different potential applications; (2) previous work shows that in GO-MOFs composites, MOFs are the leading component, and result in admixtures rather than covalently bonded composites. We are interested in having the GO substrate as the dominant component in order to grow chemically-bonded nanoscale MOFs over the platform; (3) although there are reports on the application of MOF@GO materials which only address air purification and toxic gases adsorption,^{93,107–109} to the best of our knowledge, (aside from our earlier work)¹¹³ no study addressing adsorption of organic pollutants and common ions from brackish waters has been reported; (4) The decoration of MOF@GO with Fe_3O_4 MNPs has not been fully explored. Thus, studies on the synthesis of magnetic adsorbents of $\text{Fe}_3\text{O}_4/\text{Ni}_3(\text{BTC})_2$ @GO and $\text{Fe}_3\text{O}_4/\text{Co}_3(\text{BTC})_2$ @GO and in their application as an organic pollutant adsorbent has not been

reported. The prepared hybrid nanomaterials were characterized by powder X-ray diffraction (pXRD), X-ray photoelectron spectroscopy (XPS), scanning electron microscope (SEM), transmission electron microscope (TEM), and infra-red spectroscopy (IR). The pollutant adsorption capacity of the nanomaterials was tested using methylene blue as an organic pollutant model and as a surrogate for environmental contaminants.^{86,87,114–116} Due to the synergistic effects of three different components in the composite, the adsorption capacity of ions from model brackish water was also tested. We believe the present work provides useful insight into the synthesis of magnetic MOF-based nanomaterials of $\text{Ni}_3(\text{BTC})_2@\text{GO}$ and $\text{Co}_3(\text{BTC})_2@\text{GO}$, and their application in the adsorption of hazardous and toxic compounds. These composites can also be used as a reference in designing other types of MOF@GO hybrid materials.

4.2.Experimental

4.2.1. Materials and Methods

All the reagents, purchased from commercially available sources, were used as received. Standard Schlenk techniques were used to synthesize Fe_3O_4 nanoparticles.¹¹⁷ Milli-Q water was used for all the analytical tests and the preparation of the model brackish water, and reverse osmosis water was used for synthetic procedures. Pollutant adsorption experiments were conducted using methylene blue (MB) as an organic pollutant model. A typical measurement consisted of treating 10 ml of Milli-Q water with different concentrations of MB (12.5, 25, 50 and 100 ppm) with 5 mg of the adsorbents. The resulting mixture was vigorously stirred for 12 h. The nonmagnetic adsorbents were centrifuged and the magnetic adsorbents were magnetically separated from the suspension. The concentration of the remaining dye was analyzed through UV-vis spectroscopy (Figure 27 and 28). All of the adsorption experiments were run three times and the results were averaged. For the leaching and adsorption studies the same mass and volume

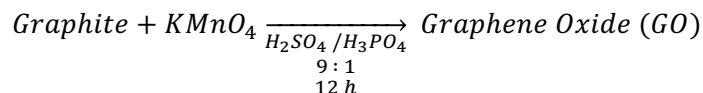
as the methylene blue studies were used. All tubes were sonicated for five minutes in order to break up any nanoparticle agglomeration, and then mixed for 24 hours on a tube rocker. After mixing, the tubes were removed from the rocker and centrifuged at 5000 rpm for 20 minutes to separate the samples from the solution. Since none of the samples are soluble in water, only suspended nanoparticles were intended to be removed through centrifugation. After centrifugation, 7.5 mL of each test solution was removed and added to a clean tube. 2.5 mL of a 12% nitric acid solution was added to each tube to bring the acid content to 3% by volume within each tube for ICP-MS and ICP-OES analysis.

4.2.2. Physical Measurements

Crystalline powder of the prepared samples were analyzed by X-ray powder diffractometer (XRD, Bruker D8 Discover X-ray Diffractometer). Morphological characterization of all samples was performed by using imaging techniques such as transmission electron microscopy (TEM, Hitachi H-7650), and scanning electron microscopy (either a SEM, Hitachi S-4800 or a Hitachi SU8230 UHR Cold Field Emission (CFE)). Samples were prepared as dilute suspensions of particles that were drop-coated onto carbon coated copper mesh (TEM) or silicon chips (SEM). IR spectroscopy was performed on a PerkinElmer® Universal ATR instrument in the range of 650–4000 cm^{-1} . X-ray photoelectron spectroscopy (XPS) tests were monitored by Omicron XPS/UPS system with Argus detector, which uses Omicron's DAR 400 dual Mg/Al X-ray source. The extent of MB removed by adsorbents was measured via a Shimadzu UV-1800 UV-Vis spectrometer. Adsorption analysis of ions was performed on a Perkin Elmer OPTIMA 4300 DV ICP-OES and leaching analysis was performed on a Perkin Elmer ELAN DRC II ICP-MS instrument. All magnetic measurements were performed using a Superconducting Quantum Interference Device (Quantum Design Magnetic Property Measuring system) at 300 K.

4.2.3. Synthesis of Graphene Oxide, 1

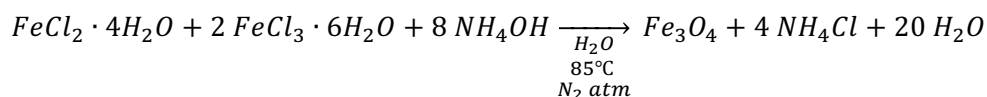
Graphene oxide was synthesized according to a previously reported method with slight modifications.¹¹⁸



Graphite flakes (3.0 g) were added to a 9:1 mixture of concentrated H₂SO₄/H₃PO₄ (180 mL:20 mL). To this suspension, KMnO₄ (18.0 g) was added slowly over a period of 5 minutes to avoid overheating. The reaction mixture was then heated to 50 °C and stirred for 12 hours. The mixture was cooled to room temperature and poured into ice (200 mL) with 30% H₂O₂ (3.0 mL). The remaining solid material was then filtered through a 150 mL M grade filter and washed with water, HCl, and ethanol three times. The remaining solid was washed with diethyl ether and dried under vacuum at room temperature.

4.2.4. Synthesis of Fe₃O₄ nanoparticles, 2

Fe₃O₄ magnetic nanoparticles were synthesized according to a previously reported method with slight modifications.¹¹⁷

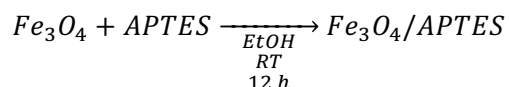


Fe₃O₄ magnetic nanoparticles were prepared by chemical co-precipitation of Fe³⁺ and Fe²⁺ ions with a molar ratio of 2:1. FeCl₃·6 H₂O (5.838 g) and FeCl₂·4 H₂O (2.147 g) were dissolved in 100 mL distilled water at 85°C under N₂ atmosphere and mechanically stirred. Then 10 mL of 25% NH₄OH were quickly injected into the reaction mixture. The formation of Fe₃O₄ black precipitate upon addition of the base was immediately observed. The reaction continued for 30

minutes and was cooled at room temperature. The Fe₃O₄ black precipitate was washed with 200 mL of water five times, a 0.02 M NaCl solution twice, and ethanol three times. All the washings were performed through magnetic decantation. The resulting magnetic powder was vacuum dried overnight at room temperature.

4.2.5. Synthesis of amino-silane functionalized Fe₃O₄ nanoparticles, 3

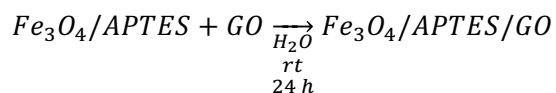
Functionalization of Fe₃O₄ nanoparticles with amino-silane was performed according to a previously reported method with slight modifications.¹¹⁹



Fe₃O₄ nanoparticles (2.0 g) were dispersed in 100 mL of ethanol via sonication for 30 minutes. The resulting dispersion was bubbled with N₂ gas for 15 minutes and 4 mL of (3-aminopropyl)triethoxysilane (APTES) were added while stirring. The mixture was left to react for 12 h at room temperature. The desired product was collected through magnetic decantation and washed with water, DMF, and ethanol. The product was dried overnight under vacuum.

4.2.6. Synthesis of magnetic graphene oxide (Fe₃O₄/GO), 4

Magnetic graphene oxide (Fe₃O₄/GO) was synthesized according to a previously reported method with slight modifications.¹¹⁹

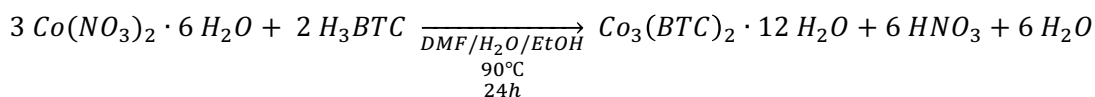


For the synthesis of magnetic graphene oxide 2.0 g of Fe₃O₄/APTES and 0.5 g of graphene oxide were completely dispersed in 80 mL of water respectively. The GO suspension was poured into the Fe₃O₄/APTES suspension under mechanical stirring. After stirring at room temperature for

24 hours, the prepared product was magnetically separated from the unreacted material and washed with water for three times. Finally, the composite was washed with ethanol three times and dried under vacuum overnight.

4.2.7. Synthesis of $\text{Co}_3(\text{BTC})_2 \cdot 12 \text{H}_2\text{O}$ MOF, 5

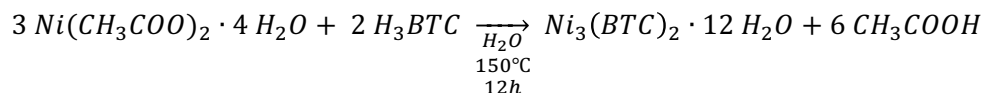
$\text{Co}_3(\text{BTC})_2 \cdot 12 \text{H}_2\text{O}$ was synthesized according to a previously reported method with slight modifications.¹²⁰



For the synthesis of $\text{Co}_3(\text{BTC})_2 \cdot 12 \text{H}_2\text{O}$, first $\text{Co}(\text{NO}_3)_2 \cdot 6 \text{H}_2\text{O}$ (3.7857g) and H_3BTC (1.8223g) were dissolved in a 45 mL mixture of DMF/water/ethanol (1:1:1) aided by sonication. The resulting dark pink-purple clear solution was transferred to a glass pressure vessel. The solution was heated at 90°C for 24 hours. A thick layer of pink-purple $\text{Co}_3(\text{BTC})_2 \cdot 12 \text{H}_2\text{O}$ crystals formed at the bottom of the vessel. The vessel was allowed to cool at room temperature. The solvent was subsequently decanted and the solid washed with DMF and ethanol. The product was exposed to a slight flow of air, and after six hours, the pink-purple needle crystals were dried.

4.2.8. Synthesis of $\text{Ni}_3(\text{BTC})_2 \cdot 12 \text{H}_2\text{O}$ MOF, 6

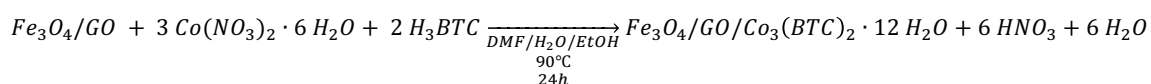
$\text{Ni}_3(\text{BTC})_2 \cdot 12 \text{H}_2\text{O}$ was synthesized according to a previously reported method with slight modifications.¹²¹



$\text{Ni}(\text{CH}_3\text{COO})_2 \cdot 4 \text{H}_2\text{O}$ (1.3885 g) and H_3BTC (0.7817g) were dissolved in 25 mL of water respectively aided by sonication. The two solutions were mixed and the resulting green clear

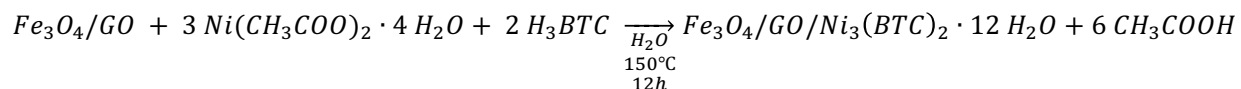
solution was transferred to a glass pressure vessel. The solution was heated at 150°C for 24 h. A thick layer of green $\text{Ni}_3(\text{BTC})_2 \cdot 12 \text{H}_2\text{O}$ crystals formed at the bottom of the vessel. The vessel was allowed to cool at room temperature. The solvent was subsequently decanted and the solid washed with DMF and ethanol. The product was exposed to a slight flow of air and after 6 hours the light green crystals were dried.

4.2.9. Synthesis of Composite $\text{Fe}_3\text{O}_4/\text{GO}/\text{Co}_3(\text{BTC})_2 \cdot 12 \text{H}_2\text{O}$, 7



$\text{Co}(\text{NO}_3)_2 \cdot 6 \text{H}_2\text{O}$ (300 mg) and H_3BTC (145 mg) were dissolved in a 45 mL mixture of DMF/water/ethanol (1:1:1) aided by mechanical stirring in a glass pressure vessel. $\text{Fe}_3\text{O}_4/\text{GO}$ (500 mg) was added to the solution mixture solution and was heated to 90°C for 24 hours under slight mechanical stirring to avoid precipitation of the composite and to obtain a uniform sample. The resulting product was cooled to room temperature. Subsequently the solvent was decanted and washed with DMF, water, and ethanol. All the washings were performed through magnetic decantation. Finally, the product was vacuum dried overnight at room temperature.

4.2.10. Synthesis of Composite $\text{Fe}_3\text{O}_4/\text{GO}/\text{Ni}_3(\text{BTC})_2 \cdot 12 \text{H}_2\text{O}$, 8

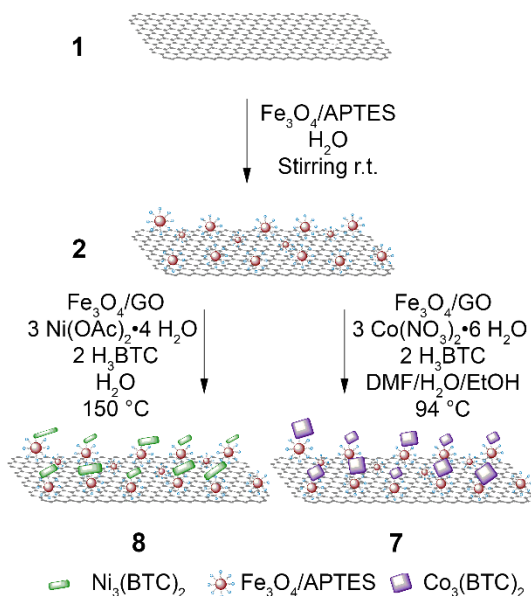


$\text{Ni}(\text{CH}_3\text{COO})_2 \cdot 4 \text{H}_2\text{O}$ (215 mg) and H_3BTC (105 mg) were dissolved in 45 mL DI H_2O aided by mechanical stirring in a glass pressure vessel. $\text{Fe}_3\text{O}_4/\text{GO}$ (500 mg) was added to the solution and was heated to 150°C for 12 h under slight mechanical stirring to avoid, precipitation of the composite and to obtain a uniform sample. The resulting product was cooled to room temperature. The solvent was then decanted and the materials were washed three times with

DMF, water, and ethanol. All the washings were performed through magnetic decantation.

Finally, the product was vacuum dried overnight at room temperature.

Scheme 2. Synthesis of compound **8** and **7**.



4.3. Results and Discussions

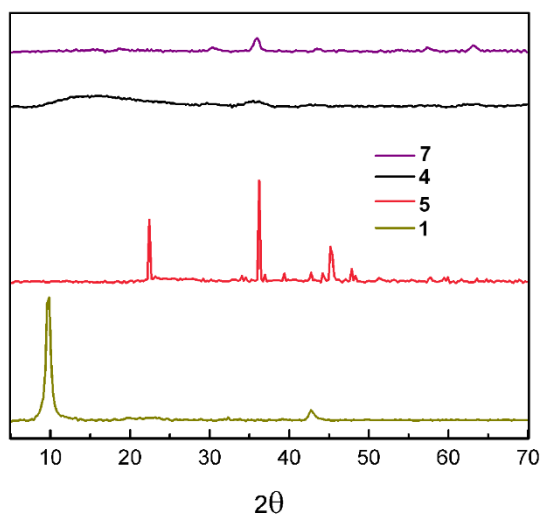


Figure 18. XRD spectrum of the Co nanocomposite, **7** (top) compared to the spectra of the parent materials (Fe₃O₄@GO, **4**; Co₃(BTC)₂, **5**; GO, **1**).

XRD patterns of the prepared Ni₃(BTC)₂ MOF-based hybrid nanocomposite, **8**, as well as the Co₃(BTC)₂ MOF-based hybrid nanocomposites, **7**, are shown in Figures 18 and 19. When

comparing the spectra of the parent materials against the spectra of the synthesized nanocomposites, the latter contains characteristic peaks of the spectra of the parent materials.

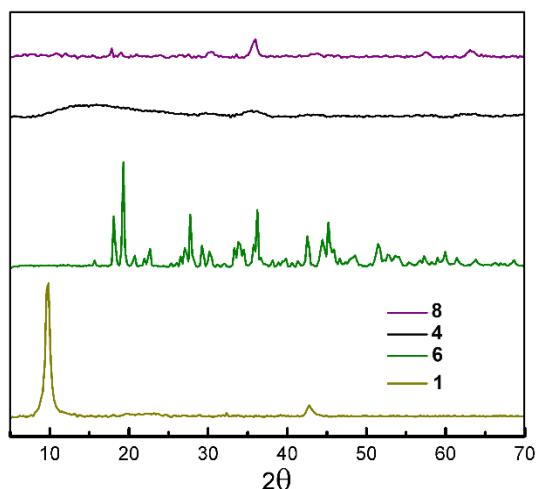


Figure 19. XRD spectrum of the Ni nanocomposite, **8** (top) compared to the spectra of the parent materials ($\text{Fe}_3\text{O}_4@\text{GO}$, **4**; $\text{Ni}_3(\text{BTC})_2$, **6**; GO, **1**).

This suggests that all three components are present in the final samples, even after several intense washes. Therefore, strong interactions among components is expected.

Morphologies of the prepared hybrid nanomaterials and their parent materials were studied by SEM, and TEM and are shown in Figures 20 and 21. The images demonstrate the successful formation of the layers during formation of the **5** and **6** results in nanoscale MOFs, which may be more suitable for small molecule adsorption. Presence of GO during the MOFs formation have several advantages such as increased dispersive forces in the MOFs, suppressed MOF aggregation, as well as formation of small pores between the GO and the MOFs.^{106,107} We

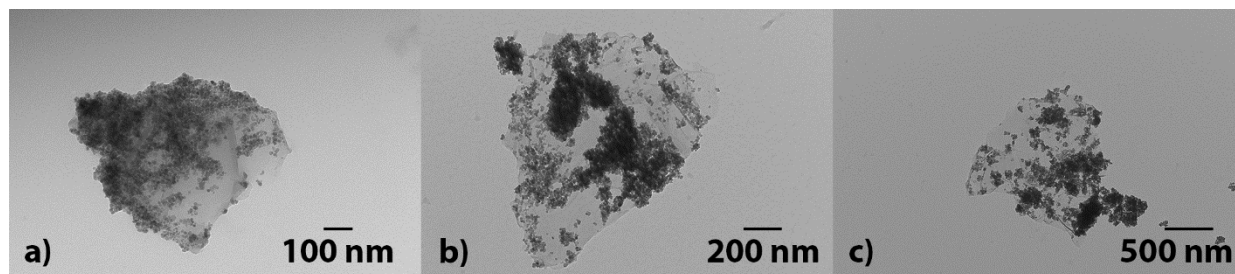


Figure 20. TEM images for GO-nanocomposites. (a) Go coated with Fe_3O_4 nanoparticles. (b) GO- $\text{Co}_3(\text{BTC})_2$ magnetic nanocomposite. (c) GO- $\text{Ni}_3(\text{BTC})_2$ magnetic nanocomposite.

believe that due to the in situ formation of the MOFs using M^{2+} salts and BTC ligand precursors, **5** and **6** are formed and grown over layers of **1** through chemical bonding between the GO functional groups and the

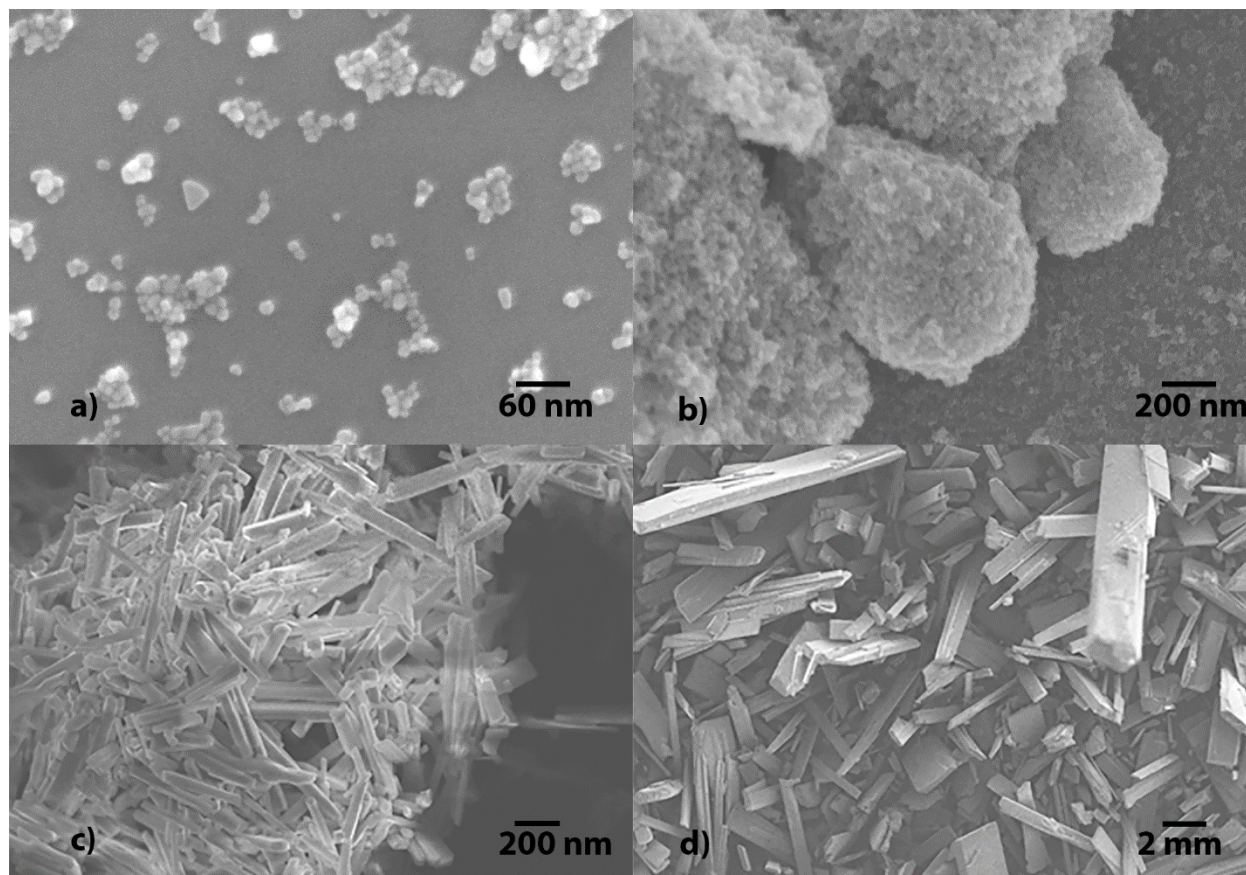


Figure 21. SEM images for parent materials. (a) $Ni_3(BTC)_2$. (b) $Co_3(BTC)_2$. (c) Fe_3O_4 Nanoparticles. (d) Fe_3O_4 nanoparticles functionalized with APTES

MOFs. Formation of the M^{2+} MOF between the GO layers also benefits the separation of the GO sheets and inhibits stacking of the layers resulting in higher surface availability for adsorption. The elemental composition of the prepared magnetic hybrid **7** and **8** nanocomposites was verified through XPS analysis. As shown in Figures 22, 23 and 24, the signals corresponding to C, O, Fe, and Ni are observed as follows: C1s at 285 eV, O1s at 531 eV, Fe2p_{3/2} at 711 and 725 eV, and Ni2p_{3/2} at 856, 861, and 873 eV. For $Fe_3O_4/GO/Co_3(BTC)_2$, the characteristic peaks of

C1s (285 eV), O1s (531 eV), Fe2p_{3/2} (711 and 725 eV), and Co2p_{3/2} (856, 861, and 873 eV) were observed corroborating synthesis of the magnetic nanocomposite.

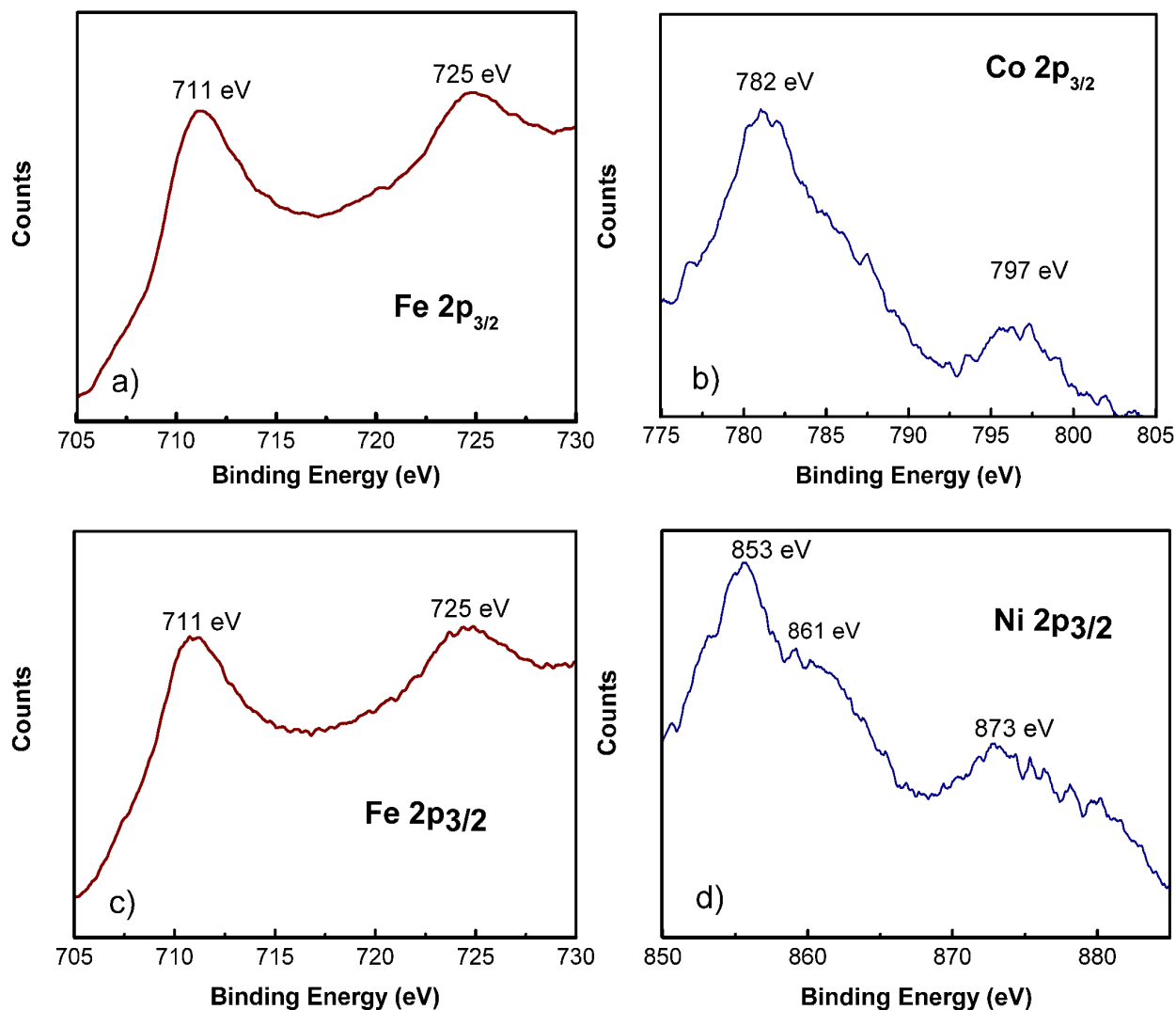


Figure 22. XPS spectra for a) Co Composite Fe2p_{3/2} with peaks at 711 and 725 eV. b) Co 2p_{3/2}. c) Ni Composite Fe 2p_{3/2} with peaks at 711 and 725 eV and d) Ni 2p_{3/2} at 853, 861 and 873 eV.

The IR spectra of **2**, **5** and **6** over **1** further verifies successful formation and decoration through the characteristic signals of GO assigned to the O-H, C=O, C=C, and C-O vibrations observable, in Figure 25, at 3166 cm⁻¹, 1716 cm⁻¹, 1617 cm⁻¹, and 1025 cm⁻¹, respectively. When the GO is functionalized with **3** a peak is visible at 540 cm⁻¹. **5** shows peaks at around 1617 and 1541 cm⁻¹

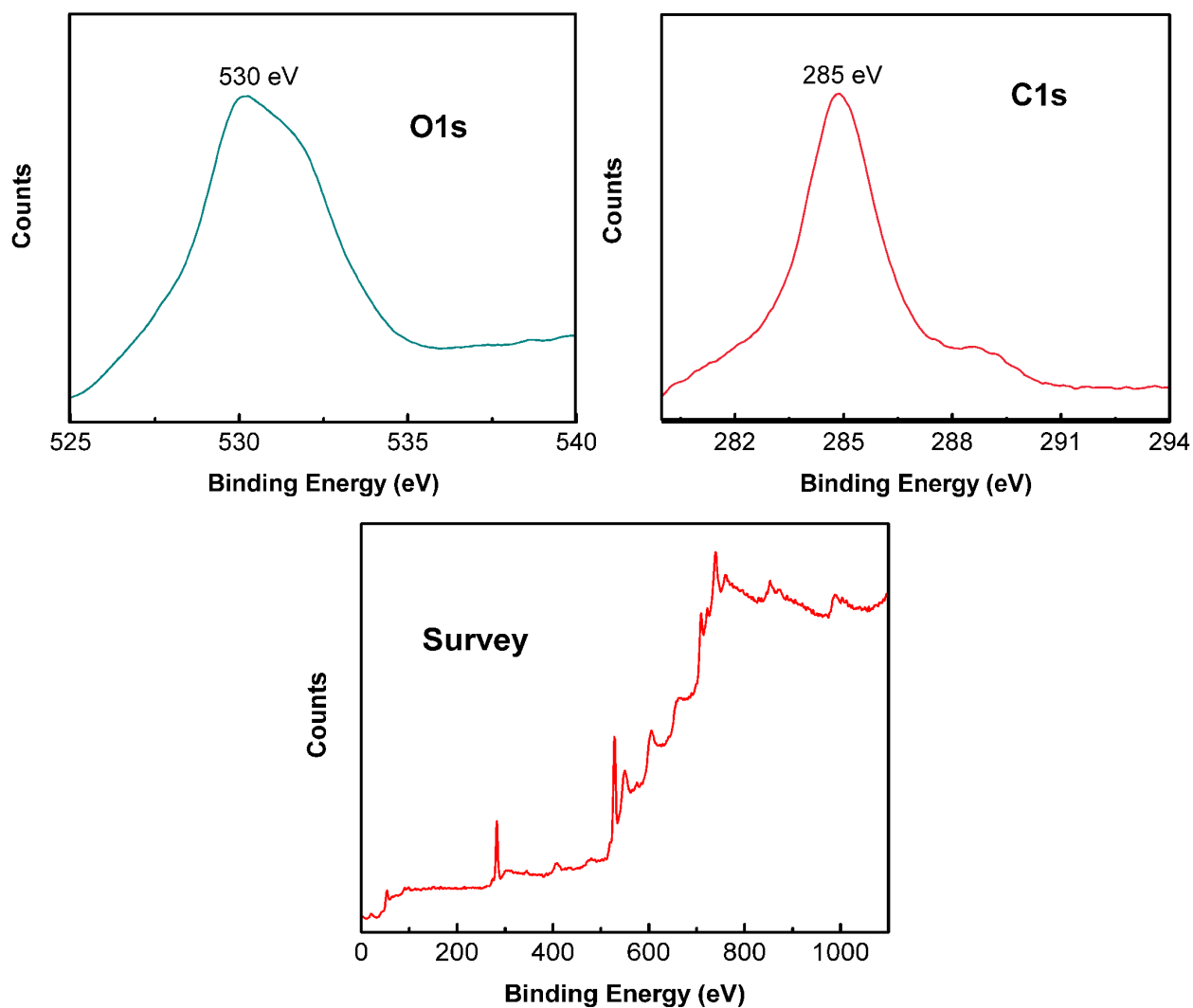


Figure 23. XPS complete spectra as well as carbon and oxygen spectra of the prepared $\text{Fe}_3\text{O}_4/\text{GO}/\text{Ni}_3(\text{BTC})_2$ (asymmetric vibrations in $-\text{CO}_2^-$); 1438 and 1358 cm^{-1} corresponding to the asymmetric and symmetric stretching vibrations of the BTC carboxylate groups. A signal at 713 cm^{-1} was assigned to the $\text{C}-\text{O}-\text{Ni}$ vibration. Presence of these peaks provides clear evidence of the successful formation of $\text{Co}_3(\text{BTC})_2$ MOF. Because **5** and **6** are isostructural, the IR spectrum of **6** shows similar features as those discussed above. The IR signals at 1617 and 1541 cm^{-1} and 1438 and 1358 cm^{-1} for **5** and **6** experience a hypsochromic shift when observed in the nanocomposites which confirm chemical bonding between the parent materials in **7** and **8**. This

hypsochromic shift is due to the interactions between BTC ligands and the functional groups of the GO platform, as well as possible distortion of the MOFs structure deriving from introduction of GO.¹⁰⁹

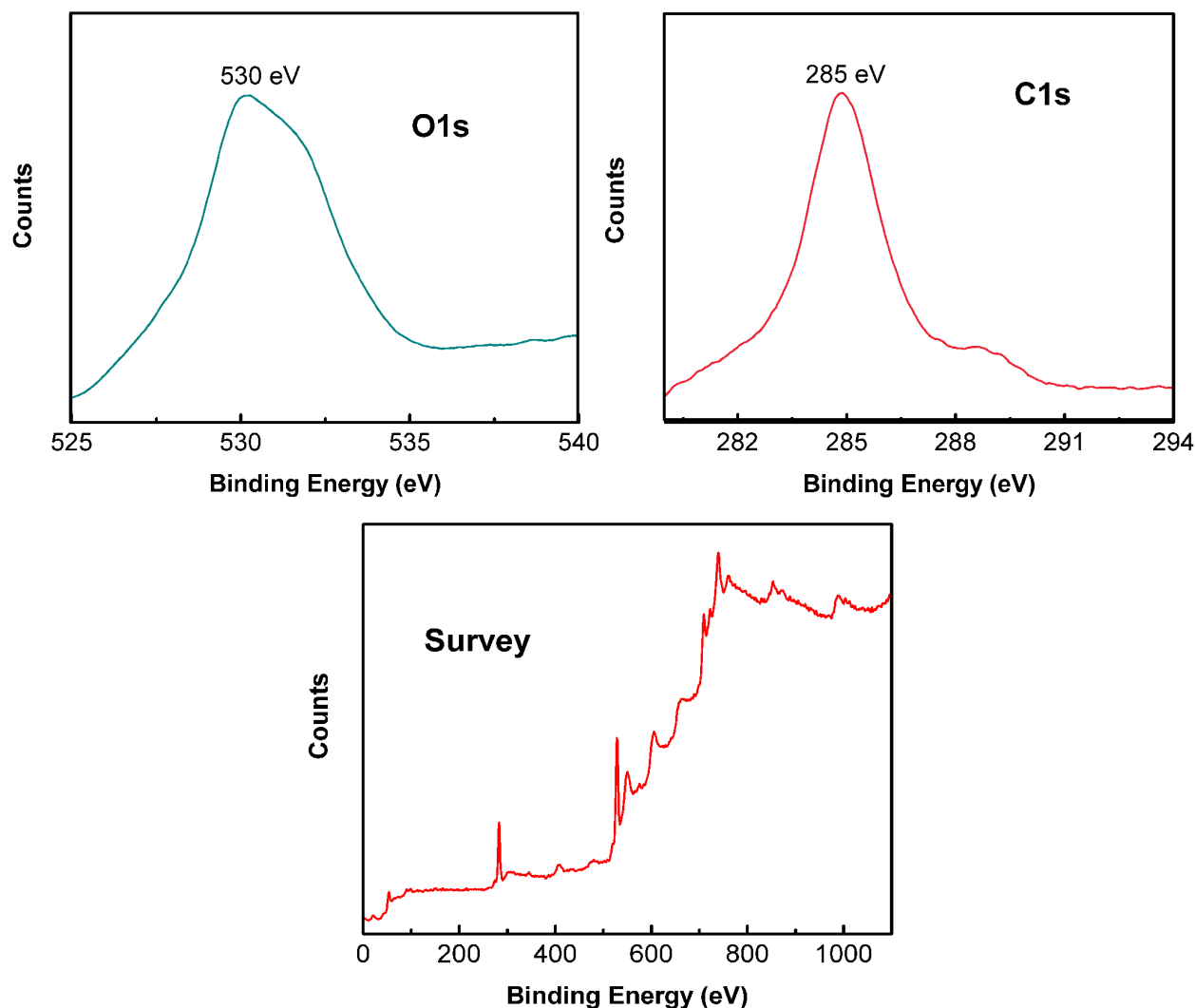


Figure 24. XPS complete spectra as well as carbon and oxygen spectra of the prepared $\text{Fe}_3\text{O}_4/\text{GO}/\text{Co}_3(\text{BTC})_2$

The synthetic manipulation of these composite materials could potentially change the superparamagnetic properties of the Fe_3O_4 nanoparticles. Thus we performed a series of magnetic measurements to test their magnetic properties as composites. The magnetization curves for all magnetic samples, 2–4, 7, and 8 are shown in Figure 26. The magnetic remanence,

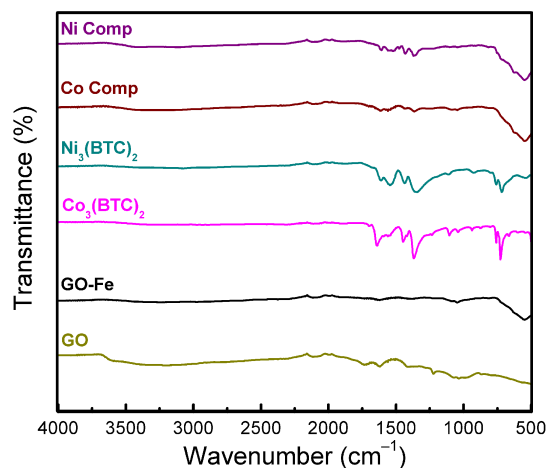


Figure 25. Infrared spectra comparison of parent materials and graphene oxide nanocomposites

coercivity, and magnetic saturation shown in Table 7 confirm that the bare magnetite nanoparticles, Fe_3O_4 , **2**, are superparamagnetic. The APTES coated Fe_3O_4 nanoparticles, **3**, show an increase of the magnetic saturation compared to the bare Fe_3O_4 nanoparticles **2** (from 45.9 emu/g to 52.9 emu/g). The APTES coating in **3** serves as a protective coating and prevents Fe_3O_4 to undergo surface oxidation. Thus, **3** maintains its magnetic integrity overtime, while **2**, lacking

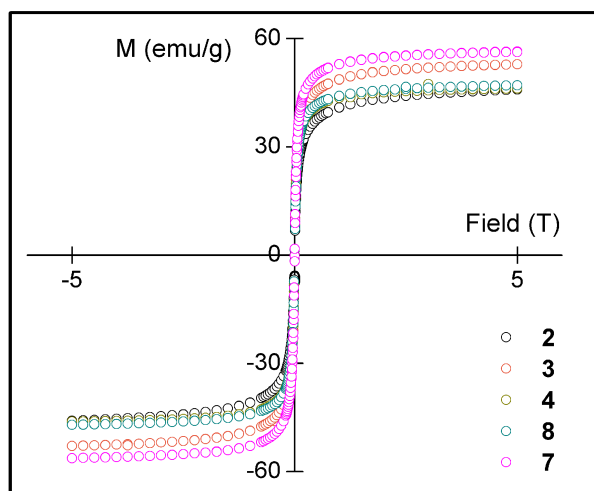


Figure 26. M vs. H curves at 300 K for: Fe_3O_4 NPs **2**, Fe_3O_4 NPs coated w/ 3-aminopropyl triethoxysilane **3**, Fe_3O_4 NPs coated w/ 3-aminopropyl triethoxysilane on GO nanosheets **4**, Ni(II) MOFs and Fe_3O_4 NPs coated w/ 3-aminopropyl triethoxysilane on GO nanosheets, **8**, the APTES coating, does not.

Graphene oxide is diamagnetic.¹²² However, loading GO with **3** yields GO/Fe₃O₄, **4**, which shows superparamagnetic properties (Table 7). The magnetic saturation of **4** is lower than that of **3** due to the increase in diamagnetism because of the presence of GO.¹²³

The superparamagnetic properties of **4** are maintained with the addition of the Ni(II) and Co(II) MOFs. The magnetic properties of **4** and **8** are very similar indicating that the addition of the Ni(II) MOFs to the GO decorated with APTES covered Fe₃O₄ MNPs has little effect on the magnetic properties. Addition of the paramagnetic Co(II) MOFs to **4**, increases the magnetic saturation from 46.2 emu/g to 56.4 emu/g, as expected.

Table 7. Summary of magnetic studies for the Ni and Co composites

Sample		Magnetism	Ms (emu/g) ^a	Hc (Oe) ^b	Mr (emu/g) ^c
Fe₃O₄	2	Superpara-	45.9	17.5	1.43
Fe-APTES	3	Superpara-	52.9	16.5	1.55
GO-Fe	4	Superpara-	46.2	16.0	1.49
Co Comp	7	Superpara-	56.4	16.0	1.73
Ni Comp	8	Superpara-	47.0	17.0	1.53
^a Ms is the magnetic saturation value ^b Hc is the coercivity value ^c Mr is the magnetic remanence value					

4.3.1. Methylene Blue Adsorption

The adsorption capacity (Q_e) of the prepared nanomaterials was calculated using Eq. 1 as follows;

$$\text{Eq. 1} \quad Q_e = \left(\frac{C_0 - C_e}{m} \right) \times V$$

where C_0 and C_e are initial and equilibrium concentration of the pollutant (mg L^{-1}), respectively, m is the adsorbent mass (g) and V is the mixture volume (L).

Table 8. Absorption capacity of parent materials and composites at different concentrations of methylene blue

Sample		Q_e (mg/g)			
		12.5 ppm	25 ppm	50 ppm	100 ppm
GO	1	23.43 ± 2.75	50.13 ± 5.16	73.41 ± 7.68	134.58 ± 19.24
GO-Fe	4	22.31 ± 0.17	35.17 ± 0.33	31.84 ± 10.2	33.05 ± 17.36
Co₃(BTC)₂	5	4.70 ± 0.62	8.75 ± 1.43	21.48 ± 2.36	37.36 ± 8.72
Ni₃(BTC)₂	6	3.51 ± 0.91	7.10 ± 1.83	11.80 ± 0.53	45.87 ± 6.78
Co Comp	7	18.52 ± 4.50	42.67 ± 4.21	67.56 ± 4.24	65.57 ± 1.64
Ni Comp	8	14.77 ± 1.72	21.12 ± 0.55	33.25 ± 3.55	54.12 ± 6.40

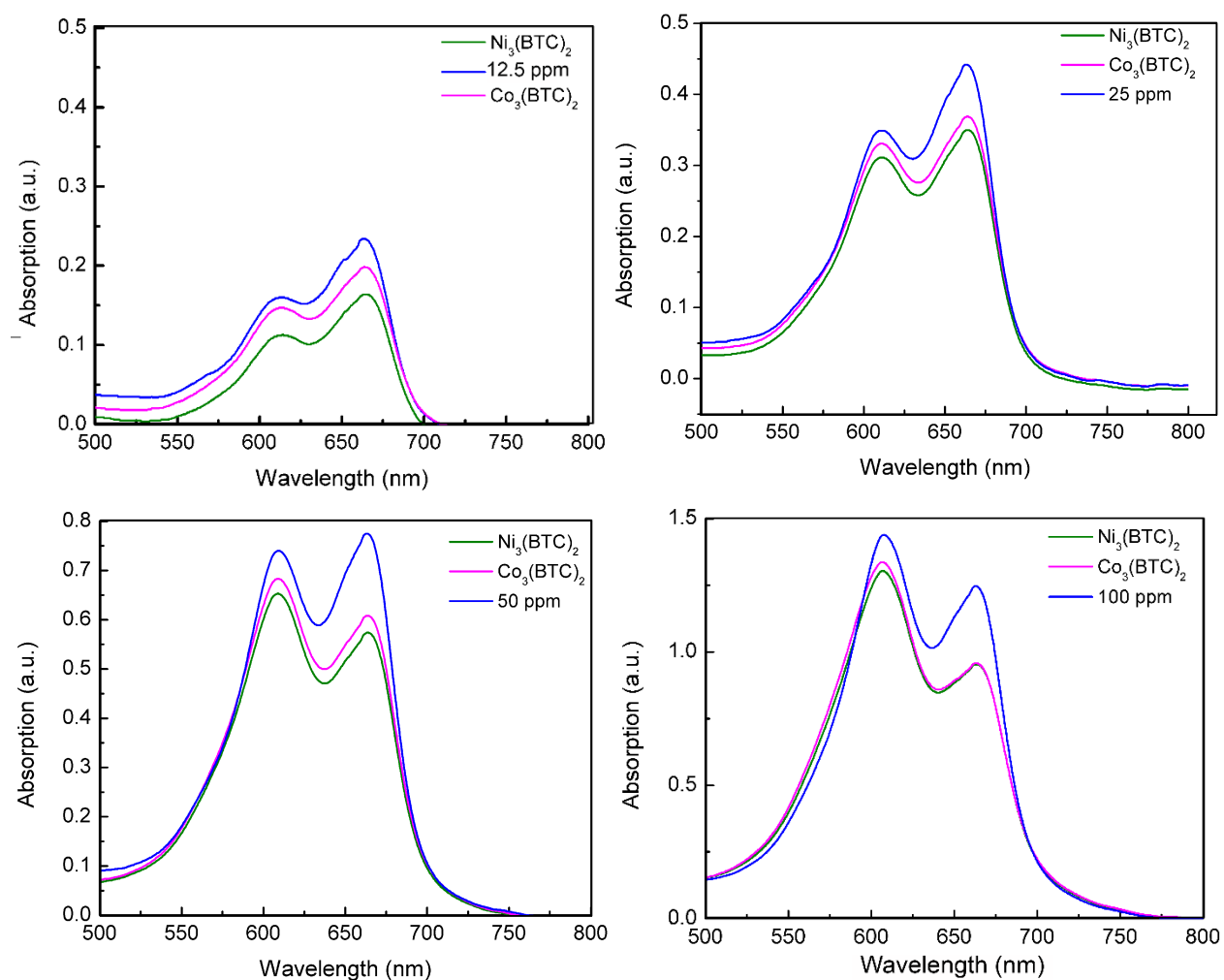


Figure 27. UV-Vis spectra of the adsorbed methylene blue dye at different concentrations using the parent materials

The pollutant adsorption capacities of the prepared hybrid nanomaterials are shown in Table 8. Nanocomposite **7** shows higher adsorbance compared to that of **8** in all concentrations. For both nanocomposites, an improvement in the adsorption capacity for methylene blue was observed compared to that of the parent materials **5** and **6**. Enhanced dye adsorption capacity of the hybrid nanomaterials compared to their MOF parent materials may be derived from synergetic effects among the individual components in a composite setting.^{94,105,106,109} It is also hypothesized that by in-situ formation and decoration of the MOFs over GO through chemical bonding, new small pores are formed between the MOFs and GO which are useful for adsorption of small molecules

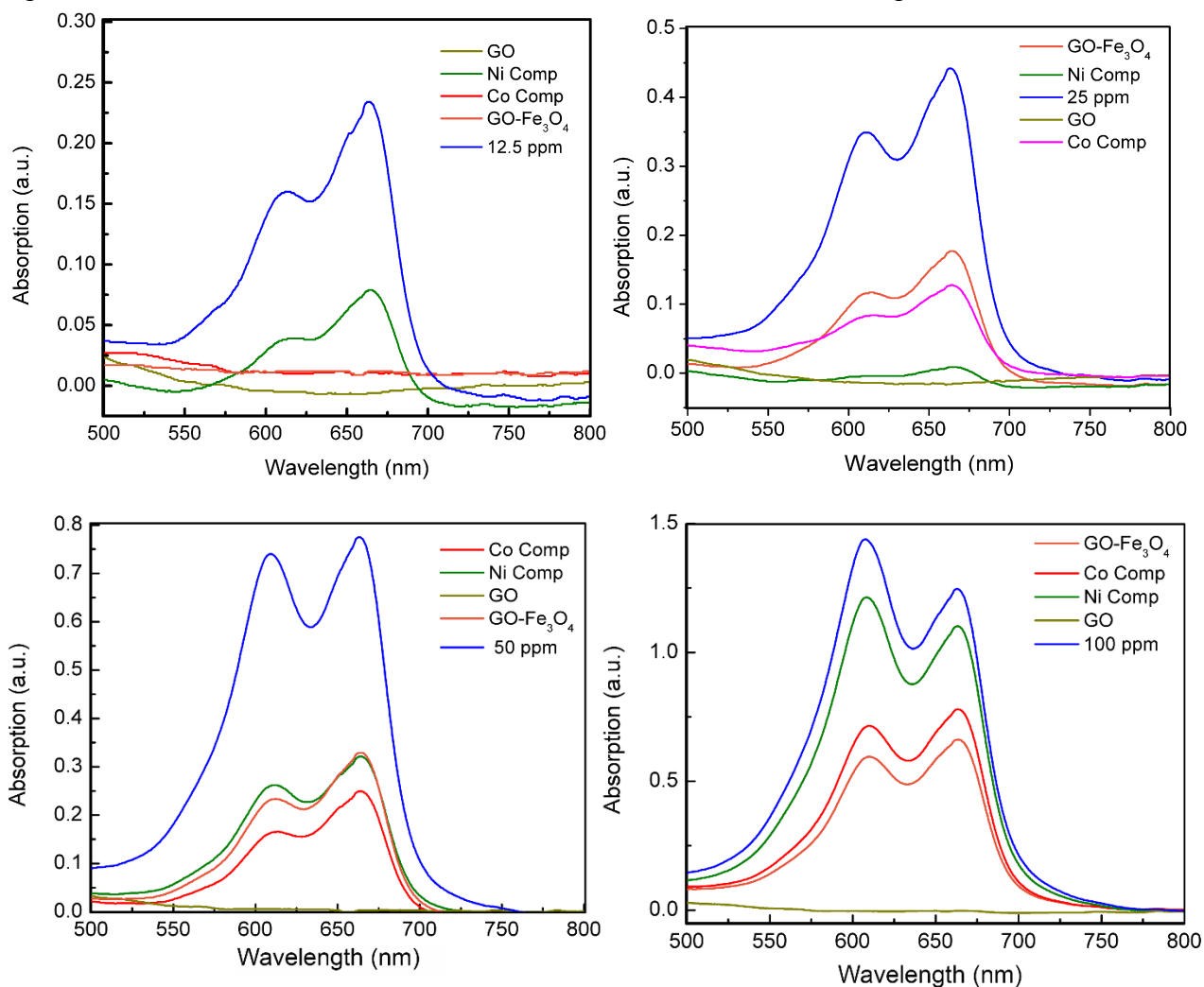


Figure 28. UV-Vis spectra of the adsorbed methylene blue dye at different concentrations using the prepared nanocomposites

and ions.^{106,107,109} Overall, it was found that the MOFs/GO composites have improved absorption capacity versus the parent MOFs but not when compared to GO.

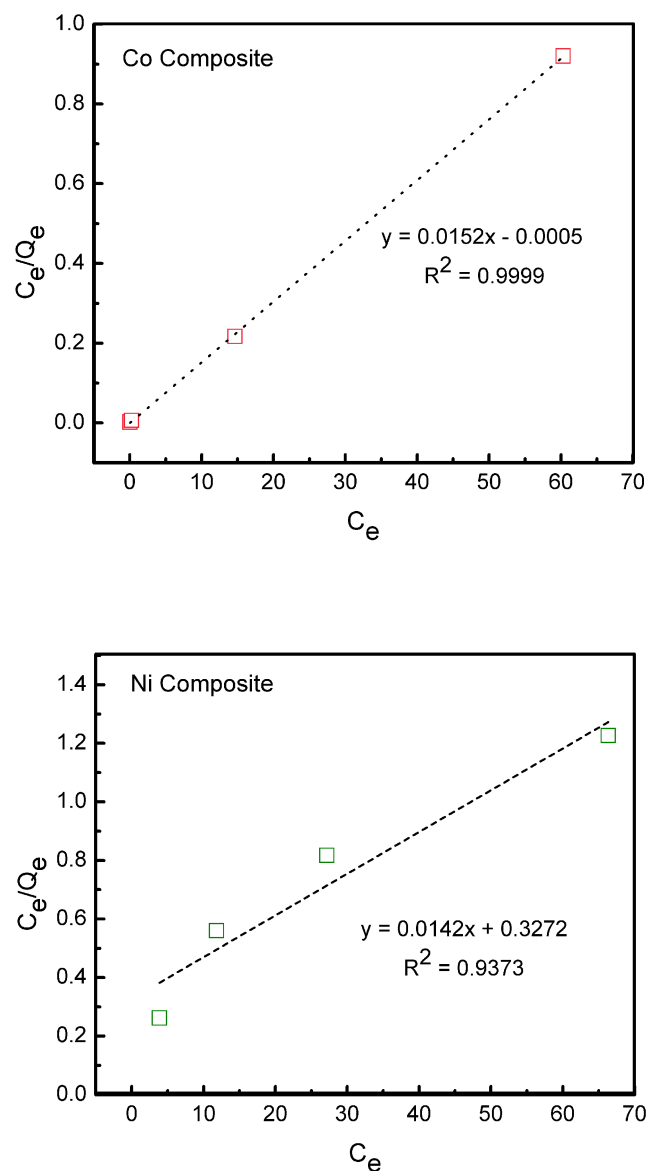


Figure 30. Langmuir isotherms (Type I) of methylene blue onto Co and Ni magnetic nanocomposites

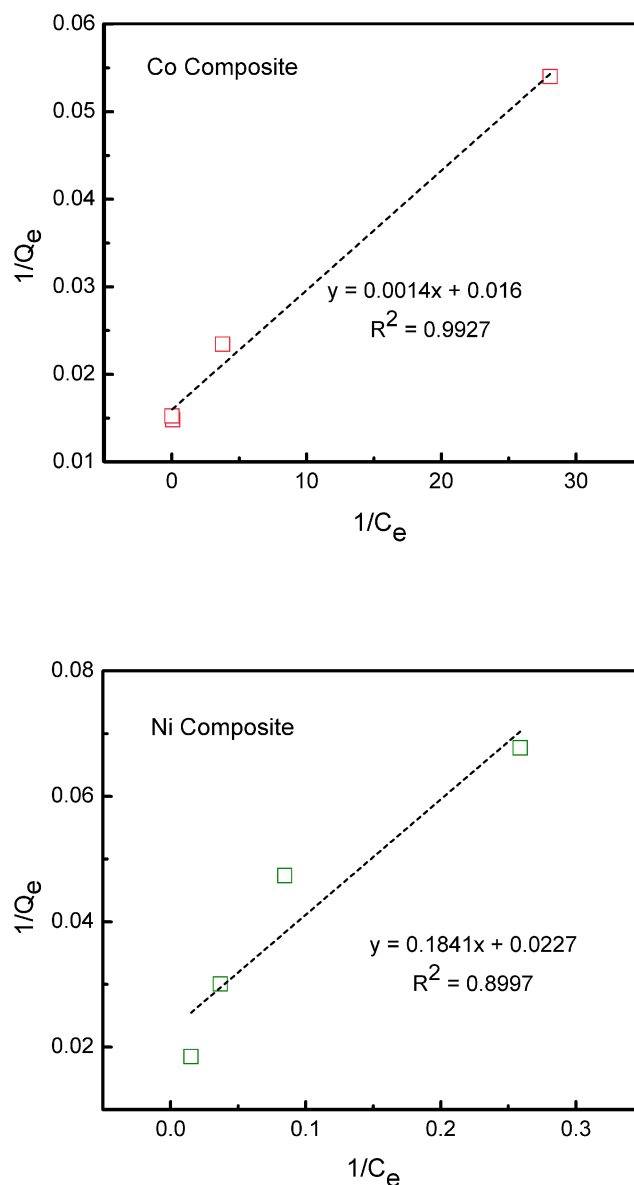


Figure 29. Langmuir isotherms (Type II) of methylene blue onto Co and Ni magnetic nanocomposites

Type I and II Langmuir isotherms plots for the adsorption of methylene blue by **7** and **8** are shown in Figures 29 and 30. These isotherms were obtained by using equation 2 and 3 as follows,

$$\text{Eq. 2} \quad \frac{C_e}{Q_e} = \left(\frac{1}{q_m} \right) C_e + \frac{1}{K_a q_m}$$

$$\text{Eq. 3} \quad \frac{1}{Q_e} = \left(\frac{1}{K_a q_m} \right) \frac{1}{C_e} + \frac{1}{q_m}$$

where q_m is the maximum absorption capacity corresponding to complete monolayer coverage on the surface and K_a is the Langmuir constant (L/mg).^{124,125}

Table 9 shows the saturation absorption capacities of methylene blue for **7** and **8**. The fitting of the data shows that methylene blue adsorption by these composites is best described by the Type I Langmuir isotherm. Thus, the maximum absorption capacities of **7** and **8** are 65.78 and 70.42 mg/g, respectively.

Table 9. Langmuir maximum absorption capacities for the Co and Ni hybrid nanocomposites.

Sample	Langmuir		
	Plot	q_m (mg/g)	R^2
7	C_e/Q_e vs C_e	65.78	0.9999
7	$1/Q_e$ vs $1/C_e$	62.50	0.9927
8	C_e/Q_e vs C_e	70.42	0.9373
8	$1/Q_e$ vs $1/C_e$	44.05	0.8997

Regeneration studies were performed on the composites and the parent materials. After the initial methylene blue adsorption test each sample was rinsed with acetone and heated to 100 °C for

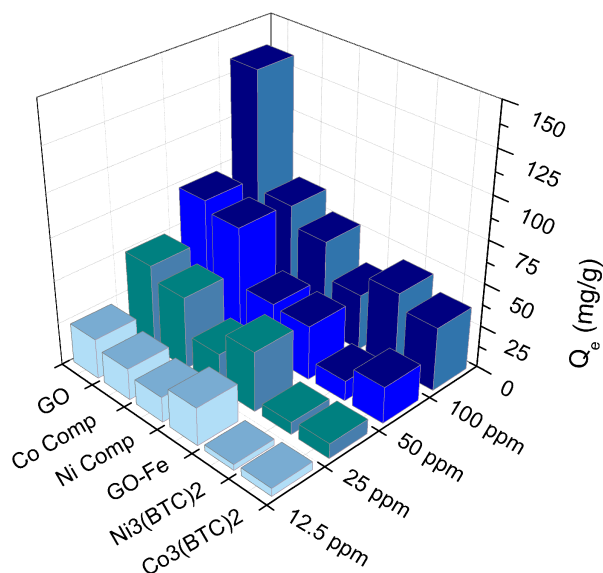


Figure 31. Absorption capacity of parent materials and composites of methylene blue at 12.5, 25, 50 and 100 ppm

12h.^{126,127} The adsorption tests were repeated following the same initial procedure using the regenerated samples. It was found that **2**, **3**, and **6** did not regenerate. However, **5** adsorbed 9% of the initial adsorbance capacity after regeneration, **1** regenerated to 46%, **8** to 14%, and **7** to 47%.

4.3.2. Brackish water treatment

The concentration of the calcium, magnesium, sulfates, and silicon analytes was measured by ICP-OES to determine adsorption capacity of **1-8**. A summary of the adsorption capacity results is shown in Table 11. The adsorption capacities of the composited ranged from less than 100 mg per gram adsorbent to 224 mg per gram adsorbent across the samples tested.

Leaching analysis show a strong stabilization of the MOFs by the combination with GO-Fe. This was shown by a much lower dissolution rate of the composite nanoparticles as compared to the naked MOFs. **1**, **2**, and **3** have very low dissolution rates in water and are stable in solution. As shown in Table 12, dissolution of nanoparticles decreased by ten-fold for **8** versus **6**, and there was almost a complete reduction of dissolution for **7**. The adsorption capacity for calcium and

magnesium ions was fairly consistent throughout the samples. Meanwhile, the absorption capacity of silicates and sulfates (SiO_3^{2-} and SO_4^{2-}) increased by almost five and seven times respectively for the prepared hybrid nanocomposites when compared to that of the graphene oxide.

Table 10. Initial Concentration of Analytes in Test Water

Constituents	Conc. (mg/L)	Conc. (mM)
Bicarbonate (HCO_3^-)	242	4
Calcium (Ca^{2+})	159	4
Chloride (Cl^-)	1,295	37
Magnesium (Mg^{2+})	63	3
Sodium (Na^+)	764	33
Silicate (SiO_3^{2-})	223	3
Sulfate (SO_4^{2-})	249	3

Table 11. Adsorption capacity for tested nanomaterials and composites per analyte.

Sample	Q_e (mg/g)				
		Ca^{2+}	Mg^{2+}	SO_4^{2-}	SiO_3^{2-}
GO	1	58.1	15.7	17.8	3.3
Fe_3O_4	2	53.8	10.5	43.2	16.5
GO-Fe	4	59.8	15.6	57.7	8.7
$\text{Co}_3(\text{BTC})_2$	5	42.9	10.6	79.4	11.0
$\text{Ni}_3(\text{BTC})_2$	6	36.0	9.8	59.9	7.3
Co Comp	7	57.5	12.7	109.9	13.2
Ni Comp	8	64.1	14.4	129.6	15.7

Table 12. Average ion concentration due to dissolution of nanomaterials in test solutions.

Sample	Average ion concentration (ppm)	
	Co	Ni
Co ₃ (BTC) ₂	5 105.2	--
Co Comp	7 0.5	--
Ni ₃ (BTC) ₂	6 --	220.0
Ni Comp	8 --	16.4

Table 13. Adsorption capacity and percent removal of ions for tested nanomaterials and composites per analyte.

		<i>Q_e (mg/g)</i>							
Sample		Ca ²⁺	% removed	Mg ²⁺	% removed	SO ₄ ²⁻	% removed	SiO ₃ ²⁻	% removed
GO	1	58.1	18.3	15.7	12.5	17.8	3.6	3.3	0.7
Fe ₃ O ₄	2	53.8	16.9	10.5	8.3	43.2	8.7	16.5	3.7
GO-Fe	4	59.8	18.8	15.6	12.4	57.7	11.6	8.7	2.0
Co ₃ (BTC) ₂	5	42.9	13.5	10.6	8.4	79.4	15.9	11.0	2.5
Ni ₃ (BTC) ₂	6	36.0	11.3	9.8	7.8	59.9	12.0	7.3	1.6
Co Comp	7	57.5	18.1	12.7	10.1	109.9	21.9	13.2	3.0
Ni Comp	8	64.1	20.2	14.4	11.4	129.6	25.9	15.7	3.5

Table 14. Adsorption capacity and percent removal of methylene blue for tested nanomaterials and composites per analyte

		<i>Q_e (mg/g)</i>							
Sample		12.5 ppm	%	25 ppm	%	50 ppm	%	100 ppm	%
GO	1	23.43 ± 2.75	93.8	50.13 ± 5.16	100	73.41 ± 7.68	73.4	134.58 ± 19.24	67.3
GO-Fe	4	22.31 ± 0.17	89.2	35.17 ± 0.33	70.3	31.84 ± 10.2	31.8	33.05 ± 17.36	16.5
Co ₃ (BTC) ₂	5	4.70 ± 0.62	18.8	8.75 ± 1.43	17.5	21.48 ± 2.36	21.5	37.36 ± 8.72	18.7
Ni ₃ (BTC) ₂	6	3.51 ± 0.91	14.04	7.10 ± 1.83	14.2	11.80 ± 0.53	11.8	45.87 ± 6.78	22.9
Co Comp	7	18.52 ± 4.50	74.1	42.67 ± 4.21	85.3	67.56 ± 4.24	67.6	65.57 ± 1.64	32.8
Ni Comp	8	14.77 ± 1.72	59.08	21.12 ± 0.55	42.2	33.25 ± 3.55	33.3	54.12 ± 6.40	27.1

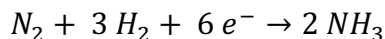
4.4. Conclusions

Two sets of efficient magnetic adsorbents, **7** and **8**, hybrid nanocomposites were synthesized by using a simple solvothermal method. The synthesized samples were characterized by XRD, SEM, TEM, XPS, and IR. The crystallinity of the samples was verified by XRD. SEM, and TEM imaging show the successful synthesis and decoration of nanoscale **5** and **6**, as well as **3** onto graphene oxide nanosheets. IR spectroscopy confirms the successful coalescing of the MOFs, Fe_3O_4 MNPs, and GO parent materials. The prepared hybrid nanocomposites were used in adsorption of MB as an organic pollutant model and in model brackish water for the adsorption of common ions. It was determined that the hybrid nanocomposites have higher methylene blue adsorption capacity, when compared to the MOFs parent materials, and the adsorption capacity for silicates and sulfates is improved by about seven times when compared to graphene oxide. The improved pollutant adsorption capacity is attributed to the synergetic effect of compositing the parent materials. The magnetic $\text{Fe}_3\text{O}_4/\text{Co}_3(\text{BTC})_2@\text{GO}$ nanocomposite, **7**, shows the highest dye adsorption capacity among the prepared materials, whereas the highest sulfate and silicate adsorption capacity was observed by the magnetic $\text{Fe}_3\text{O}_4/\text{Ni}_3(\text{BTC})_2@\text{GO}$ nanocomposite, **8**. These newly developed magnetic hybrid nanomaterials are suitable for environmental applications such as water and wastewater treatments by adsorption of pollutants.

Chapter V: Conclusion

In this dissertation, we were able to synthesize a bimetallic system with open coordination sites. This is a step closer to understand the fundamentals of small molecule activation for the development of clean and renewable energies. Future generations can learn about these fundamentals and other electrochemical processes through the developed physical chemistry laboratory practice here presented. In this practice, the basics of inner-sphere electron transfer are discussed. Similar bimetallic system can be functionalized with other materials such as, graphene oxide and magnetite to achieve water remediation. These composites have shown to be effective for the adsorption of methylene blue, silicates and sulfates.

The bimetallic system, $W_2(DippF)_2K_2$, with open coordination sites was successfully synthesized. This compound is the first example of a M_2 core with a metal center in the zero oxidation state supported by commonly known π -donating ligands. The unusual electron rich core results in the longest quadruply bonded ditungsten bond ever reported. These qualities make $W_2(DippF)_2K_2$ a suitable candidate for the study of small molecule activation. The six electron difference between $W_2(DippF)_2Cl_4$ and $W_2(DippF)_2K_2$ is fitting for the potential conversion of N_2 to NH_3 by the following reaction.



Currently our group is carrying out studies of the reactivity of the dianionic species, where small molecules as well as simple organic complexes are used (Figure 32)

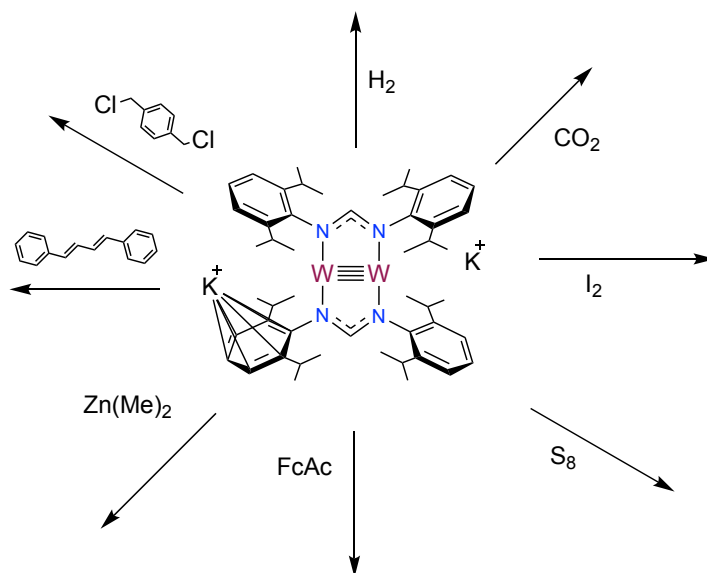


Figure 32. Digram of the current reactivity studies being carried out using $W_2(DippF)_2K_2$

Future generations of young scientists are studying the fundamentals of electron transfer. Processes that require electron transfer are commonly found in nature and in important industrial procedures. Important examples of ET mechanisms include processes inside the body. For example, the mitochondria, which is the center of cellular respiration, carries out the Krebs's Cycle, in which an electron transport chain is key for oxygen consumption. In plants, ET reactions can be found during photosynthesis when obtaining chemical energy from solar energy. The production of ammonia from inert nitrogen gas found in the atmosphere, known as the Haber-Bosch process, is widely used in industry for the production of fertilizers. A deficiency of laboratory teaching courses in literature drove our interest to develop a physical chemistry laboratory practice that has been implemented at The University of Texas at El Paso for students at the junior college level. In this laboratory exercise, the students use two ferrocene dimer isomers as platforms for the study of electron transfer in mixed valence systems. The electronic communication among the ferrocene centers was determined by calculating the equilibrium constant of the comproportionation

reaction. These complexes were sorted according to the Robin Day classification. For dimers (E) and (Z) equilibrium constants, K_c , of 4.7×10^2 and 1.1×10^3 were obtained, corresponding to Class II in the Robin-Day classification.

The use of fossil fuels resulted in adverse effects on the environment. The practice of fracking techniques for the extraction of oil and gas have caused the contamination of bodies of fresh water. The resulting contaminated water, for the most part contains a wide range of different types of contaminants from organic materials to toxic metal ions. In an effort to aid the water crisis that has resulted from the extraction of oil and gas, we have developed two sets of efficient magnetic adsorbents, capable of adsorb two different types of contaminants, using simple solvothermal methods. The resulting nanocomposites consists of three layers; (1) Graphene oxide nanolayers as supporting platforms (2) Metal-organic frameworks of the nature $M_3(BTC)_2$ (where $M = Co$ or Ni) as adsorbents and (3) iron oxide nanoparticles (magnetite) as a magnetic component. These composites were successfully synthesized, characterized and morphologically studied using XRD, SEM, TEM, XPS, and IR. In addition, the hybrid nanocomposites were used in the adsorption of methylene blue as an organic pollutant model and in model brackish water for the adsorption of common ions. The nanocomposites showed higher methylene blue adsorption capacity, when compared to the MOFs parent materials, and the adsorption capacity for silicates and sulfates was improved when compared to graphene oxide. The synergetic effect of compositing the parent materials. improved the pollutant adsorption capacity. $Fe_3O_4/Co_3(BTC)_2@GO$ shows the highest dye adsorption capacity among the prepared materials, meanwhile the highest sulfate and silicate adsorption capacity was observed by $Fe_3O_4/Ni_3(BTC)_2@GO$. These newly developed magnetic hybrid nanomaterials are suitable for environmental applications such as water and wastewater treatments by adsorption of pollutants.

References

- (1) Yilmaz, F.; Balta, M. T.; Selbaş, R. *Renew. Sustain. Energy Rev.* **2016**, *56* (Supplement C), 171.
- (2) Chu, S.; Cui, Y.; Liu, N. *Nat. Mater.* **2016**, *16* (1), nmat4834.
- (3) Thomas, M.; Partridge, T.; Harthorn, B. H.; Pidgeon, N. *Nat. Energy* **2017**, *2* (5), nenergy201754.
- (4) McConnell, I.; Li, G.; Brudvig, G. W. *Chem. Biol.* **2010**, *17* (5), 434.
- (5) Röper, M. In *Catalysis in C1 Chemistry*; Catalysis by Metal Complexes; Springer, Dordrecht, 1983; pp 41–88.
- (6) Hollander, J.; Spialter, L. *J. Chem. Educ.* **1958**, *35* (9), 446.
- (7) Hydrogen Production | Department of Energy <https://energy.gov/eere/fuelcells/hydrogen-production> (accessed Oct 30, 2017).
- (8) Nesterenko, A. I.; Berlizov, Y. S. *Chem. Technol. Fuels Oils* **2007**, *43* (6), 515.
- (9) Cotton, F. A.; Murillo, C. A.; Walton, R. A. *Multiple Bonds between Metal Atoms*; Springer Science & Business Media, 2006.
- (10) After 155 Years, A Crystalline Chromium Carboxylate with a Supershort Cr–Cr Bond - Journal of the American Chemical Society (ACS Publications) <http://pubs.acs.org/doi/abs/10.1021/ja993755i> (accessed Oct 30, 2017).
- (11) Cotton, F. A.; Daniels, L. M.; Murillo, C. A.; Slaton, J. G. *J. Am. Chem. Soc.* **2002**, *124* (12), 2878.
- (12) Cotton, F. A.; Daniels, L. M.; Murillo, C. A.; Timmons, D. J.; Wilkinson, C. C. *J. Am. Chem. Soc.* **2002**, *124* (31), 9249.
- (13) Bailey, P. J.; Bone, S. F.; Mitchell, L. A.; Parsons, S.; Taylor, K. J.; Yellowlees, L. J. *Inorg. Chem.* **1997**, *36* (5), 867.
- (14) Cotton, F. A.; Dalal, N. S.; Hillard, E. A.; Huang, P.; Murillo, C. A.; Ramsey, C. M. *Inorg. Chem.* **2003**, *42* (5), 1388.
- (15) Pap, J. S.; Snyder, J. L.; Piccoli, P. M. B.; Berry, J. F. *Inorg. Chem.* **2009**, *48* (20), 9846.
- (16) Cotton, F. A.; Gruhn, N. E.; Gu, J.; Huang, P.; Lichtenberger, D. L.; Murillo, C. A.; Van Dorn, L. O.; Wilkinson, C. C. *Science* **2002**, *298* (5600), 1971.
- (17) Sutin, N.; Creutz, C. *J. Chem. Educ.* **1983**, *60* (10), 809.
- (18) Yuan Jang, C.; Dung-Shien, P.; Chi-Fa, C.; Jia-Xin, S.; She JIng, L.; Keh Shin, K. *Inorg. Chem.* **2000**, *39* (5), 953.
- (19) WHO | Analysis of wastewater for use in agriculture http://www.who.int/water_sanitation_health/publications/labmanual/en/ (accessed Oct 30, 2017).
- (20) WHO | Benzene in drinking-water http://www.who.int/water_sanitation_health/publications/benzene/en/ (accessed Oct 30, 2017).
- (21) Shannon, M. A.; Bohn, P. W.; Elimelech, M.; Georgiadis, J. G.; Mariñas, B. J.; Mayes, A. M. *Nature* **2008**, *452* (7185), nature06599.
- (22) Maynard, A. D.; Aitken, R. J. *Nat. Nanotechnol.* **2016**, *11* (12), 998.
- (23) Beumer, K. *Nat. Nanotechnol.* **2016**, *11* (5), 398.
- (24) Surwade, S. P.; Smirnov, S. N.; Vlassioulk, I. V.; Unocic, R. R.; Veith, G. M.; Dai, S.; Mahurin, S. M. *Nat. Nanotechnol.* **2015**, *10* (5), 459.

- (25) Ultrahigh Porosity in Metal-Organic Frameworks | Science
<http://science.sciencemag.org/content/329/5990/424> (accessed Oct 30, 2017).
- (26) Li, J.-R.; Kuppler, R. J.; Zhou, H.-C. *Chem. Soc. Rev.* **2009**, 38 (5), 1477.
- (27) Long, J. R.; Yaghi, O. M. *Chem. Soc. Rev.* **2009**, 38 (5), 1213.
- (28) Cotton, F. A.; Donahue, J. P.; Lichtenberger, D. L.; Murillo, C. A.; Villagrán, D. *J. Am. Chem. Soc.* **2005**, 127 (31), 10808.
- (29) Dolinar, B. S.; Berry, J. F. *Dalton Trans.* **2014**, 43 (16), 6165.
- (30) Cayton, R. H.; Chisholm, M. H.; Huffman, J. C.; Lobkovsky, E. B. *J. Am. Chem. Soc.* **1991**, 113 (23), 8709.
- (31) Ventura, K.; Veleta, J. M.; Metta-Magaña, A.; Villagrán, D. *Inorganica Chim. Acta* **2015**, 424, 286.
- (32) Tsai, Y.-C.; Chen, H.-Z.; Chang, C.-C.; Yu, J.-S. K.; Lee, G.-H.; Wang, Y.; Kuo, T.-S. *J. Am. Chem. Soc.* **2009**, 131 (35), 12534.
- (33) Kol, M.; Schrock, R. R.; Kempe, R.; Davis, W. M. *J. Am. Chem. Soc.* **1994**, 116 (10), 4382.
- (34) Nippe, M.; Goodman, S. M.; Fry, C. G.; Berry, J. F. *J. Am. Chem. Soc.* **2011**, 133 (9), 2856.
- (35) Churchill, M. R.; Amoh, K. N.; Wasserman, H. J. *Inorg. Chem.* **1981**, 20 (5), 1609.
- (36) Sweany, R. L.; Brown, T. L. *Inorg. Chem.* **1977**, 16 (2), 415.
- (37) Brimm, E. O.; Lynch, M. A.; Sesny, W. J. *J. Am. Chem. Soc.* **1954**, 76 (14), 3831.
- (38) Bailey, P. J.; Pace, S. *Coord. Chem. Rev.* **2001**, 214 (1), 91.
- (39) Schrock, R. R.; Sturgeooff, L. G.; Sharp, P. R. *Inorg. Chem.* **1983**, 22 (20), 2801.
- (40) Krahulic, K. E.; Enright, G. D.; Parvez, M.; Roesler, R. *J. Am. Chem. Soc.* **2005**, 127 (12), 4142.
- (41) Hohenberg, P.; Kohn, W. *Phys. Rev.* **1964**, 136 (3B), B864.
- (42) Calais, J.-L. *Int. J. Quantum Chem.* **1993**, 47 (1), 101.
- (43) Becke, A. D. *Phys. Rev. A* **1988**, 38 (6), 3098.
- (44) Becke, A. D. *J. Chem. Phys.* **1993**, 98 (7), 5648.
- (45) Lee, C.; Yang, W.; Parr, R. G. *Phys. Rev. B* **1988**, 37 (2), 785.
- (46) Frisch, M. J.; Trucks, G. W.; Schlegel, H. B.; Scuseria, G. E.; Robb, M. A.; Cheeseman, J. R.; Scalmani, G.; Barone, V.; Mennucci, B.; Petersson, G. A.; Nakatsuji, H.; Caricato, M.; Li, X.; Hratchian, H. P.; Izmaylov, A. F.; Bloino, J.; Zheng, G.; Sonnenberg, J. L.; Hada, M.; Ehara, M.; Toyota, K.; Fukuda, R.; Hasegawa, J.; Ishida, M.; Nakajima, T.; Honda, Y.; Kitao, O.; Nakai, H.; Vreven, T.; Montgomery, Jr., J. A.; Peralta, J. E.; Ogliaro, F.; Bearpark, M.; Heyd, J. J.; Brothers, E.; Kudin, K. N.; Staroverov, V. N.; Kobayashi, R.; Normand, J.; Raghavachari, K.; Rendell, A.; Burant, J. C.; Iyengar, S. S.; Tomasi, J.; Cossi, M.; Rega, N.; Millam, N. J.; Klene, M.; Knox, J. E.; Cross, J. B.; Bakken, V.; Adamo, C.; Jaramillo, J.; Gomperts, R.; Stratmann, R. E.; Yazyev, O.; Austin, A. J.; Cammi, R.; Pomelli, C.; Ochterski, J. W.; Martin, R. L.; Morokuma, K.; Zakrzewski, V. G.; Voth, G. A.; Salvador, P.; Dannenberg, J. J.; Dapprich, S.; Daniels, A. D.; Farkas, O.; Foresman, J. B.; Ortiz, J. V.; Cioslowski, J.; Fox, D. J. *Gaussian 09, Revision A.1*; Gaussian, Inc.: Wallingford, CT, 2009.
- (47) While the crystal structure of **1** has not yet been obtained we can compare this W-W distance to the triple bonded W2tpg2Cl4 (where tpg is the anion of N,N',N''-triphenylguanidine) that has a W-W bond distance of 2.261(2), consistent with the stronger basicity of the guanidinate ligand.

- (48) While we have probed and spectroscopically characterized the second reduction event yielding a putative W(I)-W(I) quintuply bonded complex, the crystal structure of this has remained elusive, and it is not a matter of this communication.
- (49) Eglin, J. L.; Smith, L. T.; Staples, R. J.; Valente, E. J.; Zubkowski, J. D. *J. Organomet. Chem.* **2000**, 596 (1–2), 136.
- (50) Nguyen, T.; Sutton, A. D.; Brynda, M.; Fetting, J. C.; Long, G. J.; Power, P. P. *Science* **2005**, 310 (5749), 844.
- (51) Murillo, C. A. *Comments Inorg. Chem.* **2015**, 35 (1), 39.
- (52) Noor, A.; Kempe, R. *Inorganica Chim. Acta* **2015**, 424 (Supplement C), 75.
- (53) Landis, C. R.; Weinhold, F. *J. Am. Chem. Soc.* **2006**, 128 (22), 7335.
- (54) These excited states would be antibonding in nature with respect to the W-W bond, and thus consistent with the observed long W-W bond.
- (55) The in-phase combination of each of these ligand orbitals do not have the symmetry to interact with the metal d orbitals (b_{1u}, b_{2g}), and they are not depicted graphically except for the b_{1u} of the antibonding that is LUMO and has some interaction with metal π orbitals.
- (56) Cole, M. L.; Junk, P. C. *J. Organomet. Chem.* **2003**, 666 (1–2), 55.
- (57) In compound 2 the NCN distances are of 1.3214 and 1.3404 Å consistent with the metal-ligand interactions.
- (58) Perkins, R. I. *J. Chem. Educ.* **1985**, 62 (11), 1018.
- (59) Tanimoto, S.; Ichimura, A. *J. Chem. Educ.* **2013**, 90 (6), 778.
- (60) Gratzel, M. *Energy Resources through Photochemistry and Catalysis*; Elsevier, 2012.
- (61) Marcus, R. A. *J. Chem. Phys.* **1956**, 24 (5), 966.
- (62) Day, P.; Hush, N. S.; Clark, R. J. H. *Philos. Trans. R. Soc. Lond. Math. Phys. Eng. Sci.* **2008**, 366 (1862), 5.
- (63) Press Release: The 1983 Nobel Prize in Chemistry
https://www.nobelprize.org/nobel_prizes/chemistry/laureates/1983/press.html (accessed Oct 26, 2017).
- (64) Angaridis, P.; Berry, J. F.; Cotton, F. A.; Lei, P.; Lin, C.; Murillo, C. A.; Villagrán, D. *Inorg. Chem. Commun.* **2004**, 7 (1), 9.
- (65) Cotton, F. A.; Liu, C. Y.; Murillo, C. A.; Villagrán, D.; Wang, X. *J. Am. Chem. Soc.* **2003**, 125 (44), 13564.
- (66) Angaridis, P.; Cotton, F. A.; Murillo, C. A.; Villagrán, D.; Wang, X. *Inorg. Chem.* **2004**, 43 (26), 8290.
- (67) Cotton, F. A.; Liu, C. Y.; Murillo, C. A.; Villagrán, D.; Wang, X. *J. Am. Chem. Soc.* **2004**, 126 (45), 14822.
- (68) Cotton, F. A.; Murillo, C. A.; Villagrán, D.; Yu, R. *J. Am. Chem. Soc.* **2006**, 128 (10), 3281.
- (69) Cotton, F. A.; Donahue, J. P.; Hall, M. B.; Murillo, C. A.; Villagrán, D. *Inorg. Chem.* **2004**, 43 (22), 6954.
- (70) Arumugam, K.; Shaw, M. C.; Chandrasekaran, P.; Villagrán, D.; Gray, T. G.; Mague, J. T.; Donahue, J. P. *Inorg. Chem.* **2009**, 48 (22), 10591.
- (71) Sun, H.; Steeb, J.; Kaifer, A. E. *J. Am. Chem. Soc.* **2006**, 128 (9), 2820.
- (72) Duan, X.-F.; Zeng, J.; Lü, J.-W.; Zhang, Z.-B. *J. Org. Chem.* **2006**, 71 (26), 9873.

- (73) According to the Robin-Day classification complexes with $K_c < 102$ are Class I. Complexes where $102 < K_c < 106$ are considered Class II. Class III complexes are those where $K_c > 106$.
- (74) Wiley: Molecular Metal-Metal Bonds: Compounds, Synthesis, Properties - Stephen T. Liddle <http://www.wiley.com/WileyCDA/WileyTitle/productCd-3527335412.html> (accessed Oct 26, 2017).
- (75) Lu, Y.; Lent, C. S. *Chem. Phys. Lett.* **2015**, *633*, 52.
- (76) Demadis, K. D.; Hartshorn, C. M.; Meyer, T. J. *Chem. Rev.* **2001**, *101* (9), 2655.
- (77) Férey, G. *Chem. Soc. Rev.* **2007**, *37* (1), 191.
- (78) Kitagawa, S.; Kitaura, R.; Noro, S. *Angew. Chem. Int. Ed.* **2004**, *43* (18), 2334.
- (79) Yaghi, O. M.; O'Keeffe, M.; Ockwig, N. W.; Chae, H. K.; Eddaoudi, M.; Kim, J. *Nature* **2003**, *423* (6941), 705.
- (80) Czaja, A. U.; Trukhan, N.; Müller, U. *Chem. Soc. Rev.* **2009**, *38* (5), 1284.
- (81) Metal-Organic Frameworks: A Rapidly Growing Class of Versatile Nanoporous Materials - Meek - 2010 - Advanced Materials - Wiley Online Library <http://onlinelibrary.wiley.com/doi/10.1002/adma.201002854/full> (accessed Oct 27, 2017).
- (82) Wu, H.; Gong, Q.; Olson, D. H.; Li, J. *Chem. Rev.* **2012**, *112* (2), 836.
- (83) Liang, D.-D.; Liu, S.-X.; Ma, F.-J.; Wei, F.; Chen, Y.-G. *Adv. Synth. Catal.* **2011**, *353* (5), 733.
- (84) Applications of advanced hybrid organic–inorganic nanomaterials: from laboratory to market - Chemical Society Reviews (RSC Publishing) <http://pubs.rsc.org/en/content/articlelanding/2011/cs/c0cs00136h#!divAbstract> (accessed Oct 27, 2017).
- (85) Shah, M.; McCarthy, M. C.; Sachdeva, S.; Lee, A. K.; Jeong, H.-K. *Ind. Eng. Chem. Res.* **2012**, *51* (5), 2179.
- (86) Haque, E.; Lee, J. E.; Jang, I. T.; Hwang, Y. K.; Chang, J.-S.; Jegal, J.; Jhung, S. H. *J. Hazard. Mater.* **2010**, *181* (1), 535.
- (87) Haque, E.; Jun, J. W.; Jhung, S. H. *J. Hazard. Mater.* **2011**, *185* (1), 507.
- (88) Zhang, C.-F.; Qiu, L.-G.; Ke, F.; Zhu, Y.-J.; Yuan, Y.-P.; Xu, G.-S.; Jiang, X. *J. Mater. Chem. A* **2013**, *1* (45), 14329.
- (89) Nickerl, G.; Leistner, M.; Helten, S.; Bon, V.; Senkovska, I.; Kaskel, S. *Inorg. Chem. Front.* **2014**, *1* (4), 325.
- (90) Hwang, Y. K.; Hong, D.-Y.; Chang, J.-S.; Jhung, S. H.; Seo, Y.-K.; Kim, J.; Vimont, A.; Daturi, M.; Serre, C.; Férey, G. *Angew. Chem. Int. Ed.* **2008**, *47* (22), 4144.
- (91) Eddaoudi, M.; Kim, J.; Rosi, N.; Vodak, D.; Wachter, J.; O'Keeffe, M.; Yaghi, O. M. *Science* **2002**, *295* (5554), 469.
- (92) Thornton, A. W.; Nairn, K. M.; Hill, J. M.; Hill, A. J.; Hill, M. R. *J. Am. Chem. Soc.* **2009**, *131* (30), 10662.
- (93) Yang, S. J.; Choi, J. Y.; Chae, H. K.; Cho, J. H.; Nahm, K. S.; Park, C. R. *Chem. Mater.* **2009**, *21* (9), 1893.
- (94) Petit, C.; Bandoz, T. J. *Adv. Mater.* **2009**, *21* (46), 4753.
- (95) Kim, M.; Cahill, J. F.; Fei, H.; Prather, K. A.; Cohen, S. M. *J. Am. Chem. Soc.* **2012**, *134* (43), 18082.
- (96) Stock, N.; Biswas, S. *Chem. Rev.* **2012**, *112* (2), 933.
- (97) O'Neill, L. D.; Zhang, H.; Bradshaw, D. J. *Mater. Chem.* **2010**, *20* (27), 5720.

- (98) Ostermann, R.; Cravillon, J.; Weidmann, C.; Wiebecke, M.; M. Smarsly, B. *Chem. Commun.* **2011**, 47 (1), 442.
- (99) Wee, L. H.; Bajpe, S. R.; Janssens, N.; Hermans, I.; Houthoofd, K.; Kirschhock, C. E. A.; Martens, J. A. *Chem. Commun.* **2009**, 46 (43), 8186.
- (100) Jahan, M.; Bao, Q.; Yang, J.-X.; Loh, K. P. *J. Am. Chem. Soc.* **2010**, 132 (41), 14487.
- (101) Petit, C.; Bandosz, T. J. *Adv. Funct. Mater.* **2010**, 20 (1), 111.
- (102) Petit, C.; Huang, L.; Jagiello, J.; Kenvin, J.; Gubbins, K. E.; Bandosz, T. J. *Langmuir* **2011**, 27 (21), 13043.
- (103) Mustafa, D.; Breynaert, E.; Bajpe, S. R.; Martens, J. A.; Kirschhock, C. E. A. *Chem. Commun.* **2011**, 47 (28), 8037.
- (104) Petit, C.; Bandosz, T. J. *Adv. Funct. Mater.* **2011**, 21 (11), 2108.
- (105) Petit, C.; Mendoza, B.; Bandosz, T. J. *Chemphyschem Eur. J. Chem. Phys. Phys. Chem.* **2010**, 11 (17), 3678.
- (106) Petit, C.; Levasseur, B.; Mendoza, B.; Bandosz, T. J. *Microporous Mesoporous Mater.* **2012**, 154 (Supplement C), 107.
- (107) Huang, Z.-H.; Liu, G.; Kang, F. *ACS Appl. Mater. Interfaces* **2012**, 4 (9), 4942.
- (108) Xiang, Z.; Peng, X.; Cheng, X.; Li, X.; Cao, D. *J. Phys. Chem. C* **2011**, 115 (40), 19864.
- (109) Petit, C.; J. Bandosz, T. *Dalton Trans.* **2012**, 41 (14), 4027.
- (110) Zhao, X.; Liu, S.; Tang, Z.; Niu, H.; Cai, Y.; Meng, W.; Wu, F.; Giesy, J. P. *Sci. Rep.* **2015**, 5.
- (111) Zhao, X.; Wang, J.; Wu, F.; Wang, T.; Cai, Y.; Shi, Y.; Jiang, G. *J. Hazard. Mater.* **2010**, 173 (1), 102.
- (112) Dave, P. N.; Chopda, L. V. Application of Iron Oxide Nanomaterials for the Removal of Heavy Metals <https://www.hindawi.com/journals/jnt/2014/398569/> (accessed Oct 27, 2017).
- (113) Jabbari, V.; Veleta, J. M.; Zarei-Chaleshtori, M.; Gardea-Torresdey, J.; Villagrán, D. *Chem. Eng. J.* **2016**, 304, 774.
- (114) Gao, J.; Qin, Y.; Zhou, T.; Cao, D.; Xu, P.; Hochstetter, D.; Wang, Y. *J. Zhejiang Univ. Sci. B* **2013**, 14 (7), 650.
- (115) Ozer, A.; Dursun, G. *J. Hazard. Mater.* **2007**, 146 (1–2), 262.
- (116) Rafatullah, M.; Sulaiman, O.; Hashim, R.; Ahmad, A. *J. Hazard. Mater.* **2010**, 177 (1–3), 70.
- (117) Kassaei, M. Z.; Masrouri, H.; Movahedi, F. *Appl. Catal. Gen.* **2011**, 395 (1), 28.
- (118) Marcano, D. C.; Kosynkin, D. V.; Berlin, J. M.; Sinitskii, A.; Sun, Z.; Slesarev, A.; Alemany, L. B.; Lu, W.; Tour, J. M. *ACS Nano* **2010**, 4 (8), 4806.
- (119) Huang, Y.; Wang, Y.; Wang, Y.; Pan, Q.; Ding, X.; Xu, K.; Li, N.; Wen, Q. *RSC Adv.* **2016**, 6 (7), 5718.
- (120) Simple preparation of crystal Co₃(BTC)₂·12H₂O and its catalytic activity in CO oxidation reaction | SpringerLink <https://link.springer.com/article/10.1007/s11595-015-1103-z> (accessed Oct 27, 2017).
- (121) Yaghi, O. M.; Li, H.; Groy, T. L. *J. Am. Chem. Soc.* **1996**, 118 (38), 9096.
- (122) Tang, T.; Liu, F.; Liu, Y.; Li, X.; Xu, Q.; Feng, Q.; Tang, N.; Du, Y. *Appl. Phys. Lett.* **2014**, 104 (12), 123104.
- (123) Veligatla, M.; Katakam, S.; Das, S.; Dahotre, N.; Gopalan, R.; Prabhu, D.; Babu, D. A.; Choi-Yim, H.; Mukherjee, S. *Metall. Mater. Trans. A* **2015**, 46 (3), 1019.
- (124) Itodo, A. U.; Itodo, H. U.; Gafar, M. K. *J. Appl. Sci. Environ. Manag.* **2010**, 14 (4).

- (125) Hameed, B. H.; Ahmad, A. A.; Aziz, N. *Chem. Eng. J.* **2007**, *133* (1), 195.
- (126) Daneshvar, E.; Vazirzadeh, A.; Niazi, A.; Kousha, M.; Naushad, M.; Bhatnagar, A. *J. Clean. Prod.* **2017**, *152*, 443.
- (127) He, X.; Male, K. B.; Nesterenko, P. N.; Brabazon, D.; Paull, B.; Luong, J. H. T. *ACS Appl. Mater. Interfaces* **2013**, *5* (17), 8796.
- (128) Perkins, R. I. *J. Chem. Educ.* **1985**, *62* (11), 1018.
- (129) Berg, J.; Tymoczko, J.; Stryer, L. *Biochemistry*, 5th ed.; W H Freeman: New York, 2002.
- (130) Sutin, N.; Creutz, C. *J. Chem. Educ.* **1983**, *60* (10), 809.
- (131) Osteryoung, J. *J. Chem. Educ.* **1983**, *60* (4), 296.

Appendix

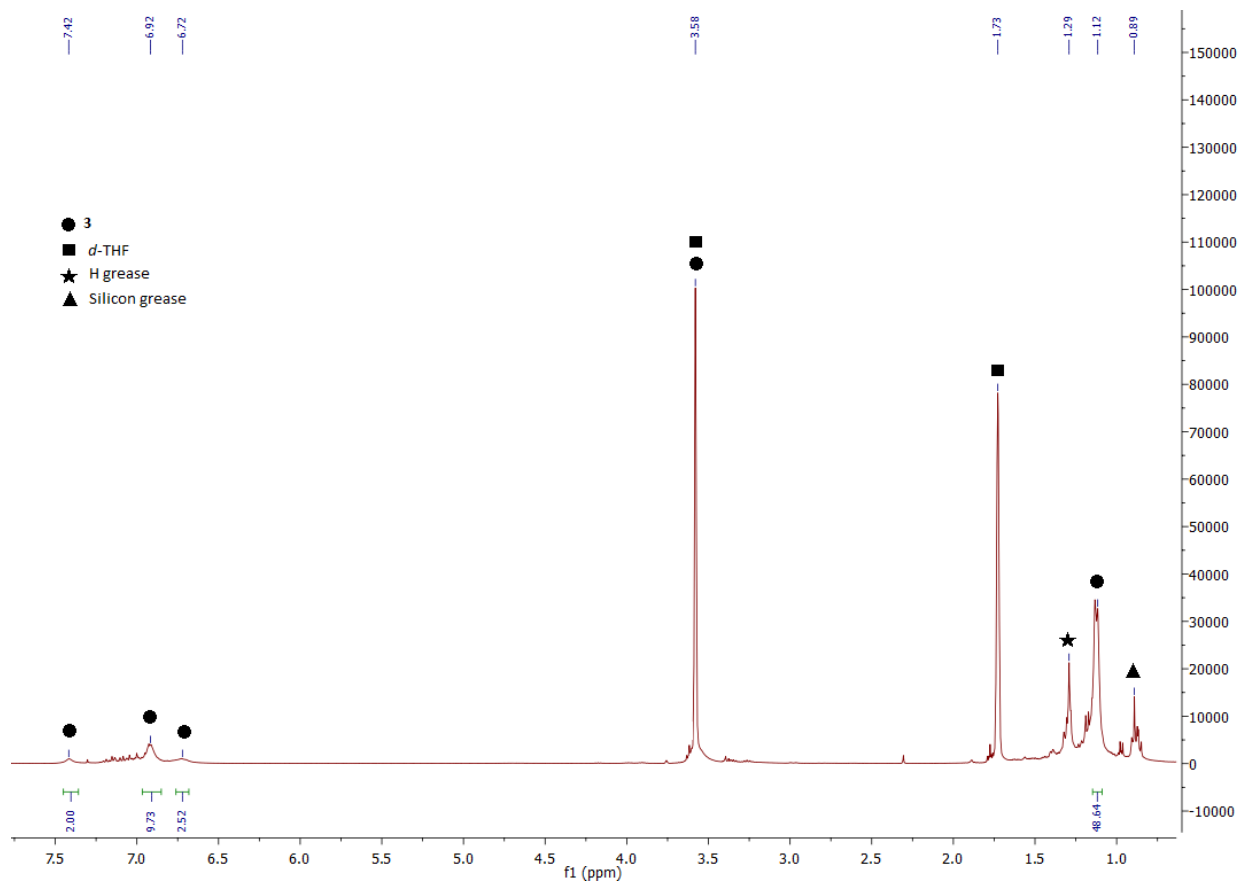


Figure 33. NMR spectrum of $W_2(DippF)_2Cl_4$ in *d*-THF

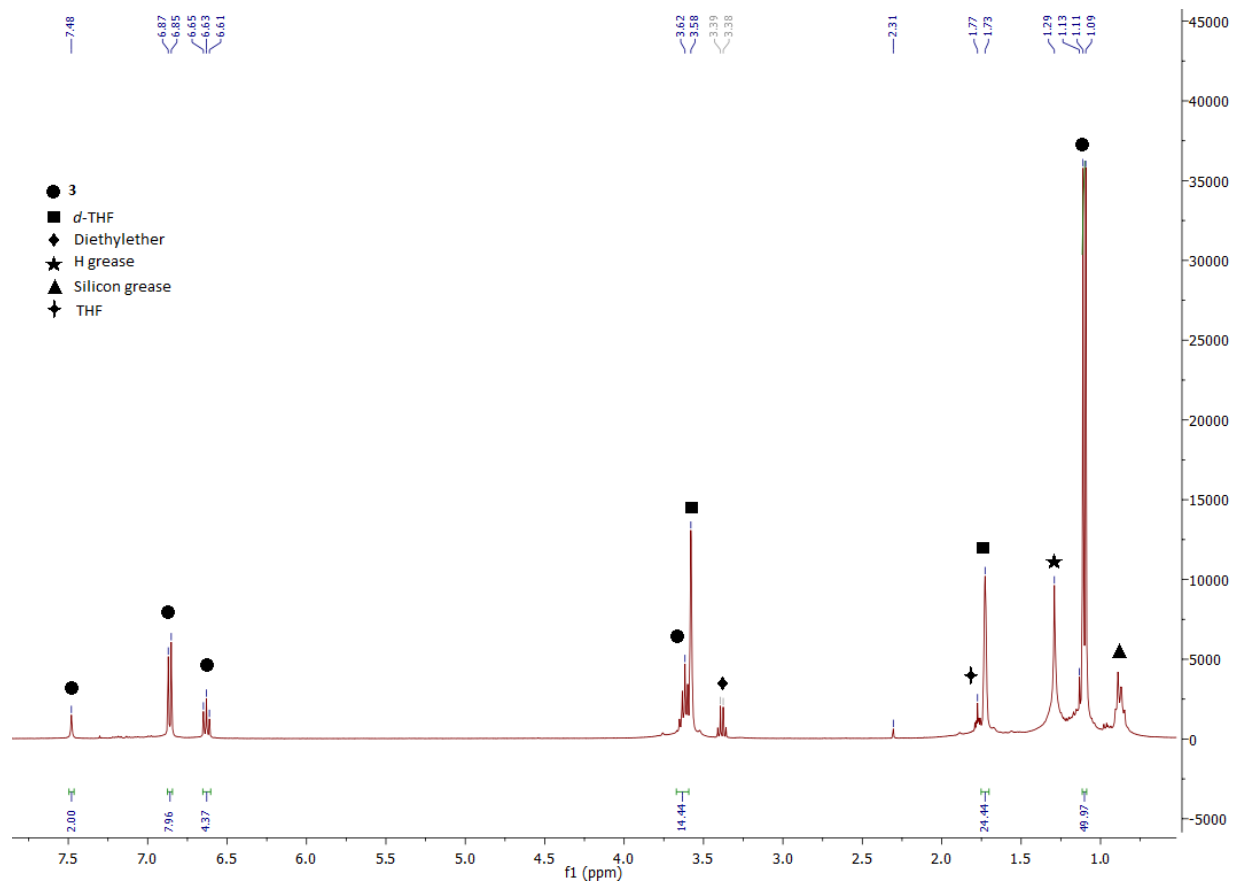


Figure 34. NMR spectrum of $W_2(DippF)_2K_2$

Student Handout

Inner Sphere Electron Transfer in Diferrocene Mixed-Valence Systems

Introduction

Electron Transfer (ET) reactions are fundamentally important in chemistry. Typically in these reactions, no bond cleavage or formation takes place during the development of products from reactants. This unpretentious act of transferring an electron from one molecule to another is a crucial process found in nature, and it is also critical to many current industrial chemical processes.¹²⁸ An excellent example of an everyday ET reaction can be found inside the human body. Mitochondria, the center of cellular respiration, carries out the Krebs's Cycle, in which an electron transport chain is key for oxygen consumption. In plants, ET reactions can be found during photosynthesis when obtaining chemical energy from solar energy.¹²⁹ The production of ammonia from inert nitrogen gas found in the atmosphere, known as the Haber-Bosch process, is widely used in industry for the production of fertilizers.

In order to fully understand all of these processes we first need to understand the fundamentals. The objective of this experiment is to explore the transfer of electrons in mixed-valent (MV) compounds utilizing electrochemical methods. Two covalently bonded ferrocene dimer molecules will be used as models for these studies.

Electron Transfer

In chemistry, the process of **oxidation** refers to the loss of electrons, while the process of **reduction** involves the gain of electrons. These two processes cannot occur separately, since the electron has to reside either in the products or the reactants. In order for electron transfer to take place, an oxidation center (electron donor) and a reduction center (electron acceptor) are needed. These processes are commonly known as oxidation-reduction reactions or redox events.

There are two types of electron transfer: inner sphere and outer-sphere. In **outer-sphere** electron transfer, the center of reduction and the center of oxidation are not bonded to each other, meaning that the electron transfer occurs through the space between the two centers. This type of ET is the most common for redox reactions in a typical synthetic laboratory. In **inner-sphere** electron transfer, the redox centers are covalently bonded to a linker and the electron is passed through that bond. However, in some instances the bond can be transient and the transfer can occur in the intermediate species. Thanks to the discovery of the mechanism of inner-sphere ET, Henry Taube was awarded the Nobel Prize in chemistry in 1983.¹³⁰

Mixed-Valence Compounds

A Mixed-Valent compound is a molecule containing oxidation and reduction centers consisting of atoms of the same element that co-exist in different oxidation states (Figure 1). Mixed-Valent compounds serve as suitable models for the study of the inner-sphere ET mechanisms by using electrochemical and spectroscopic techniques.

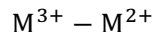


Figure 1. A mixed valent compound with two metal atoms in different oxidation states.

Most mixed-valent compounds are composed of two metallic (M) redox centers bridged by a linker molecule (L). A simplified example of this system is shown in figure 2.

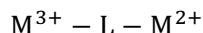
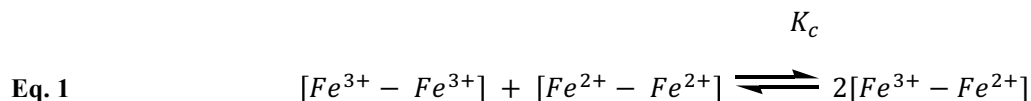


Figure 2. A mixed valent compound with two metal atoms in different oxidation states bridged by a linker molecule.

In this laboratory practice we will be studying the electron transfer in mixed-valent complexes in which the electron donor and acceptor moieties are ferrocene centers. We will use cyclic voltammetry in order to measure the thermodynamic equilibrium of the comproportionation reaction (K_c) depicted in equation 1.



The degree of electron transfer in the mixed-valent complex can be inferred by measuring K_c . A large equilibrium constant means that the concentration of the products will be favored. In contrast, a small value for K_c means that the equilibrium lies to the left (reactants).

The first compound analyzed in this experiment, to be used as reference, is ferrocene. Ferrocene is composed of a single iron ion sandwiched between two cyclopentadienyl ligands (Figure 3a). To measure

electron transfer in a mixed-valent compound, two ferrocene dimers will be used. These diastereoisomers, E-dimethylferrocenylethylene and Z-dimethylferrocenylethylene (Figures 3b and 3c respectively), consist of two ferrocene centers linked by an alkene in an E and Z conformation.

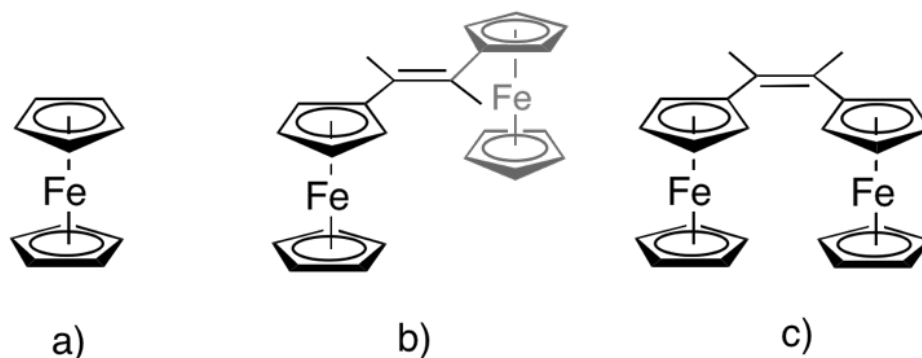


Figure 3. Drawing of the molecules used in this practice; a) Ferrocene in staggered conformation, b) E-dimethylferrocenylethylene, c) Z-dimethylferrocenylethylene.

Electrochemistry

The electrochemical methods used in this practice are cyclic voltammetry (CV) and differential pulse voltammetry (DPV). In cyclic voltammetry, a potential that increases linearly as a function of time is applied to the molecule. In differential pulse voltammetry a potential is pulsed (as opposed to being scanned) for a specific time window. DPV is typically more sensitive than CV, but CV can give useful information more quickly. The applied potential occurs at the working electrode, which may be a cathode or an anode depending on the direction of a scan. When performing an electrochemical reduction, the potential is scanned towards more negative values (or in the cathodic direction) relative to the “open circuit potential”. The open circuit potential is the potential difference between the anode and the cathode in the absence of external voltage applied. If an electron is removed from the electrode and given to the molecule, a current in the cathodic direction is observed in the cyclic voltammogram. This peak describes a reduction event of the sample. The shape of the wave (i.e. first increasing, then reaching a plateau, and finally decreasing in current) is due to the charging of the electrode surface with the sample substrate followed by reaching a diffusion limit, and then depletion of the substrate near the electrode.

When the same process is performed in the reverse direction, that is, when the potential is scanned toward positive values, an electron may be removed from the molecule towards the anode, resulting in the sample getting oxidized. This oxidation event creates a current that is shown as a peak in the anodic direction. An example of a CV is shown in Figure 4.

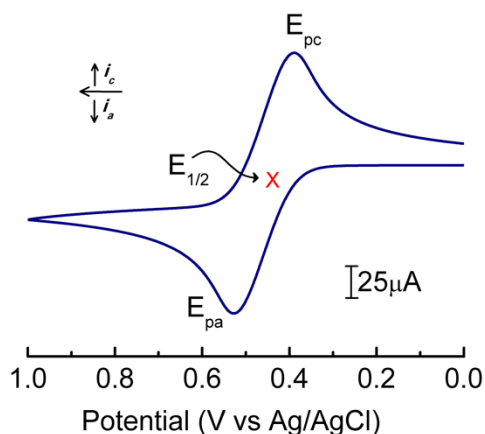


Figure 4. Example of a cyclic voltammogram with one redox event.

The peak reduction potential is labeled E_{pc} (for peak-cathodic) and the peak oxidation potential is labeled E_{pa} (for peak-anodic). The average between the peak reduction potential and the peak oxidation potential gives the half-wave potential, $E_{1/2}$, which is the redox potential of the electrochemical event, and can be calculated using Equation 2.

Eq. 2

$$E_{1/2} = \frac{E_{pc} + E_{pa}}{2}$$

With cyclic voltammetry, the relative degree of electronic communication between redox centers in a molecule (electron transfer rate) can be analyzed. To compare the electronic communication abilities of two redox centers, two redox events corresponding to the first and second electron transfers, need to be observed in the cyclovoltammogram. An example of a CV with two redox events is shown in Figure 5. A molecule capable of electron transfer exhibiting strong electronic communication is one that has a CV where the two different redox events are well defined or separated by a good distance. A molecule with weak electron transfer (poor electronic communication) is one where the two redox events are not well defined on the CV, or they are very close to each other. This is a way to qualitatively evaluate electron transfer and electronic communication.

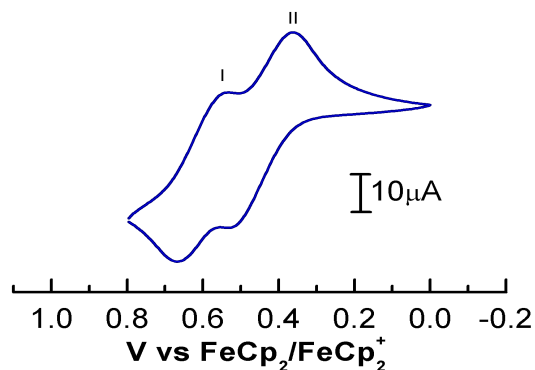


Figure 5. Example of a cyclic voltammogram with two redox events.

To find the half-wave potential in the cyclovoltammogram, one must find the half-wave potential of the first (I) and the second (II) redox event using equation 2. Then, one should use Equation 3 to find the difference between the half-wave potentials of both redox events.

Eq. 3

$$\Delta E_{1/2} = E_{1/2}^{\text{II}} - E_{1/2}^{\text{I}}$$

In differential pulse voltammetry the potential is held at a value and then stepped instantaneously to a second value. Sometime after the pulse is applied the current is then measured and as a function of potential¹³¹. An example of a DPV with two events is shown in Figure 6.

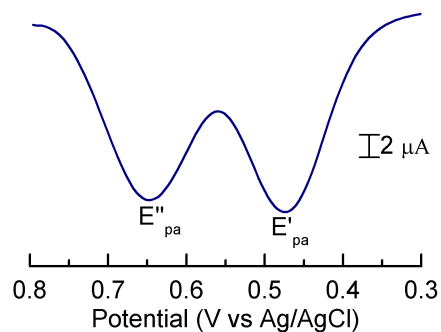


Figure 6. Example of a differential pulse voltammetry depicting two oxidations.

Equilibrium Constant

Once the half-wave potential ($\Delta E_{1/2}$) are obtained from the cyclic voltammetry experiments, the equilibrium constant can be calculated using the Nernst equation (Equation 4);

Eq. 4
$$K_c = \exp\left(\frac{F\Delta E_{1/2}}{RT}\right)$$

Where T is the temperature, R is the gas constant, and F is the faraday constant.

ET classification

The Robin-Day classification system is used to differentiate the types of electronic communication in mixed valent systems. The scheme divides molecules into three different classes, Class I, Class II, and Class III. A Class I molecule has the least amount of electronic communication with a value of $K_c < 10^2$. Class III molecules have a value of $K_c < 10^6$, therefore having the best electronic communication. Class II molecules have intermediate electronic communication and K_c lies between 10^2 and 10^6 .

The difference in degree of electronic communication between or within molecules depends on how the redox centers are linked to each other. In a molecule with two redox centers linked covalently (Figure 7a), one redox center gains an electron for an initial reduction. If there is sufficient electron delocalization within the system, the second redox center will be affected by the added electron. With better electronic communication between the redox centers a second reduction will be more challenging to obtain. In a cyclic voltammogram this added difficulty will be proportional to the potentials at which the redox events occur. The greater the energetic barrier associated with the second reduction, the larger the difference in potentials at which the events occur. This can be quantified by the difference in half wave potentials, $\Delta E_{1/2}$.

A molecule not directly linked to the second redox center (Figure 7b) would have weak electronic communication and a second electron would be added with greater ease. The molecule with weak electronic communication will have a cyclic voltammogram in which the redox events are not well defined and the potential difference is smaller, resulting in a lower $\Delta E_{1/2}$.

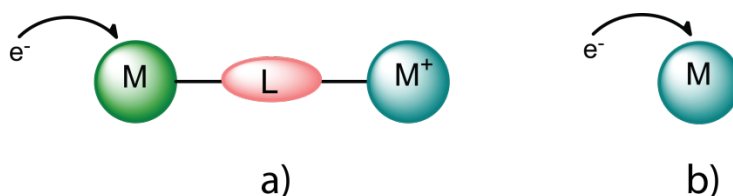


Figure 7. Example of two molecular systems; a) A system with large electronic communication will show a greater $\Delta E_{1/2}$, b) a system with a poor electronic communication will show a small $\Delta E_{1/2}$.

Procedure

Turn on the CH Instrument Electrochemical Workstation. Wait about twenty second for the instrument to warm up. Go to “Start” and “Run” and type: “C:\CHI”. Choose “CHI760D (Electrochemical Software)”. If a dialog boxer appear, press “OK” until you see the software open. Next, choose “Setup” → “System,” and make sure COM 3 is selected. Press “OK,” and choose “Setup” → “Hardware Test.” You should hear a clicking sound and a dialog box should appear. At the end of each of the six tests, you should see "OK" If you see something other than "OK" after any of those tests, wait a minute and run the Hardware Test again.

1. Pour 10 mL of a 2 mM E-dimethyldiferrocenylethylene / 1 M TBAPF₆ solution in dry DCM into the provided electrochemical cell containing a stir bar and place it on a stir plate.
2. Bubble the solution with nitrogen for about 5 minutes.
3. Next, gently feed the platinum wire through the smallest opening on the cap provided.
4. Place the cap on the cell such that the platinum wire rests on the bottom of the beaker.
5. Remove the yellow cap off the platinum working electrode. Place the platinum working electrode in the larger opening, and place the white non-aqueous Ag⁺/AgCl reference electrode in the smaller opening.
6. Attach the green alligator clip to the working electrode, the white alligator clip to the reference electrode, and the red alligator clip to the flat end of the platinum counter electrode.
7. Connecting the alligator clips may cause the electrodes to move. Make sure none of the electrodes touch, for this will cause a short circuit. Bubbles may form around the electrodes; if so stir the solution to remove them.
8. To check if you have properly set up your electrochemical cell, choose "Control" → "Open Circuit Potential."
9. Open the “CV Par.bin” file with the CH Instruments software. This will load the experimental parameters.
10. Choose “Control” → “Run Experiment.”
11. When the run is over, choose “Graphics” → “Present Data Plot.” Make sure to “Save As” and save your file to your U: drive as “your initials_ferrocene CV.”
12. Run the experiment two more times (steps 1 -10) for Z-dimethyldiferrocenylethylene and ferrocene.
13. Record the half-wave potential $\Delta E_{1/2}$ and calculate K_{com} for each compound.
14. Report your data and calculations in a lab report with an ACS style format. Turn in the lab report in one week.

Report

Your report must include the following information:

1. An introduction (in your own words!) of what electronic communication is and how physical chemists have measured it, other than through electrochemistry.

2. A well written account of the procedures that you performed in this laboratory
3. A results section that describes what you observed, including your calculated K_c and $\Delta E_{1/2}$.
4. A discussion section describing the significance of your results. What systems show strong, weak, or no electronic communication?
5. A conclusion summarizing the key take home points of this laboratory practice

References for student handout:

- (1) Yuan Jang, C.; Dung-Shien, P.; Chi-Fa, C.; Jia-Xin, S.; She JIng, L.; Keh Shin, K. *Inorg. Chem.* 2000, 39 (5), 953.
- (2) Perkins, R. I. *J. Chem. Educ.* 1985, 62 (11), 1018.
- (3) Berg, J.; Tymoczko, J.; Stryer, L. *Biochemistry*, 5th ed.; W H Freeman: New York, 2002.
- (4) Sutin, N.; Creutz, C. J. *J. Chem. Educ.* 1983, 60 (10), 809.
- (5) Osteryoung, J. J. *J. Chem. Educ.* 1983, 60 (4), 296.

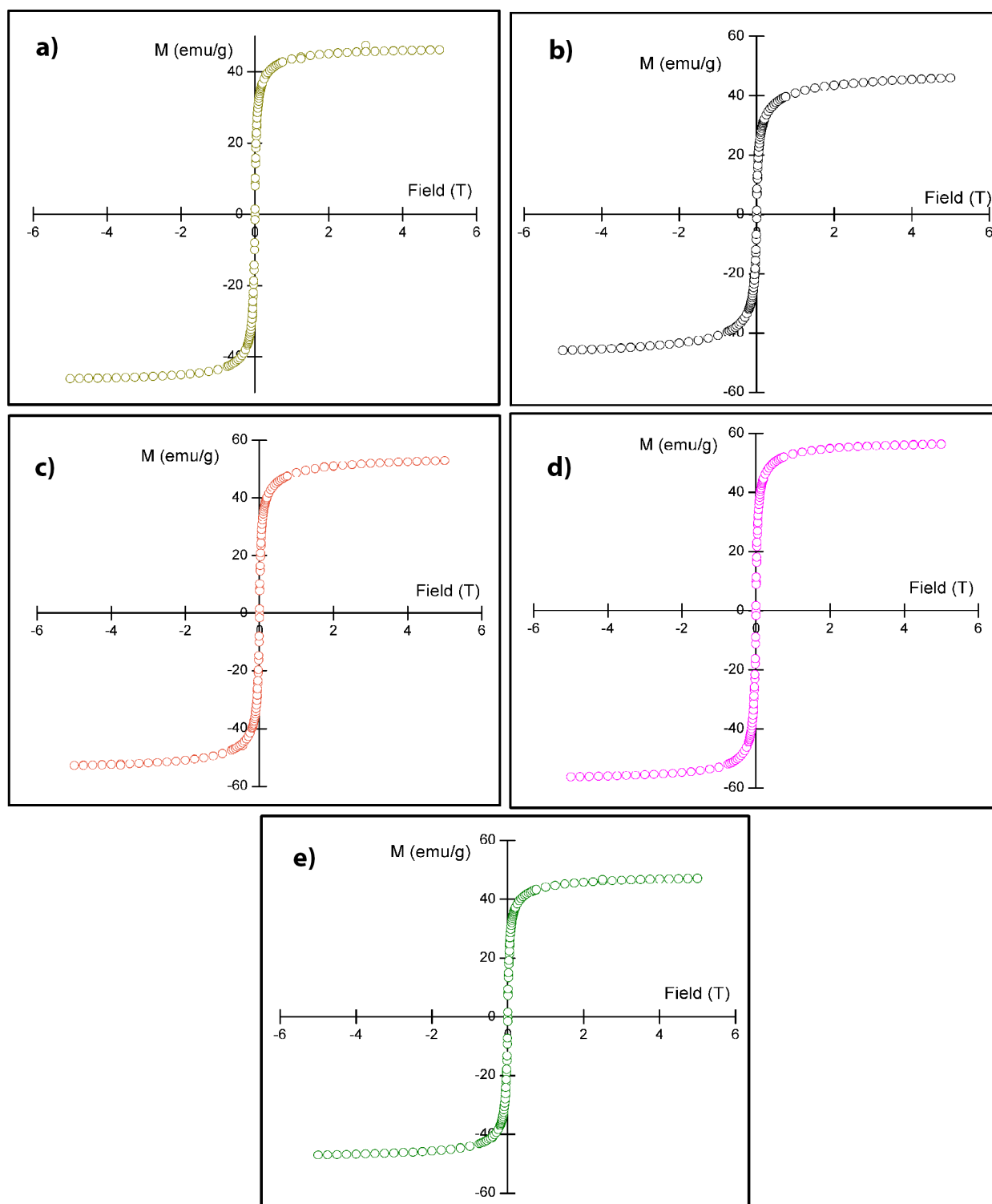


Figure 35. Hysteresis loop studies for a) Fe_3O_4 , b) $\text{GO-Fe}_3\text{O}_4$, c) $\text{Fe}_3\text{O}_4\text{-APTES}$, d) Co composite, e) Ni composite

Vita

Karen Ventura was born in El Paso, Texas. After completing her coursework at Instituto Tecnológico de Estudios Superiores de Monterrey in Cd. Juárez, México in 2009, Karen pursued her Bachelor's of Science degree at the University of Texas at El Paso. During the summer of 2011 she attended Versalius College in Brussels, Belgium. Later in the summer of 2012 she attended Shantou University in Shantou, China. She graduated with a major in Chemistry in December 2012. In August 2013 she entered the Graduate School of The University of Texas at El Paso to pursue a Master's degree. She graduating in December 2015 with a Masters in Chemistry. Subsequently in January 2016 she began her Doctoral degree at the same University.

Permanent address: 379 Morning Star
El Paso, TX, 79912

This dissertation was typed by Karen Ventura